

FIRST DETECTION OF THE ENVIRONMENTAL DEPENDENCE OF THE STRUCTURES OF MASSIVE GALAXIES

SONG HUANG (黃崧)¹, HSC COLLABORATION¹

(Dated:)
Draft version 0

ABSTRACT

Although the environmental dependence of structures for massive central galaxies is predicted by the promising hierarchical assembly model, observations at low redshift seem to find no convincing evidence for that. With the help of deep *i*-band images of a large sample of massive central galaxies at $0.3 < z < 0.5$ from the Subaru Hyper Suprime-Cam (HSC) survey, we map their stellar mass distributions out to radius larger than 100 kpc, and discover subtle, but systematic and robust structural differences that depend on halo mass. At fixed stellar mass within 100 kpc, the massive central galaxies in more massive ($M_{200m} > 1.6 \times 10^{14} M_\odot$) halos have a slightly flattened inner profile within $\sim 15\text{--}20$ kpc, and a more prominent outer envelope compared to ones in less massive ($M_{200m} > 8.7 \times 10^{13} M_\odot$) halos. For centrals with $M_* > 10^{11.5} M_\odot$, the ones in more massive halos show very significant excess of mass in the outskirt when the two samples are matched using proxies of mass assembled at $z > 1$. Such differences are broadly consistent with richer recent merging history for more massive halos. We suggest that the relation between total stellar mass and mass within inner 5 or 10 kpc is potentially interesting for diagnosing the role played by host halo in shaping the structures of massive central galaxies. These results also highlight the importance of deep photometry and the usage of detailed structural information in the study of the assembly history of galaxies.

Subject headings: galaxies: elliptical and lenticular, cD — galaxies: formation — galaxies: photometry — galaxies: structure — galaxies: surveys

1. INTRODUCTION

Scientific Background

- Massive galaxies are important cosmic probe and unique labs to study galaxy evolution.
- Briefly explain why massive early-type galaxies are important through the difficulties of stellar-halo mass relation and stellar mass function at the high-mass end.
- Brief summary of the current understanding of their cosmic assembly history.
- Explain why we should care about the environment, and why we expect to see some environmental dependence in the structure and other properties of massive galaxies.
- Brief review of the current observations. It is still not clear whether there is a clear environmental dependence.

Observational difficulties (a.k.a Why we need HSC)

- Explain why it is important to study the mass distribution of massive galaxies out to large physical radius; and, given their unique light profiles, why it is more difficult to study them compared to late-type galaxies.
- Very brief summary of past observational efforts, and why they are not good enough (Not enough number of really massive galaxy; Shallow images; Background subtraction issue; and stacking analysis can be dangerous as while)

song.huang@ipmu.jp

¹ Kavli Institute for the Physics and Mathematics of the Universe, The University of Tokyo Institutes for Advanced Study, the University of Tokyo (Kavli ITPU, WPI), Kashiwa 277–8583, Japan

Basic idea of this work

- Here we take advantages of the ambitious Hyper-Suprime camera survey...

Here, we take advantage of the excellent image quality of the HSC survey, and investigate the potential environmental dependence of structure for massive galaxies via comparing the surface M_* density profiles and structural scaling relations between massive central galaxies in different environments. As shown in Fig.1, the HSC *i*-band images are typically 3–4 magnitude deeper than SDSS ones, and have much better seeing condition (median FWHM $\sim 0.6''$), hence they are perfect for mapping the M_* distributions of massive galaxies out to very large radius. With the help of a cluster catalog, we select a large sample of massive central galaxies in halos that are more or less massive than $\log(M_{\text{Halo}}/M_\odot) \sim 14.0$ at $0.3 < z < 0.5$ from the available ~ 100 square degree of HSC data.

Due to the difficulty in appropriately modeling the M_* distributions of massive galaxies out to their very outskirts, we focus on M_* within two different physical apertures in this work:

- M_* within 10 kpc, $M_{*,10\text{kpc}}$: according to the “two-phase” scenario, the “in-situ” star-formation quickly built up the inner, dense core of massive ETGs. Based on recent observations and simulations (e.g. van Dokkum et al. 2010; Rodriguez-Gomez et al. 2016), the in-situ component distributes mostly within the effect radius (R_e , or 5–10 kpc) in massive galaxies. Here we use $M_{*,10\text{kpc}}$ as a proxy of the M_* formed in the “in-situ” phase. Although it is an empirical choice, the detailed comparison of the stellar mass surface density (μ_*) profiles later suggests it indeed helps reveal interesting environmental dependence. Under the adopted cosmology, $1.0''$ in radius equals 4.4 and 6.1 kpc at redshift

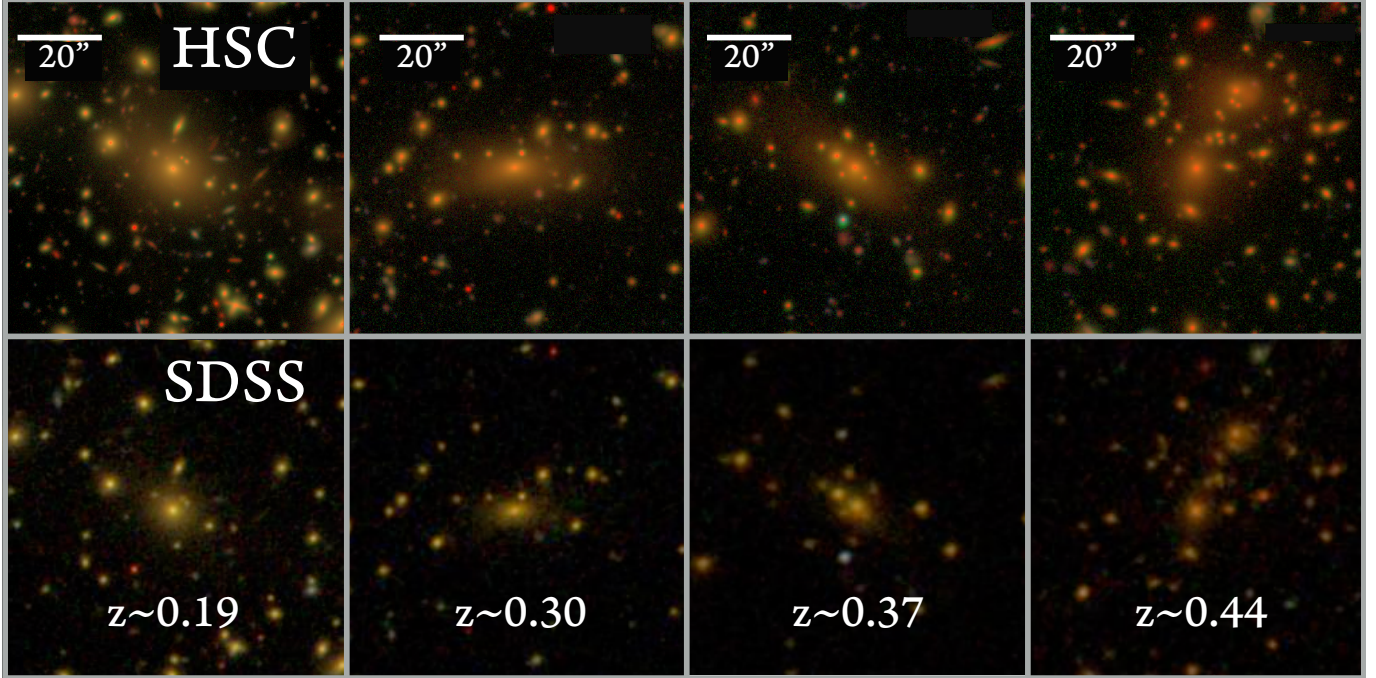


FIG. 1.— A comparison between the imaging quality of SDSS and HSC Wide for a sample of nearby massive elliptical galaxies at $0.2 < z < 0.5$. These images are generated using *gri* band images with an arcsinh stretch (Lupton et al. 2004). The HSC Wide layer is 3.0-4.0 magnitudes deeper than SDSS which is critical in order to map the outskirts of ETGs out to large radii.

0.3 and 0.5. We can reliably measure $M_{*,10\text{kpc}}$ without being bothered by smearing effect of seeing.

- M_* within 100 kpc, $M_{*,100\text{kpc}}$: for massive galaxies in this work, 100 kpc aperture reaches to $5\text{-}10 \times R_e$ and very low μ_* region, hence can be treated as proxy of the “total” M_* . Limited by the accuracy of background subtraction, the μ_* profile of outer region can not be reliably recovered for massive galaxies across our redshift range. Although not perfect, $M_{*,100\text{kpc}}$ is still a much better tracer of total M_* than the model-dependent ones using shallower images.

Massive central galaxies in this work show an intriguing diversity on the plane defined by these two metrics. We preview this using Fig.2, which shows a subsample of massive galaxies at $z \sim 0.4$ that share very similar value of $M_{*,10\text{kpc}}$, but show a large range of outer structures. Assuming galaxies at the same $M_{*,10\text{kpc}}$ have similar amount stars in the in-situ component, it is of great interest to investigate the relation between their environments and outer envelopes that are assembled at later time. It is worth noting that, although a circular aperture is shown on Fig.2, we always use elliptical apertures that follow the average isophotal shape for photometry in this work. And, within our choices of redshift and M_* ranges, we can safely ignore significant mass growth and structural evolution (no star formation, lower merger rate et al. e.g. Bellstedt et al. 2016, Inagaki et al. 2015; but also see Bai et al. 2014) with our redshift and M_* ranges.

The paper is organized as follows. Section 2 gives a brief overview of the HSC observation and data reduction, along with the summary of the data selection processes. Then, we will explain the procedures for extracting 1-D surface brightness profiles (Section 3) and estimating stellar mass (Section 4) in details. We will present the main results in Section 5, and discuss the several related technical and scientific issues in Section 6, ending with summary and future plans in Section

7.

All the magnitudes used here are in AB system (Oke & Gunn 1983), and are corrected for Galactic extinction using calibrations from Schlafly & Finkbeiner (2011). In this work, we assume $H_0 = 70 \text{ km s}^{-1} \text{ Mpc}^{-1}$, $\Omega_m = 0.3$, and $\Omega_\lambda = 0.7$.

2. DATA AND SAMPLE SELECTION

2.1. The Hyper Suprime-Cam Survey

The Subaru Strategic Program (SSP, REF) makes use of the new prime-focus camera, the Hyper Suprime-Cam (HSC; Miyazaki et al. 2012), on the 8.2-m Subaru telescope at Mauna Kea. This ambitious multi-layer photometric survey takes advantage of the large field of view (FoV; 1.5 deg in diameter) of HSC and will cover $\sim 1400 \text{ deg}^2$ of sky in 5 broad bands ($g\ r\ i\ z\ Y$) to the depth of $r \sim 26$ mag in the WIDE. This work is based on the internal data release S15B, which covers ~ 100 square degree of sky in all 5-band to full WIDE depth. The regions covered by this release overlap with a number of spectroscopic surveys (e.g. SDSS/BOSS: Eisenstein et al. 2011, Alam et al. 2015; GAMA: Driver et al. 2011, Liske et al. 2015).

The HSC WIDE survey is 3.0-4.0 magnitudes deeper in the i -band than SDSS. Combined with the excellent imaging resolution (median i -band seeing is $0.6''$), and the wide area, this makes the HSC wide layer a tremendous data set to perform a large statistical study of surface brightness profiles of ETGs out to large radii. Fig.1 illustrated the quality of HSC imaging compared to SDSS for a sample of low redshift ETGs. Fig.1 clearly demonstrates that the HSC Wide survey is well suited for mapping the stellar distribution of massive galaxies out to large radii and will be a powerful data set to explore the assembly history of ETGs.

The HSC i -band images typically have the best seeing in all five bands because of strict requirements determined by weak lensing science. We will therefore use the i -band images to measure the stellar distributions of massive galaxies.

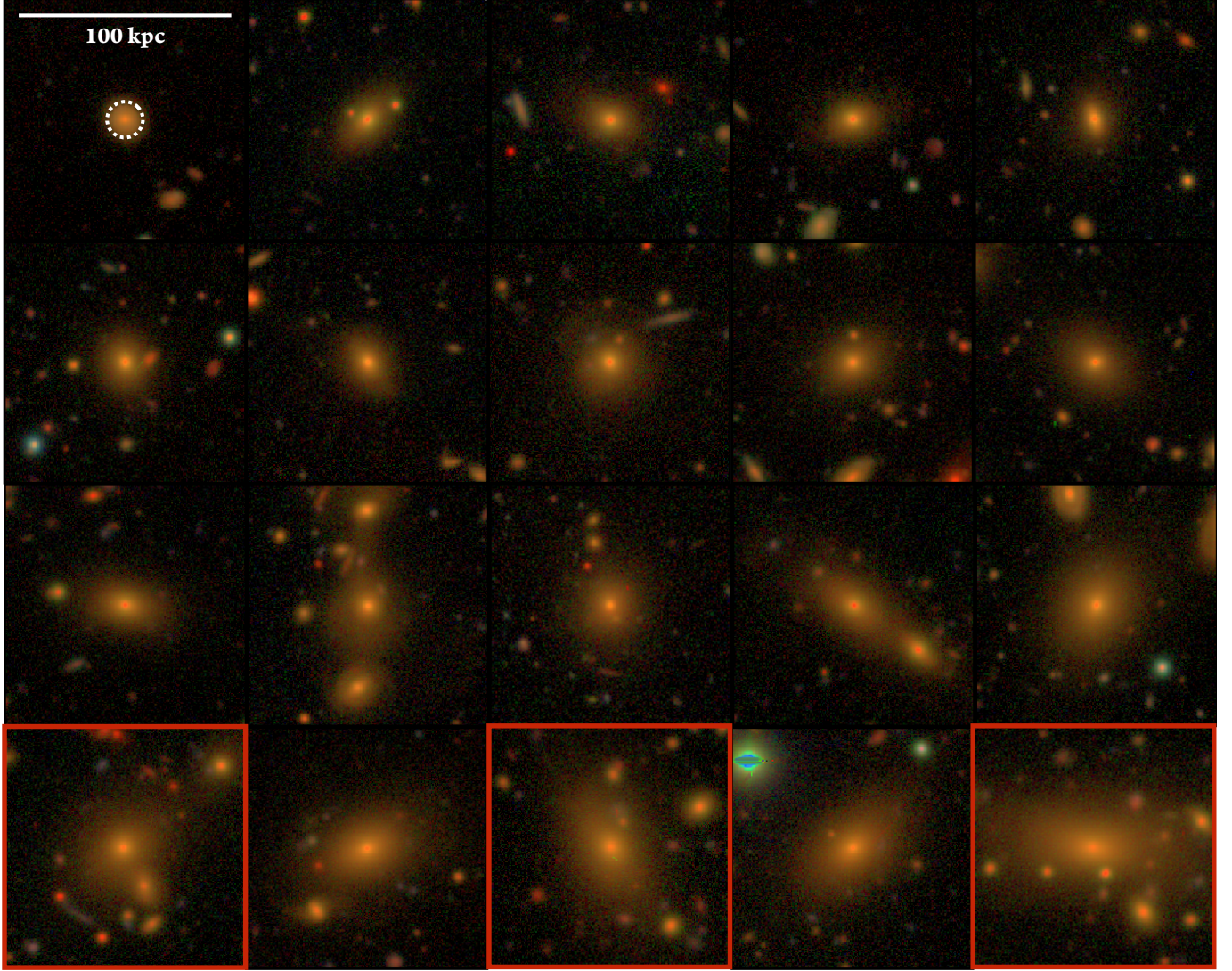


FIG. 2.— Three-color images for a subsample of massive galaxies at similar redshift (~ 0.4), and with similar M_* inside inner 10 kpc (indicated by the dash-line circle on top-left figure; $11.2 < \log(M_{*,10 \text{ kpc}}/M_\odot) < 11.3$). However, they span quite a large range in M_* within 100 kpc (highlighted by the solid bar on the top-left figure). From top-left to bottom-right, their $M_{*,100 \text{ kpc}}$ increases from $10^{11.2} M_\odot$ to $10^{11.7} M_\odot$. The three galaxies from cenHighMh sample are highlighted via red frames.

2.2. The HSC galaxy catalog and photometry measurements

The HSC SSP data are processed with `hscPipe 4.0.1`, a derivative of the Large Synoptic Survey Telescope (LSST) pipeline (e.g. Jurić et al. 2015; Axelrod et al. 2010), modified for HSC. `hscPipe` first performs a number of tasks at the single exposure level (bias subtraction, flat fielding, background modeling, object detection and measurements). Then pipeline perform astrometric and photometric calibration for each single exposures. After that, the `hscPipe` warp different exposures on to a common World Coordinate System (WCS), combine them into coadded images with improved signal-to-noise ratio (S/N), and update the images with better astrometric and photometric calibrations at the same time using the common stars among different exposures. The pixel scale of the combined images is $0.168''$. The photometric calibration is based on data from the Panoramic Survey Telescope and Rapid Response System (Pan-STARRS) 1 imaging survey (Schlafly et al. 2012, Tonry et al. 2012, Magnier et al. 2013). To achieve consistent deblending and photometry across all bands, `hscPipe` performs multi-band post-processing at the

coadd level. First, the `hscPipe` performs object detection again on the coadd images in each band independently, and identify the above-threshold region (referred as “footprint”) and the flux peak within it for each source. “footprints” and peaks from different bands are then merged together before the `hscPipe` deblend and measure them in each band. Later, `hscPipe` selects a “reference band” for each object based on the S/N in different bands (for most galaxies in this work, it is the i -band). After fixing the centroids, shape, and other non-amplitude parameters of each object in this reference catalog, `hscPipe` perform forced photometry on the coadd image in each band. The PSF and galaxy model fluxes measured in the forced photometry approach are the best for color measurements. Please refer to Bosch (in prep.) for more details of the `hscPipe` and the multi-band processing method.

The HSC `cModel` algorithm is similar to the SDSS `cModel` one. It fits the flux distribution of an object using a combination of de Vaucouleur and exponential components after considering the PSF convolution. For more details about the algorithm, please see Bosch et al. in prep.. We have tested its performance using synthetic objects (Huang et al. in

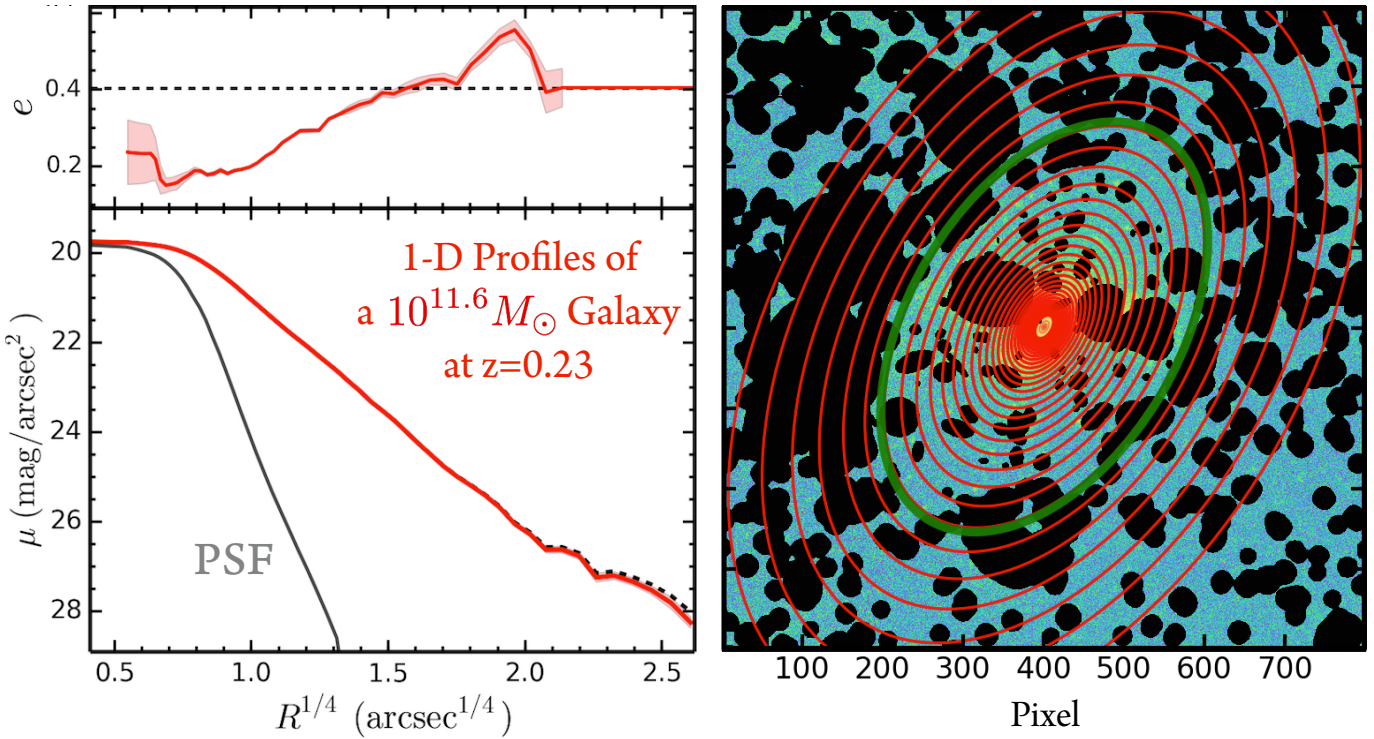


FIG. 3.— Left: example of the 1-D surface brightness and ellipticity profile for a massive galaxy at $z = 0.23$ in i -band using `Ellipse`. In this work, we always show the radial profile in $R^{1/4}$ scale as it is the most appropriate one to show the structural details of massive ETGs at both inner and outer regions. The dash-line shows the surface brightness profile after correcting the background. We also plot the brightness profile of the PSF model normalized at the central surface brightness of the galaxy to highlight the region affected by seeing. On the top panel, the dash line shows the ellipticity used for the final isophote. Right: the masked i -band image of this galaxy with the isophotes extracted by `Ellipse` overlaid. The thick, green isophote highlights the one with $\mu_i \sim 28.5$ mag arcsec^{-2} . [Song: Will update completely, takes a little bit longer]

prep.), and the results indicate that, generally speaking, the HSC cModel photometry is accurate down to $i > 25.0$ mag. However, for massive ETGs with extended stellar distributions, cModel currently systematically underestimates their total flux. This problem indicates the intrinsic limitation of cModel as it is incapable of modeling profiles that are extremely extended in the outskirt at the depth of HSC survey. At the same time, issues with the deblender also worsen the situation. As the image becomes much deeper, it also significantly increases the fraction objects that are blended with others, and makes reliable deblending process a very challenging problem especially for massive ETGs where satellites and background galaxies often blend with the low surface brightness stellar envelope. To make sure the reliable detection of faint objects close to the detection limit, the deblending method implemented by the hscPipe now tends to “over-deblend” the surrounding areas of bright galaxies, and further results in under-estimated total flux of massive ETGs (more discussion in Bosch et al. in prep.). For these reasons, we will perform customized photometric measurements to derive more accurate total luminosity and stellar mass. We only use the HSC cModel photometry in the initial selection of parent sample.

2.3. Initial Massive Galaxy Sample

Because of the caveats that apply to hscPipe measurements for bright galaxies, we will use custom made software to measure the luminosity profiles of massive galaxies. **As the first step, we select the initial sample of massive galaxies at $z < 0.5$ from the HSC photometric catalog.** We will then use custom made software to re-measure lumi-

nosities for all galaxies in this sample. Based on Leauthaud et al. (2016), most $\log(M_*/M_\odot) \geq 11.5$ galaxies should have $i_{\text{SDSS,cModel}} \leq 21.0$ mag. So we first select all galaxies with $i_{\text{HSC,cModel}} \leq 21.5$ ² in regions that have reached the required depth of WIDE survey in all five bands.

We select extended objects that have no error in deblending process, well defined centroids, and cModel magnitudes in all five bands. After removing the objects that have pixel affected by saturation, cosmic-ray, and other optical artefact³, we select 1760845 galaxies that will be referred as hscPho.

As reliable photometric redshift using HSC photometry is still a working progress, we only use objects with either available spectroscopic redshift or robust red-sequence photo-z from the redMaPPer catalog (see Section 2.4). We first match the hscPho sample with the external spec-z catalog compiled by the HSC database⁴ using $1.0''$ radius. At $0.2 \leq z \leq 0.5$, most redshifts in the HSC spec-z catalog come from SDSS/BOSS and GAMA surveys. The BOSS survey provides the majority of spec-z in this work. Due to the complex selection criteria for different subsamples within the BOSS survey (e.g. the LOWZ and CMASS), it is not easy to estimate its M_* completeness. Recently, through comparing with the deeper Stripe 82 Massive Galaxy Catalog (S82-MGC; Bundy et al.

² We neglect the insignificant differences between the response curves of SDSS- i and HSC- i filters

³ each criterion affects less than 8% of the entire sample

⁴ It is created by matching HSC objects with public data of several spectroscopic surveys (e.g. SDSS/BOSS; GAMA). Duplicated matches from different sources are merged through internal matching using $0.5''$ radius. For each object, the quality information of the spec-z from different catalogs are homogenized into a single flag that indicates whether the redshift is secure, and only secure spec-z are used in this work.

2015), Leauthaud et al. (2016) suggests that the BOSS spec- z is about 80% complete at $\log(M_*/M_\odot) \geq 11.6$ at $0.3 < z < 0.5$. The GAMA survey, which partially overlaps with the HSC footprint, provides additional 14% unique spec- z . Based on Taylor et al. (2011) (e.g. their Fig. 6), at $z \sim 0.3$, the GAMA sample is 80% complete down to $10^{10.8} M_\odot$; but only 80% complete to $10^{12.0} M_\odot$ at $z \sim 0.5$. Despite the difference in M_* estimates, we can expect our sample should be quite complete above $\log(M_*/M_\odot) \geq 11.5\text{--}11.6$. We will further address the issue of M_* -completeness more carefully using the common sample with S82–MGC (see Section 4.2).

Among the 116813 matched objects, 42696 are at $0.2 \leq z \leq 0.5$. The majority of these redshifts come from either SDSS or BOSS data. GAMA survey contributes another $\sim 14\%$. For objects without external spec- z , we match them with the central galaxies from redMaPPer catalog using $2.0''$ radius. The matched objects with useful red-sequence photo- z (z_λ) are also included in the final sample of bright galaxies with reliable redshift between $0.2 \leq z \leq 0.5$ (will be referred as hscZ). As we will mention at the end of the paper, to ensure reasonable M_* -completeness at the high- M_* end, and make sure the samples we want to compare have well overlapped redshift distributions, we will focus on the galaxies at $0.3 \leq z \leq 0.5$.

2.4. redMaPPer cluster catalog

In this paper, our study focuses on galaxies which are located at the center of their dark matter halos. To limit our sample to central galaxies, we use v5.10 of the redMaPPer cluster catalog⁵ (e.g. Rykoff et al. 2014; Rozo et al. 2015b). These authors have developed a well-tested red-sequence cluster finder that has been run on SDSS DR8 (Aihara et al. 2011) photometric data. For each cluster, the catalog provides a photometric redshift estimate z_λ , a richness λ , and identified the most likely central galaxy (this is the galaxies with the highest value of the central probability P_{Cen}). A list of member galaxies for each cluster, and associated membership probabilities, is also provided. Details about the performance of the redMaPPer cluster catalog can be found in Rozo & Rykoff (2014), Rozo et al. (2015a), and Rozo et al. (2015b). Several studies have published calibrations between the redMaPPer richness estimate, λ , and halo mass (e.g. Saro et al. 2015; Farahi et al. 2016; Simet et al. 2016). The results of these studies are in good agreement and indicate that clusters identified by redMaPPer ($\lambda > 20$) have $\log(M_{200,c}/M_\odot) \geq 14.0$. Therefore, the redMaPPer catalog helps us group the massive central galaxies into samples with different average M_{halo} . And, to select reliable candidates of central galaxies, we only include the ones with high probability of being the central galaxy ($P_{\text{Cen}} \geq 0.7$).

Although the redMaPPer catalog provides us a good sample of central galaxies in massive halos, the typical uncertainty of λ estimate is still at $\sim 5\text{--}10$ level. In addition, due to the depth and resolution of SDSS images, the redMaPPer catalog becomes slightly incomplete at lower richness ($\lambda < 40$) end at $z > 0.33$. To reduce the impacts from uncertain richness and incomplete selection of massive halos, we will focus on a sample of central galaxies in halos with $\lambda > 30$. This will also help up enhance the M_{halo} contrast in the structural comparison. Based on the calibration in Simet et al. (2016), the $\lambda \geq 20$ sample should have halo mass

(M_{200m}) more massive than $10^{14.0} M_\odot$. For the $\lambda \geq 30$ sample, they should live in halo more massive than $10^{14.2} M_\odot$ using the same calibration. And, we can confirm that the results presented later do not depend on the choice of λ boundary here. For the massive central galaxies that are not in these cluster-level halos, we unfortunately can not estimate their M_{halo} individually, but it is safe to assume they should have $\log(M_{200m}/M_\odot) < 14.0$.

2.5. Massive Central Galaxies from Low and High Mass Halos

Based on recent constraints of M_* - M_{Halo} relation (e.g. Leauthaud et al. 2012, Behroozi et al. 2013, Kravtsov et al. 2014), the M_{halo} of $\log(M_*/M_\odot) > 11.0$ galaxies has a large scatter at fixed M_* . Although we can not yet measure M_{halo} individually, we can still broadly separate them into galaxies in small groups ($\log(M_{\text{Halo}}/M_\odot) < 14.0$) and large groups/clusters ($\log(M_{\text{Halo}}/M_\odot) > 14.0$), and investigate the “environmental”-dependence of their structures.

Firstly, we match the hscZ sample with the massive central galaxies of redMaPPer clusters with $\lambda \geq 20$ and $P_{0.7} \geq 0.7$ using $1.0''$ radius. This step finds 375 matched galaxies at $0.2 \leq z \leq 0.5$ (among them 282 are at $0.3 \leq z \leq 0.5$). We will refer these **central galaxies in more massive halos** as cenHighMh sample from now on. A small fraction of redMaPPer centrals within the HSC footprints are missing due to severe contamination from optical artifacts or bright stars. Spec- z is not available for 67 (17.9%) galaxies in the sample, but their z_λ should be very accurate (median $|z_\lambda - z_{\text{Spec}}|$ is about 0.01 for the ones with spec- z). The median richness (λ) of these clusters is ~ 32 , corresponding to halo mass of $M_{200m} \sim 1.7 \times 10^{14} h^{-1} M_\odot$. Among these central galaxies, 222 are in clusters with $\lambda \geq 30$. When focusing on this subsample, the median richness is ~ 41 , corresponding to halos with $M_{200m} \sim 2.2 \times 10^{14} h^{-1} M_\odot$. Meanwhile, only 15% of cenHighMh sample lives in clusters with $\lambda \geq 50$ ($M_{200m} \sim 3.0 \times 10^{14} h^{-1} M_\odot$). Therefore, the current cenHighMh sample is not dominated by very massive clusters with $M_{\text{halo}} > 10^{15} M_\odot$.

Assuming that the redMaPPer catalog correctly identifies all halos with $M_{200m} \sim 1.0 \times 10^{14} h^{-1} M_\odot$ in the current footprint, the unmatched massive galaxies from the above step should be dominated by central galaxies of less massive halos and massive satellites galaxies. To select a purer sample of massive centrals in $M_{200m} < 10^{14} h^{-1} M_\odot$ halos, we identify and remove all galaxies within a cylinder region around the central galaxies in redMaPPer catalog. We choose to use the R_{200m} as the radius of the cylinder. For each cluster, we convert the richness estimates into M_{200m} using the calibration in (Simet et al. 2016), then estimate the R_{200m} using M_{200m} and the mass-concentration relation in (Diemer & Kravtsov 2015). For the thickness of the cylinder, we use twice the uncertainty of the photometric redshift error of each cluster. At $0.3 < z < 0.5$, such uncertainty is between 0.015 to 0.025, which are more than enough to exclude cluster member. [Song: The actual number waits to be updated]

However, we should note that the cenLowMh sample at this stage spans a large range in M_* , extending towards $\log(M_*/M_\odot) < 10^{11}$. Therefore, we should expect contamination from satellites in $\log(M_{\text{Halo}}/M_\odot) < 14.0$ halos at certain degree. Later, after we update the total M_* of them, we will mainly focus on the cenLowMh galaxies at high mass end, especially the ones at $\log(M_*/M_\odot) > 11.5$. Based on observa-

⁵ See: <http://risa.stanford.edu/redmapper/>

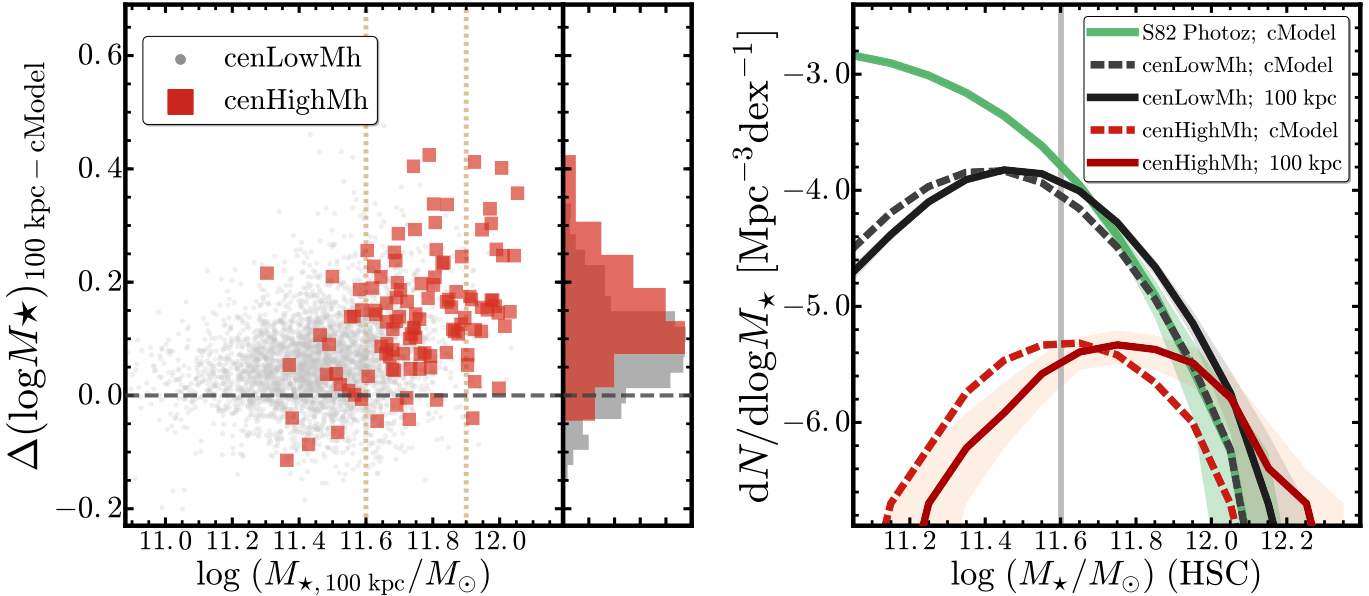


FIG. 4.— **Left:** Difference between $M_{\star, \text{cModel}}$ and $M_{\star, 100\text{kpc}}$ for central galaxies in halos smaller than $10^{14} M_{\odot}$ (grey dots) and in halos larger than $10^{14} M_{\odot}$ (red squares). On average, $M_{\star, \text{cModel}}$ underestimates the total stellar mass of massive galaxies by 0.1 dex and the difference can exceed 0.2 dex. Vertical histograms indicate the mass difference for galaxies with $11.6 < \log(M_{\star, 100\text{kpc}}/M_{\odot}) < 11.9$. **Right:** Impact of using $M_{\star, \text{cModel}}$ on the galaxy stellar mass function. Dashed lines correspond to the SMF computed using $M_{\star, \text{cModel}}$ as an estimate of the total luminosity whereas solid lines correspond to the SMF computed using the total luminosity from our 1-D profile modeling. The impact on the SMF can exceed 0.2 dex for massive centrals living in halos larger than $10^{14} M_{\odot}$ (red lines).

tional constraints (e.g. van Uitert et al. 2016), we can neglect satellite contamination at such high M_{\star} range.

2.6. Summary of Sample Construction

In summary, from the $\sim 100 \text{ deg}^2$ deep HSC images, we select a large sample of massive central galaxies with reliable redshift information, and broadly separate them into two groups with different M_{halo} . To help you go through the results, here are a few key points to keep in mind:

- **hscPho sample:** this parent sample consists of bright galaxies with $i_{\text{cModel}} \leq 21.0$, good quality images and reliable cModel photometry in all five HSC bands in the S15B data release.
- **hscZ sample:** through matching the hscPho sample with spectroscopic redshifts from surveys like SDSS/BOSS and GAMA, or accurate red-sequence photometric redshift in the redMaPPer catalog, we come up with a large sample of bright galaxies with reliable redshift information.
- **cenHighMh sample:** we select a sample of 375 galaxies at $0.2 \leq z \leq 0.5$ that are identified as central galaxies in $\lambda > 30$ redMaPPer clusters. The most reliable ones ($P_{\text{Cen}} > 0.7$) among them will represent the central galaxies in very massive halos ($\log(M_{\text{Halo}}/M_{\odot}) \geq 14.0$).
- **cenLowMh sample:** after excluding all the galaxies that are close to any redMaPPer clusters in both radial and redshift directions from the hscZ sample, we have 29973 bright galaxies at $0.2 \leq z \leq 0.5$. With the help of M_{\star} estimates via SED fitting (see Section 4.1), we consider the massive ones among them as the candidates of central galaxies in halos with $\log(M_{\text{Halo}}/M_{\odot}) < 14.0$.
- To compare the cenHighMh and cenLowMh samples carefully, we will focus on the redshift range at $0.3 \leq$

$z \leq 0.5$ where their redshift distributions greatly overlap and both samples have acceptable M_{\star} -completeness (see Section 4.2). Although we use the $\lambda > 30$ sample for structural comparison, in the Appendix G, we show that the results will not change if we include central galaxies of $20 < \lambda \leq 30$ clusters in the cenHighMh sample.

3. MEASUREMENTS OF 1-D SURFACE BRIGHTNESS PROFILE

To estimate the total luminosity of massive galaxies, and measure their one-dimensional stellar mass density (μ_{\star}) profiles, we perform elliptical isophotes fitting using the IRAF task `Ellipse` (Jedrzejewski 1987). Compared to the popular two-dimensional model fitting method, the isophote fitting approach is much less sensitive to the choice of model, number of components, and the initial guesses of free parameters. It is also less affected by the uncertainty of sky background subtraction. This is particularly important for the massive ellipticals in our sample. The much deeper HSC image reveals significantly more extended structures, while also make it inappropriate to fit these galaxies with simple model like the de Vaucouleurs model or single Sérsic component model. Such models fail to fit the central region and the stellar halo of massive galaxies simultaneously, and also can not account for the radial variation of ellipticity and position angle. In principle, such massive galaxies can still be described using more complex models (e.g Huang et al. 2013b; Huang et al. 2013a). However, they are still very sensitive to background subtraction. And it becomes even more difficult to choose initial parameters, and investigate the degeneracies among parameters. Although it is certainly worth exploring in the future, we decide that the 1-D method suits the goal of this work better.

We first prepare large i -band cut-out images around these massive galaxies that cover at least 750 kpc in radius, along with the bad pixel masks, and the PSF model reconstructed using the central coordinates. While they include all the visible light of the galaxy, they also leave enough space to eval-

uate the background subtraction. We choose to use *i*-band images not only considering their excellent seeing condition, but also because they trace the stellar distributions of massive galaxies at $0.3 \leq z \leq 0.5$ reasonably well (fall between rest-frame *g* and *r* band), and they suffer less from background uncertainty, which is crucial for studying the outskirt of massive ETGs. Although *z* and *Y*-band should be better μ_* tracer, the sky background is much higher and the seeing is considerably worse on average.

Secondly, using the SEP Python library, we perform SExtractor-like background estimation and object detections using different configurations to overcome the “over-deblending” challenge met by the hscPipe. Combining detections using different backgrounds and *S/N* thresholds, we correctly obtain the footprints of all objects, even of the ones that are very close to the center of bright galaxies. For the rest objects, we convert their footprints into a mask image for the Ellipse procedure after increasing their sizes adaptively based on the brightness and distance to the massive galaxy. We achieve this via convolving the individual footprint with a Gaussian kernel so that we can conservatively exclude pixels affected by this object while still making the mask follow the shape of the object. Meanwhile, we create a more aggressive mask of *all* objects in the same approach, median-rebin the remaining pixels using a 6×6 pixels box, and take the peak value (or mode) of the distribution of these rebinned “sky” pixels as the average background value around these bright galaxies. As expected, we often found slightly negative value that indicate over-subtraction of background at certain degree. In hscPipe, the background on each CCD is modeled with a Chebyshev-polynomial fit to the smoothed image after excluding pixels with $S/N > 5$. This algorithm suffer less than the SDSS version (e.g. see Blanton et al. 2011), but still over-subtract background around very bright object. For our massive galaxies, such over-subtracted background creates artificial truncation or steeper surface brightness profile. We therefore provide an ad hoc fix using a SExtractor-style background model (200×200 pixels background box size, and 6 pixels median filtering size of sky boxes) via running SEP on the image with all objects masked out. This model can account for the slightly over-subtracted background at very large scale, shift the distribution of rebinned “sky” pixels to 0, and do not affect the intrinsic flux distribution of our target.

Finally, we run Ellipse on the background-corrected image following similar strategy of (Li et al. 2011). In short, we start with free centroid and shape of each isophote, then gradually constrain their behaviors, and eventually extract 1-D surface brightness profile along the major axis using isophotes with fixed centroid and shape. The 4th Fourier modes are included to fit the isophote better. In this way, we can extract the radial changes of the centroid, ellipticity, position angle, and average isophotal distortions (more “disky” or “boxy”, e.g. Kormendy et al. 2009) along with the surface brightness profile. Fig.3 shows an example of the 1-D surface brightness and ellipticity profile for a massive galaxy at $z \sim 0.2$ along with its masked image and a subset of isophotes. Appendix.B includes more details about the Ellipse procedure.

For physical (e.g. late-stage major merger) and unphysical (e.g. nearby foreground galaxy or bright star) reasons, we can not extract reliable 1-D profiles for small fraction of massive galaxies due to heavily masked out central region. This issue reflects an intrinsic limitation of the 1-D method. It affects 48/375 cenHighMh galaxies, and a smaller fraction of cenLowMh ones. It is worth noting that this excludes most

massive galaxies in major merger process from the analysis. We will come back to them in the future using 2-D modeling method.

We correct these surface brightness profiles for Galactic extinction and cosmological dimming, then integrate them to various radius to get the luminosity within different physical apertures. Although the *i*-band 1-D profile can in principle reach to ~ 30 mag arcsec $^{-2}$, we notice the profiles at very low surface brightness part are often less reliable by showing truncation or large fluctuation that are due to either background uncertainty or contamination from bright neighbours. We therefore only consider the < 28.5 mag arcsec $^{-2}$ part of the profile here. This conservative choice already allows us to study the region out to ~ 120 kpc for massive galaxies in this sample.

4. STELLAR MASSES AND STELLAR MASS DENSITY PROFILES

4.1. Stellar Masses from SED Fitting

To convert the luminosity into stellar mass estimates, we assume that these massive galaxies can be well described by an average M_*/L_* . This is a reasonable assumption considering that they are ETGs that are dominated by old stellar population and are known to have shallow color gradients. We will further justify this point using the average color profiles in Section 6.

We use the broadband Spectral Energy Distributions (SEDs) fitting (see Walcher et al. 2011 for a recent review) code iSEDFit⁶ (Moustakas et al. 2013) to estimate the average M_*/L_* and *k*-corrections using 5-band HSC cModel fluxes under forced-photometry mode. Although cModel tends to underestimate the total flux for bright, extended objects, the forced-photometry results still provides accurate *average* color of the galaxy as it constrains the behaviour of the model using the optimized reference one and takes the PSF convolution into account (e.g. Huang et al. in prep.).

iSEDFit takes a simplified Bayesian approach. In short, it first generates a large grid of SEDs from synthetic stellar population models by drawing randomly from the prior distributions of relevant parameters (e.g. age, metallicity, dust extinction, and star formation history). Based on these models, it uses the observed photometry and redshift to compute the statistical likelihood, and generate the posterior probability distribution (PDF) functions of each parameter. To get the best estimate of certain parameter, iSEDFit “integrates” the full PDF over all the other “nuisance” parameters. Then, the median value of the resulting marginalized PDF is used as the best value, while the $1-\sigma$ uncertainty is derived from the cumulative PDF. Please refer to Moustakas et al. (2013) for technical details and performance of iSEDFit.

In this work, we derive average M_*/L_* using the Flexible Stellar Population Synthesis⁷ (FSPS; v2.4; Conroy & Gunn 2010a, Conroy & Gunn 2010b) model based on the MILES⁸ (Sánchez-Blázquez et al. 2006, Falcón-Barroso et al. 2011) stellar library and Chabrier (2003) IMF between 0.1 to 100 M_\odot . We use a delayed- τ model with stochastic star burst as the form of star formation history (SFH), and choose a set of reasonable parameters after some tests. Such form of SFH is appropriate for massive galaxies at low redshift (e.g. Kauffmann et al. 2003). For stellar metallicity, we assume flat dis-

⁶ <http://www.sos.siena.edu/jmoustakas/isefit/>

⁷ <http://scholar.harvard.edu/cconroy/sps-models>

⁸ <http://www.iac.es/proyecto/miles/pages/stellar-libraries/miles-library.php>

tribution between 0.004 to 0.03 (which is the highest metallicity allowed by FSPS models). And, we adopt the [Calzetti et al. \(2000\)](#) extinction law with a order two Gamma distribution of A_V between 0 to 2 magnitude. Since most galaxies in both samples are red, quiescent galaxies, the results are not very sensitive to parameters related to SFH and internal dust extinction. To achieve reasonable sampling across these parameters, we generate 250000 models.

We construct five band SED using the forced-photometry cModel magnitude corrected for the Galactic extinction. As for the photometric error, the current cModel photometry underestimates the flux errors of bright galaxies as it only includes statistical error, not the systematic uncertainties in the model-fitting process. From tests of synthetic objects, we find that the average accuracy of cModel photometry for bright galaxy is roughly at 1% level. Therefore, we supply iSEDFit with simplified flux errors assuming $S/N = 100$ for riz bands, and $S/N = 80$ for gY bands (on average, images in gY bands are shallower in depth and/or have higher background noise). The typical uncertainty of $\log(M_*/M_\odot)$ for both samples is around 0.08–0.10 dex at the high- M_* end. Please see Appendix.C for more detailed discussions of the SED fitting results.

4.2. Comparison with S82–MGC

Given the heterogeneous nature of the redshift resources for these samples, we further investigate their M_* completeness via comparing with galaxies that are in common with the S82–MGC sample. The S82–MGC sample matches the deeper SDSS photometric data in the Stripe 82 region ([Annis et al. 2014](#)) with the near infrared data from the United Kingdom Infrared Telescope Infrared Deep Sky Survey (UKIDSS; [Lawrence et al. 2007](#)). The deeper photometry and better photo-z make the S82–MGC sample complete to $\log(M_*/M_\odot) \geq 11.2$ at $z < 0.7$.

The match between the hscPho sample and the S82–MGC one results in 20453 galaxies at $0.3 \leq z \leq 0.5$ (referred as s82Pho sample). We estimate their M_* using cModel SED in exactly the same way. The M_* using HSC photometry shows tight correlation with ones based on the S82–MGC SED (five optical bands from SDSS and NIR data from UKIDSS; and S82–MGC also used iSEDFit under slightly different assumptions). Then we estimate the volume densities distributions of galaxies in cenHighMh, cenLowMh, and s82Pho samples (left panel of Fig.4) using rough estimates of the survey areas they occupied (since we only care about the relative shapes of the density distributions). And, we estimate the uncertainties of these distributions using a 10000 times bootstrap resampling. The distribution of cenLowMh sample starts to deviates from the s82Pho one below $\log(M_*/M_\odot) < 11.6$, indicating that the sample starts to become incomplete within $0.3 \leq z \leq 0.5$. As for the cenHighMh sample, their mass completeness should be better thanks to the reliable redMaPPer z_λ . Its behaviour is quite consistent with the mass function of galaxies in massive halos with a narrow M_{halo} distribution ([REF](#)). Later, we will see that the cModel photometry on average underestimate the M_* of galaxies with $\log(M_*/M_\odot) > 11.5$ by -0.1 dex. Therefore, we conclude that the cenLowMh becomes not perfectly complete below $\log(M_*/M_\odot) < 11.7$. This is most likely due to the incompleteness of the BOSS spec-z sample. Although it is unlikely that the incompleteness will bias the results of our comparisons, we will bear this in mind, and match the two samples carefully in $\log(M_*/M_\odot)$ and red-

shift space before comparing them.

4.3. Stellar Mass Corrected for Total Luminosity

Using the best-fit stellar mass from iSEDFit (referred as $M_{*,\text{cModel}}$), we estimate the average M_*/L_* in i -band, then use that M_*/L_* to convert the 1-D luminosity density profiles into stellar mass density profiles; and also convert the luminosity within 10 and 100 kpc apertures into corresponding stellar mass estimates (referred as $M_{*,10\text{kpc}}$ and $M_{*,100\text{kpc}}$). From now, we use $M_{*,100\text{kpc}}$ as the new proxy of “total” stellar mass of these galaxies. And we also derive the k -corrected luminosity and colors from the results. In Appendix.C, we also show the outputs like the average stellar age, metallicity, and internal dust extinction all behave reasonably for both samples, but will not use them for further scientific analysis.

As expected, the integration of 1-D profile out to very large radius help recover more luminosity (stellar mass) compared to the cModel results. We highlight this in the right panel of Fig.4 as we show the distributions of differences between $M_{*,100\text{kpc}}$ and $M_{*,\text{cModel}}$, and their relations to the $M_{*,100\text{kpc}}$. For both samples, we see the “extra mass” recovered by 1-D photometry increases with $M_{*,100\text{kpc}}$, therefore this improvement impacts the cenHighMh sample more. This is basically consistent with the fact that the structure of massive ETGs depends on its stellar mass in a way that more massive ones tends to be more extended (e.g. [REF](#)). Apparently, such mass-dependent difference between $M_{*,100\text{kpc}}$ and $M_{*,\text{cModel}}$ will result in difference of the SMF. As the slope and normalization of SMF at high mass end is very sensitive to both cosmology and interesting baryonic processes such as AGN feedback ([REF](#)), they are particularly important in constraining the galaxy evolution model, and therefore became the center of some intense arguments ([REF](#)). Although the jury is still out on this topic, it has become clear that popular results using SDSS photometry ([REF](#)) underestimate the total luminosity (stellar mass) of massive ETGs. However, past works (e.g. [REF](#)) often relied on either stacking of shallow images or the extrapolation of models to investigate this effect. Using the deep HSC images, we have the potential to answer this question much better. Detailed studies of SMF deserves more careful investigations of many systematic issues (e.g. [REF](#)), so we just show the impact of the “extra mass” on the volume density distributions of both samples (Fig.4, left panel). Generally speaking, the stellar mass corrected for total luminosity shifts the distribution toward the higher mass end, and slightly modify the slope. People who want to use HSC photometry or other cModel-like photometry to study the properties and evolution of SMF should be aware of such effect.

As mentioned earlier, our assumption of using an average M_*/L_* ignores its radial variation. It is well known that massive ETGs have negative optical color gradient which indicates a gradient of M_*/L_* (e.g. [La Barbera et al. 2012](#); [D’Souza et al. 2015](#)), but the gradient is smooth and shallow out to a few times of the effective radius (color gradient at the very outskirt is still not well quantified). And, for the comparison between the cenHighMh and cenLowMh samples, Our results should remain intact as long as there is no significant differences of color gradient between these two samples. We will discuss this more later, but initial results do suggest a smooth color gradient out to very large radius, and there is no systematic difference in color gradients of the two samples. Both suggest that the average M_*/L_* approach should work reasonably well for our goals.

And, we should mention that our approach is in principle

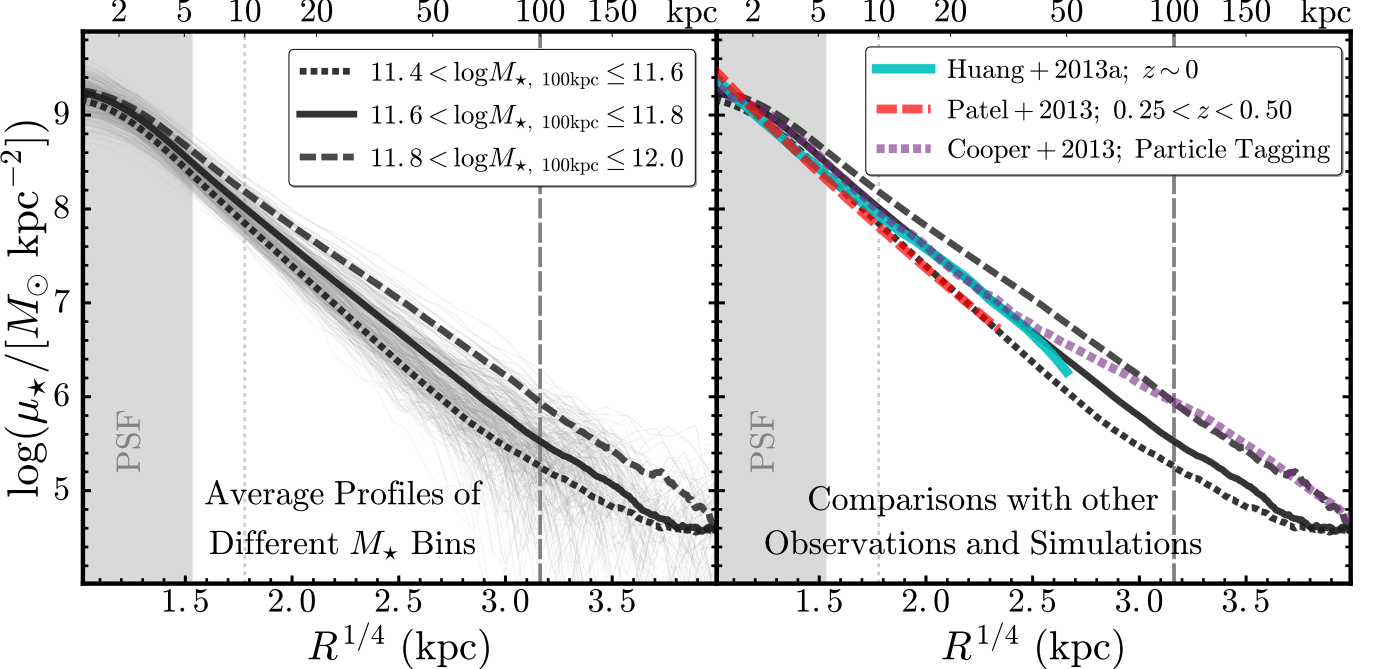


FIG. 5.— **Left:** Median μ_\star profiles of galaxies in different $M_{\star,100\text{kpc}}$ bins: $[11.4, 11.6]$ (short-dashed line), $[11.6, 11.8]$ (solid line), and $[11.8, 12.0]$ (long-dashed line). Here we combine the `cenHighMh` and `cenLowMh` samples, and we also show a random subset of individual profiles in the background. The shaded region highlights the region that could be affected by PSF. Two vertical lines label the radius of 10 kpc (thin, dotted line) and 100 kpc (thick, dash line). **Right:** comparison between the average μ_\star profiles with the ones from previous observations and simulations, including: 1) average profile of massive elliptical galaxies at $z \sim 0$ from Huang et al. (2013b, Cyan, solid); 2) average profile of massive galaxies at $0.25 \leq z < 0.50$ observed by *HST* from Patel et al. (2013, Red, long-dashed); 3) average radial stellar distributions in massive halos using simulation and particle tagging method (Cooper et al. 2013; Purple, short-dashed).

very similar to the one adopted by the GAMA survey (Taylor et al. 2011), where they start with M_\star estimated using average M_\star/L_\star from SED fitting results of PSF-matched aperture photometry, and later correct it with better estimate of total luminosity. However, the GAMA survey relied on multi-band single-Sérsic model fitting on the SDSS images to get total luminosity (Kelvin et al. 2012). It is therefore interesting to compare the M_\star ($M_{\star,\text{GAMA}}$ v.s. $M_{\star,100\text{kpc}}$) estimates for galaxies in common, given the differences in data and method. Please see the Appendix.D for more details. In short, we notice systematic differences between the two M_\star estimates, and it is likely that the GAMA models miss fluxes in the stellar halo that is beyond the depth of SDSS image.

In Appendix.A, we summarize the basic statistics of the `cenHighMh` and `cenLowMh` samples. In general:

- The two samples follow the same, tight “red-sequence” defined by k -corrected colors.
- The redshift distributions are reasonably similar in $0.3 < z < 0.5$, but the difference can still bias the comparison of μ_\star profiles.
- Although their $M_{\star,100\text{kpc}}$ overlaps a lot between $11.6 < \log(M_{\star,100\text{kpc}}/M_\odot) < 11.9$, the relative distributions within this bin are still very different.
- The distributions of $M_{\star,10\text{kpc}}$ overlaps the most between $11.2 < \log(M_{\star,10\text{kpc}}/M_\odot) < 11.6$, but the relative distributions also show difference within this $M_{\star,10\text{kpc}}$ range.

To compare their structural details, we will focus on `cenHighMh` and `cenLowMh` galaxies with $11.6 \leq \log(M_{\star,100\text{kpc}}/M_\odot) \leq 11.9$. Both samples have reasonable completeness in this $M_{\star,100\text{kpc}}$ range (see Fig.4).

In light of the differences in distributions of $M_{\star,100\text{kpc}}$, $M_{\star,10\text{kpc}}$, and redshift, we will carefully match these properties between the `cenHighMh` and `cenLowMh` samples to make sure the comparison is fair and meaningful. Please see the next section and Appendix.F for more details.

5. RESULTS

5.1. Comparison of Surface Mass Density Profiles

5.1.1. Internal Comparison and Comparison with Previous Works

As discussed earlier, although the mass-size scaling relation has been intensively discussed when it comes to the topic of environmental dependence of structure, it may not be the best tool to investigate this problem. Compared to the simple scaling relation, the detailed stellar mass density profiles contain much richer structural details that can help us diagnose the role played by different physical processes, including the environmental effect.

Before dive into more details, we first show the average μ_\star of massive galaxies at $0.3 < z < 0.5$ in three $M_{\star,100\text{kpc}}$ bins after mixing the `cenHighMh` and `cenLowMh` samples together⁹. For μ_\star profiles in each $M_{\star,100\text{kpc}}$ bin, we derive the median profile along with its uncertainty using bootstrap resampling method (5000 times). As one can see in the left panel of Fig.5, we can comfortably trace the M_\star distribution of these massive galaxies out to 100 kpc **individually**, which gives us huge advantage in studying the statistical properties of their outer envelopes. We can see that the higher $M_{\star,100\text{kpc}}$ shifts the median μ_\star profile up a little bit in the inner region, but makes the outskirts significantly more prominent.

⁹ Knowing that the two samples have different levels of completeness, here we simply mean to show the general properties of massive galaxies. In the first two $M_{\star,100\text{kpc}}$ bins, the `cenLowMh` galaxies dominate the number; while in the highest $M_{\star,100\text{kpc}}$ bin, the two samples have roughly the same size.

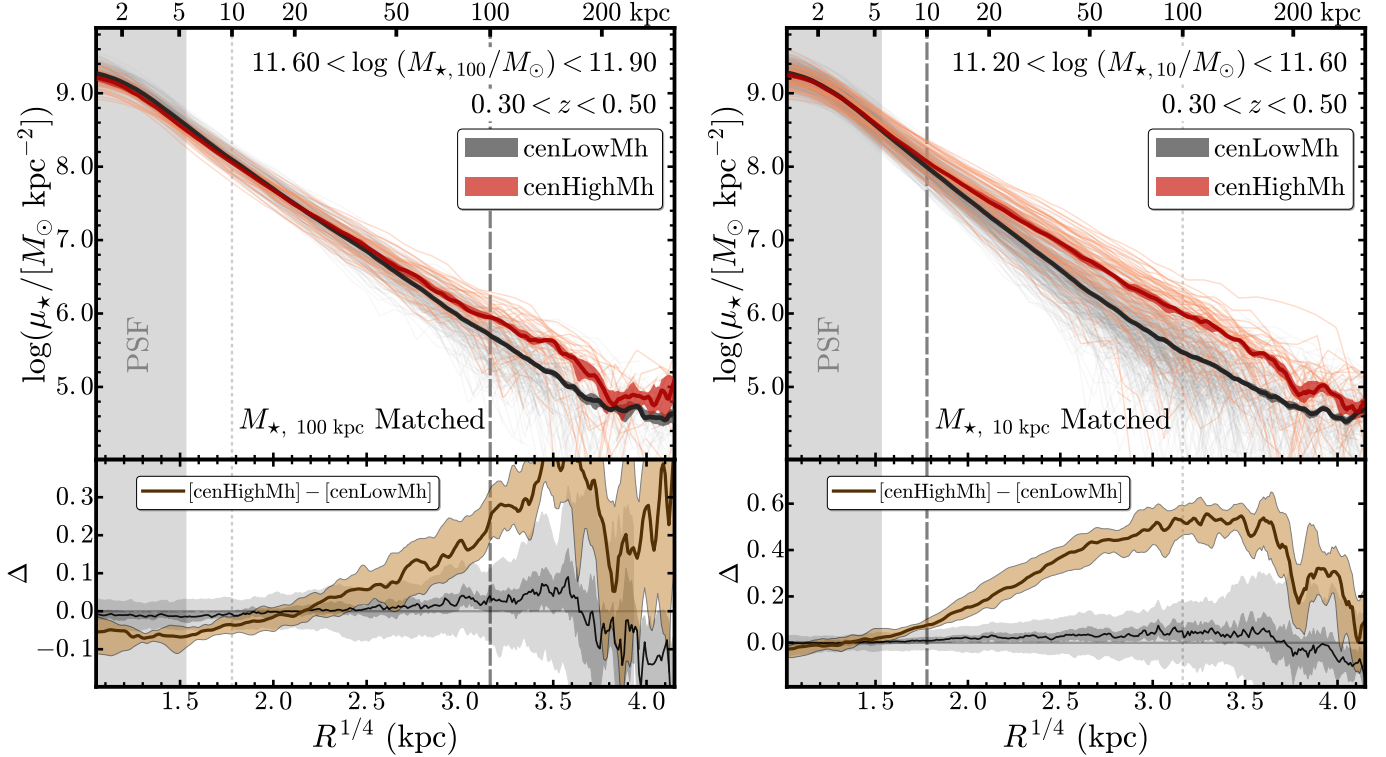


FIG. 6.— Comparison of the μ_* profiles for $M_{*,100\text{kpc}}$ -matched ($11.6 < \log(M_{*,100\text{kpc}}/M_\odot) < 11.9$) and $M_{*,10\text{kpc}}$ -matched ($11.2 < \log(M_{*,10\text{kpc}}/M_\odot) < 11.6$) samples of cenHighMh (orange to red) and cenLowMh (grey to black) galaxies. Left shows the results for the $M_{*,100\text{kpc}}$ -matched samples. For details of the matching process, please see Appendix F. On its upper panel, we show the μ_* profile of each galaxy using very light color in the background. We highlight the median profile and its corresponding uncertainties using thick solid line with darker color and shaded region. Other formats are the same with Fig. 5. Meanwhile, we highlight the difference between the median profiles and its uncertainty on the bottom panel (brown solid line and shaded region). To test the significance of the differential profile, we perform statistical tests by comparing the median profiles of two random groups that are drawn from the mixed sample, and have the same sizes with the matched cenHighMh and cenLowMh ones. Repeating this process many times, the median of these random differential profiles (black solid line), the $1-\sigma$ (dark-grey shaded region) and $3-\sigma$ (light-grey shaded region) uncertainties are shown on the bottom panel as well. A darker vertical dash-line highlights the 100 kpc radius. Right shows the results for the $M_{*,10\text{kpc}}$ -matched samples. The format is exactly the same with the left one, except that the darker vertical dash-line now highlights the 10 kpc radius.

Most of these very massive galaxies ($\geq 10^{11.4} M_\odot$) should be slow-rotating (e.g. Cappellari et al. 2013) giant ellipticals with “boxy” inner isophotal shape (e.g. Kormendy et al. 2009), and slightly flattened μ_* profile around the center (e.g. Lauer et al. 2007). But their structures in the outskirt clearly does NOT response to the increase of “total” stellar mass in a self-similar way.

In principle, this is consistent with result from HST observations of BCGs at $0.3 < z < 0.9$ (Bai et al. 2014) and the claimed positive correlation between luminosity and Sérsic index (e.g. Savorgnan et al. 2013)¹⁰; it is also consistent with the picture that more massive ETGs experienced more recent (minor) mergers.

In the right panel of Fig. 5, we compare these median profiles with a few past works. (Huang et al. 2013b), derived the median μ_* profile for a small sample of very nearby ellipticals from the Carnegie-Irvine Galaxy Survey (CGS, Ho et al. 2011). Individual profile and total luminosity were derived from three-component 2-D models that describe both very inner and outer luminosity distributions of these galaxies accurately. The average stellar mass of this sample is around $10^{11.3} M_\odot$. Due to the proximity of this sample (< 100 Mpc), the average profile is unaffected by seeing within ~ 1 kpc. Most galaxies of the CGS sample are not in any cluster. The

median profile qualitatively agrees with the median profile in the lowest $M_{*,100\text{kpc}}$ bin, especially in the inner region. Outside the inner 15 kpc, the CGS median profile shows a slightly more prominent outer envelope. While this could simply be due to the small size of the CGS sample (~ 30), interestingly, it is also consistent with the expectation if the mild mass growth from $z \sim 0.4$ to $z = 0$ mostly happened in the outskirt. The CGS images are already slightly deeper than SDSS images in r -band, however, the median profile can only reach to ~ 50 kpc (with much larger uncertainty compared to this work) for ETGs within ~ 100 Mpc. Such comparison clearly highlights the improvement made by the deep HSC images as individual profile of $z \sim 0.5$ galaxy is reliable out to at least 100 kpc.

Patel et al. (2013) extracted the median μ_* profile of massive ETGs in a similar redshift range with this work ($0.25 < z < 0.50$) using the stacked *HST/ACS* images. These galaxies are selected at a constant cumulative number density that makes them good candidates of progenitors of $z = 0$ massive ETGs. The median M_* is $\sim 10^{11.2} M_\odot$ according to their estimates. However, given the shallower depth of the ACS images and the usage of the BC03 model (each could cause -0.1 dex mass offset compared to this work), this sample should be comparable to the galaxies in the lowest $M_{*,100\text{kpc}}$ bin, and the comparison of their median profiles does reflect that. Moreover, the superb resolution of the *HST/ACS* image makes the μ_* profile unaffected by PSF even within inner 1 kpc, hence the comparison illustrates that the HSC profiles within our

¹⁰ But it does not mean such high Sérsic index model works well for massive ETGs as they fail at the inner-most region dramatically, and can not explain the radial variation of isophotal shape

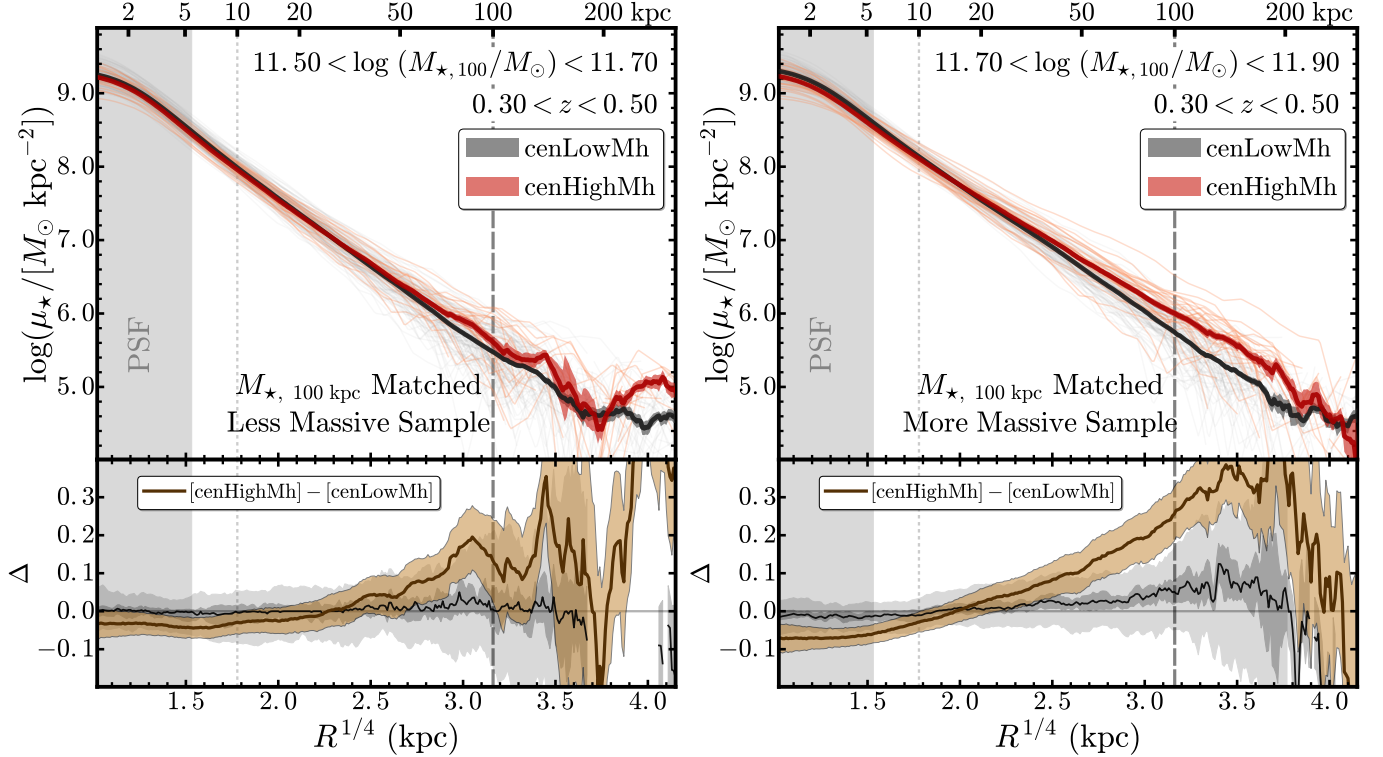


FIG. 7.— Comparisons of the μ_* profiles for $M_{*,100\text{kpc}}$ -matched cenHighMh (orange-red) and cenLowMh (grey-black) galaxies in lower (left; $[11.5, 11.70]$) and higher (right; $[11.7, 11.9]$) $M_{*,100\text{kpc}}$ bins. Other formats are in consistent with the right figure of Fig.6. The difference in median profiles is more significant in higher $M_{*,100\text{kpc}}$ bin.

redshift range are indeed not bothered by seeing outside the shaded region, and $M_{*,10\text{kpc}}$ should be very reliable. In fact, even M_* within 5 kpc should be available for comparison.

Besides these observations, we also compare with the predicted average μ_* profile of central galaxies in very massive halos ($13.5 < \log M_{200,c} < 14.0$) from cosmological simulation (Cooper et al. 2013). This is achieved by combining the detailed assembly information of halos from the dark-matter-only simulation with semi-analytic model and particle-tagging technique (Cooper et al. 2010). Although the physical resolution and detailed baryonic processes are not as “realistic” as state-of-art hydro-simulation, it is very efficient in providing rough stellar mass distributions in a large sample of massive halos. Without any adjustment, the profile is already quite similar to the median μ_* profile of galaxies in the $11.6 < \log(M_{*,100\text{kpc}}/M_\odot) < 11.8$ bin within 30-40 kpc. But the simulation seems to predict too significant envelope at larger radius for this average halo mass. Although we will not dig into the detailed causes of such differences, it already highlights that the comparison between deep μ_* profiles from observations and the predicted ones in simulations can be very interesting, especially in the outskirt that was rarely discussed using previous data.

We summarize the median profiles in Fig.5 in Table. 1, and all the above median profiles are available [here](#).

5.1.2. Environmental dependence of μ_* profiles at fixed $M_{*,100\text{kpc}}$

We show the results of the comparison in Fig.6 after carefully matching the cenHighMh sample with smaller size to the cenLowMh samples within $0.3 < z < 0.5$ and $11.6 < \log(M_{*,100\text{kpc}}/M_\odot) < 11.9$ via searching for the N nearest neighbours on the M_* -redshift plane using the KDTree algorithm. The details of the procedure and the evaluation of

the matching quality can be found in Appendix F. In summary, given the typical uncertainty of stellar mass, the two samples are well matched in $M_{*,100\text{kpc}}$; and their redshift distributions are broadly consistent with each other, hence we can perform meaningful comparison of their average structures at “fixed stellar mass” (median $\log(M_{*,100\text{kpc}}/M_\odot) \sim 11.74$). We also check their distributions of k -corrected colors ($g-r$), and confirm that they have similar color distributions as well.

For the 45 cenHighMh galaxies, we have 229 unique cenLowMh galaxies in the matched sample. On the left side of Fig.6, we plot the individual μ_* profile of cenHighMh and cenLowMh galaxies along with the median profiles of both samples. The uncertainties of the median profiles are derived using 5000 times of bootstrap resampling. The μ_* profile out to such large radius was only available for large sample of massive galaxies through image stacking method (e.g. (Tal & van Dokkum 2011; D’Souza et al. 2015)) which suffers from certain systematic issues. Although the μ_* profiles of many galaxies extend well beyond the 100 kpc radius, we notice that some profiles show signs of unphysical truncation that is caused by inaccurate background subtraction. Therefore, we will not include profiles outside 100 kpc in the comparison, even though the median profiles within 200 kpc still behave normally.

Once we match the distributions of $M_{*,100\text{kpc}}$, the μ_* profiles of massive galaxies in the cenHighMh and cenLowMh samples **greatly overlap with each other over the entire radius range**. At fixed “total” stellar mass, massive central galaxies in more massive halos do not form a unique population comparing to the ones from less massive halos in terms of their radial M_* distributions. This partially explains why the previous works have trouble finding any clear environmental dependence of structure.

At the same time, thanks to the high-quality individual profile from HSC image, we can also spot interesting differences in the median profiles of the $M_{*,100\text{kpc}}$ -matched `cenHighMh` and `cenLowMh` samples. In details, it seems that the central galaxies in more massive halos tend to have slightly flattened inner μ_* profiles while also possess more significant outer stellar envelope. To highlight such subtle structural features, we show the difference between the two median profiles and its uncertainty in the bottom panel. Given the noticeable uncertainties of $M_{*,100\text{kpc}}$ and λ , along with the small size of the current `cenHighMh` sample, we perform statistical test to confirm the robustness of the result: we mix the N_r `cenHighMh` galaxies and the N_n $M_{*,100\text{kpc}}$ -matched `cenLowMh` ones together, then randomly draw N_r galaxies with putting-back, compute the difference between the median profile of this sample and the `cenLowMh` sample. After repeating this process 2000 times, we can evaluate the possibility that the systematic differences in median μ_* profiles can be reproduced by random selection of massive galaxies. Comparing with the statistical distributions of the differential profiles from this test (grey shaded region), we can now conclude that the structural differences between `cenHighMh` and `cenLowMh` samples are significant. Apparently, the “transition radius” where the median profiles of `cenHighMh` and `cenLowMh` sample have the same μ_* is $\sim 15\text{-}20$ kpc, which is quite close to the expected R_e of ETGs at this $M_{*,100\text{kpc}}$ (please see next section for details).

To further test the robustness of this interesting result, we apply the above procedures to $M_{*,100\text{kpc}}$ -matched samples with slightly different definitions. The results are shown in Fig.21 in Appendix.G: (a). At higher redshift, the profile is affected more by the seeing at inner region, and by the imaging depth in the outskirt. Therefore, we compare the matched `cenHighMh` and `cenLowMh` samples within $0.3 \leq z < 0.4$, and the results are very similar. (b). We also make the comparison using a `cenHighMh` sample with lower average halo mass ($\lambda \geq 20$), the results are still stable (middle panel). We also check whether the structural differences are driven by small fraction of `cenHighMh` galaxies in very massive clusters. After removing the `cenHighMh` galaxies in clusters with $\lambda \geq 40$, the differences are as significant as above. (c). As noted before, the $M_{*,100\text{kpc}}$ is just a proxy of the total stellar mass. Given the differences we find, at fixed $M_{*,100\text{kpc}}$, `cenHighMh` galaxy tends to have slightly more prominent outer envelope outside 100 kpc than the `cenLowMh` one. Hence their real “total” stellar mass could also be slightly larger, and bias the comparison. Therefore, we make a similar comparison using the maximum M_* from the integration of the μ_* profile instead of the $M_{*,100\text{kpc}}$. In this case, the differences between the median profiles become slightly less significant as expected (a fraction of `cenHighMh` galaxies become more massive, and is not included in the $\log(M_{*,100\text{kpc}}/M_\odot) < 11.9$ mass bin). But the systematic trends, especially the differences in the low mass density outskirt are still very robust. We will further discuss this in Section 6. Considering the uncertainty of μ_* profiles outside 100 kpc, the feasibility of applying the average M_*/L_* to stars in the extreme outskirt, and the contribution of the diffuse stellar components that trace the halo, we think that our results are stable.

All these tests confirm that we robustly detect subtle, but systematic M_{halo} -dependence (environmental dependence) of structure in massive, central galaxies. Interestingly, the fact the it takes much better data and really cautious comparison to detect such systematic difference seems to suggest

that the role played by environment in shaping the structure of central galaxies may not be that crucial in the M_{halo} and M_* ranges we discussed.

At the same time, the systematic differences we find, especially the more extended stellar envelope of massive central galaxy in more massive halos, seem to be consistent with the expectation of richer (minor) merging history in denser environment. Predicted by the “two-phase” scenario, the non-dissipative mergers, especially the minor ones, should mainly deposit stellar mass in the outskirts, help build the stellar halo while do not change the inner μ_* profiles very much (e.g. Hilz et al. 2013, Oogi & Habe 2013).

We also explore the possible $M_{*,100\text{kpc}}$ dependence of such difference. Limited by the small sample we have, we can only afford to separate the samples into two $M_{*,100\text{kpc}}$ bins, and extend to slightly lower $M_{*,100\text{kpc}}$ bound ($11.5 \leq \log(M_{*,100\text{kpc}}/M_\odot) < 11.7$ and $11.7 \leq \log(M_{*,100\text{kpc}}/M_\odot) < 11.9$). After performing the same procedures of sample matching and comparison, we show the results in Fig.7. Although the smaller sample leads to larger statistical uncertainties, it is still interesting to see that the structural differences seem to be more significant in the higher $M_{*,100\text{kpc}}$ bin. For the lower $M_{*,100\text{kpc}}$ bin, the difference in the inner region becomes quite uncertain, while there is still evidence of difference in the outskirt. This result also has interesting implications in the assembly history of massive galaxies, and is worth more investigations with larger samples in the near future.

5.1.3. Environmental dependence of μ_* profiles at fixed $M_{*,10\text{kpc}}$

Here, we compare the median μ_* profiles of `cenHighMh` and `cenLowMh` galaxies after matching the two samples using $M_{*,10\text{kpc}}$ ($11.2 < \log(M_{*,10\text{kpc}}/M_\odot) < 11.6$) and redshift ($0.3 < z < 0.5$). We use the same matching procedure as in the previous section, and also put its evaluation in Appendix.F. As mentioned in the beginning, here we use $M_{*,10\text{kpc}}$ as the proxy of the M_* of the “in-situ” component. We will discuss this assumption more in the Section 6, but observations and simulations seem to support this claim in general. In the previous section, we investigate the environmental dependence of structure using “total” M_* ; here, we compare the massive galaxies in low- and high-mass halos that share similar amount of “in-situ” component.

As we can see in Fig.6 and the Appendix.E, the $M_{*,10\text{kpc}}$ is not affected by the physical size of PSF out to $z = 0.5$. For the 56 galaxies in this `cenHighMh` sample, we achieve excellent matching result using 375 `cenLowMh` galaxies (see Fig.20; median $\log(M_{*,10\text{kpc}}/M_\odot) \sim 11.35$). Using the same method, we show their individual profiles, and the comparison of their median μ_* profiles on the right side of Fig.6.

Unlike the $M_{*,100\text{kpc}}$ matched samples, here we see very striking differences that are already very significant even without any statistical test. It is easy to see that, when matched at the same $M_{*,10\text{kpc}}$, the μ_* profiles of `cenHighMh` and `cenLowMh` galaxies are quite similar in the inner 5-10 kpc. However, outside inner 10-15 kpc, the `cenHighMh` galaxies show much more prominent stellar envelope. Besides the differences in the median profiles, it is also worth discussing the distributions of individual μ_* profiles. Combining the `cenHighMh` and `cenLowMh` samples together, we should notice that the slope of the μ_* profile inside 10 kpc is quite uniform, and the dynamic range of the μ_* values is pretty small. On the other hand, the outer μ_* profiles of massive central galaxies can have a larger range of slopes. The ones from more massive halos on average have shallower outer μ_*

profiles, which is in qualitative agreement with recent simulation results (e.g. Pillepich et al. 2014). And, for both `cenHighMh` and `cenLowMh` samples, we find their outer profiles clearly have much larger dynamic range of μ_* values at fixed radius. This interesting diversity is also clearly illustrated by Fig.2, where we show the 3-color images of randomly selected massive central galaxies that have similar $M_{*,10\text{kpc}}$ ($11.1 \leq \log(M_{*,10\text{kpc}}/M_\odot) < 11.2$) but different $M_{*,100\text{kpc}}$. From the top-left to the bottom-right, the $M_{*,100\text{kpc}}$ of these galaxies increases from $10^{11.22} M_\odot$ to $10^{11.75} M_\odot$.

Putting together, these results indicate that massive central galaxies with similar M_* in the “in-situ” components share very similar radial M_* distributions in the inner region. Given the highly dissipative nature of the “in-situ” phase, this is consistent with the prediction that dissipative process like intense star-formation or wet-merger should create de Vaucouleur-like ($n \sim 4$) μ_* profile (e.g. Hopkins et al. 2008). On the other hand, the outer envelope of massive galaxies should be slowly assembled through non-dissipative accretion process, where merger history should play a essential role. Therefore, it is reasonable to see that the central galaxy of more massive halo has more significant stellar envelope than the one from lower mass halo at fixed M_* of their “in-situ” components.

Despite that the structural contrast is very clear using the median μ_* profile, we still perform a serious of tests to verify the robustness of the results. Changing the redshift range or the lower λ bound of the `cenHighMh` sample has no impact in the significance of the results; Replacing the $M_{*,10\text{kpc}}$ with the M_* within 5 or 15 kpc will result in very similar differences; And, unlike the $M_{*,100\text{kpc}}$ -matched samples, spitting the samples into two $M_{*,10\text{kpc}}$ bins (above and below $\log(M_{*,10\text{kpc}}/M_\odot) = 11.4$) reveals no apparent $M_{*,10\text{kpc}}$ -dependence of the structural differences. During the comparison, we notice that there is still tiny structural difference within 10 kpc (right figure of Fig.6). When we match the two samples using both $M_{*,10\text{kpc}}$ and $M_{*,15\text{kpc}}$, we notice that inner median μ_* profiles within 10 kpc becomes extremely similar (see Fig.20 in Appendix.F), while the differences in the outer part remain the same. Hence, for `cenHighMh` and `cenLowMh` galaxies that share not only the same inner mass, but also the same inner μ_* profiles, we still see significant environmental dependence in their overall structure.

When we match the two samples using $M_{*,10\text{kpc}}$, the matched samples have different $M_{*,100\text{kpc}}$ distributions (median $\log(M_{*,100\text{kpc}}/M_\odot) \sim 11.78$; median $\log(M_{*,100\text{kpc}}/M_\odot) \sim 11.64$). Although it is still safe to say that they represent very massive central galaxies, we also notice that the `cenLowMh` sample starts to include galaxies with $11.2 \leq \log(M_{*,100\text{kpc}}/M_\odot) < 11.6$. For one thing, our samples start to become quite incomplete below $\log(M_{*,100\text{kpc}}/M_\odot) \sim 11.5-11.6$; the satellite contamination could also increases toward lower $M_{*,100\text{kpc}}$ end. More importantly, when the $M_{*,100\text{kpc}}$ becomes very different, it is no longer comfortable to assume that they can share very similar “in-situ” components even at the same $M_{*,10\text{kpc}}$, as they could be in different phases of evolution. Therefore, we also match the two samples using $M_{*,10\text{kpc}}$ again, but only include the massive ones with $\log(M_{*,100\text{kpc}}/M_\odot) \geq 11.5$. Comparison between these more complete, purer samples of massive central galaxies shows very similar structural differences again (see the right side of Fig.20 in Appendix.F). In fact, their median profiles become even more similar in the inner region, suggesting that the results are very robust.

The median profiles shown in Fig.6 are available in Table.1.

5.2. Comparisons of ellipticity and optical-color profiles

In the above section, we focus on the 1-D μ_* profiles that are based on i -band image along. Although they already help us reveal interesting structural differences, we should not forget that the multi-band, 2-D HSC images of massive galaxies contain more information. Among them, the shapes and colors of different stellar components are particularly important to look into. Here, we extract the radial profiles of ellipticity and k -corrected optical colors of galaxies in both $M_{*,100\text{kpc}}$ -matched and $M_{*,10\text{kpc}}$ -matched samples (used in Fig.6) using `Ellipse`, and compare the average profiles between the `cenHighMh` and `cenLowMh` samples for two main purposes:

1. Since we derive the μ_* profiles using average isophotal shape, if these massive galaxies have steep or complicated elliptical profiles, or the two samples share very different elliptical profiles, the comparison of the average μ_* profiles could be biased. Therefore, we want to verify that photometry using average isophotal shape is appropriate for these samples. We extract ellipticity profiles in i -band using `Ellipse` by setting the geometric parameters free while forcing all isophotes share the same center.
2. As emphasized earlier, we apply the average M_*/L_* to derive M_* of these massive galaxies knowing that the M_*/L_* changes with radius. Although this may not be a critical issue when deriving “total” M_* , it certainly can bias the comparisons of μ_* profiles when two samples have very different M_*/L_* profiles. So we want to confirm that the application of average M_*/L_* is reasonable using the optical color profiles as tracer of M_*/L_* . After preparing the images in other bands in the same way with i -band ones, we derive color profiles by applying the isophotes from i -band to other images in a “forced photometry” mode.

Strictly speaking, we need better background subtraction and 2-D modeling method to accurately recover these information. But the straightforward methods applied here are sufficient for these purposes. We make no correction to the differences in background subtraction and PSF in different bands, therefore, we will simply ignore the shape and color information in the inner-most region and very low surface brightness regime. The profiles between 5-50 kpc should be useful. Here we only consider g and r band data as the ones in z and Y -band are often shallower, have worse seeing, and suffer more from background subtraction issues. We apply Galactic extinction and k -correction to both $g-r$ and $g-i$ color profiles; the k -correction values are also from iSEDFit results. We show the average ellipticity, $g-r$, and $g-i$ color profiles for the $M_{*,100\text{kpc}}$ -matched ($M_{*,10\text{kpc}}$ -matched) samples of `cenHighMh` and `cenLowMh` galaxies on the left (right) side of 8, and also compare them with previous estimates that are based on stacking analysis of SDSS galaxies (e.g. La Barbera et al. 2010; Tal & van Dokkum 2011; D’Souza et al. 2014).

Firstly, it is easy to see that massive central galaxies on average have positive ellipticity profiles. The ellipticity slowly, but steadily increase with radius from $e \leq 0.2$ around 5-10 kpc to $e \sim 0.3$ at 40-50 kpc. For the $M_{*,100\text{kpc}}$ -matched samples, their ellipticity profiles trace each other very well all the

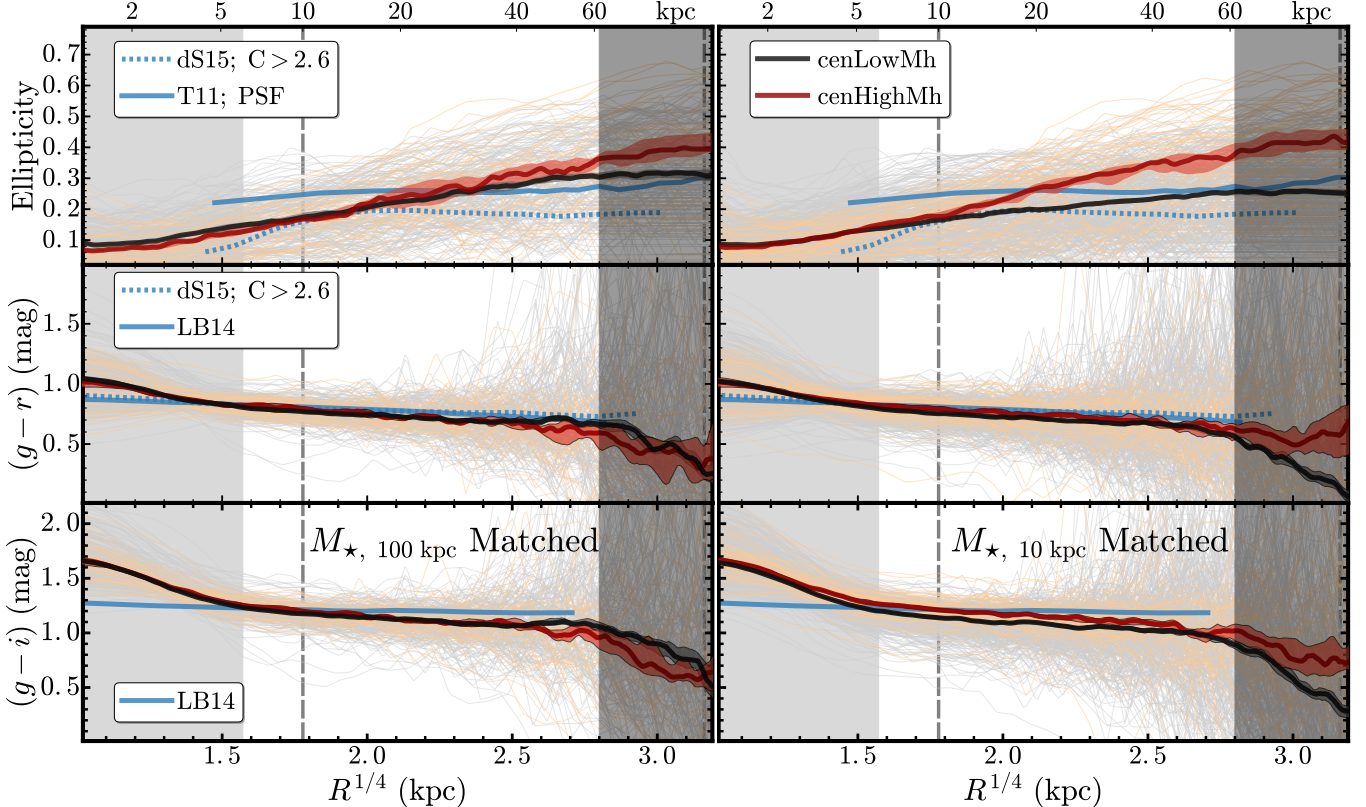


FIG. 8.— Comparisons of the radial profiles for ellipticity and optical colors for $M_{*,100\text{kpc}}$ -matched (**left figure**) and $M_{*,10\text{kpc}}$ -matched (**right figure**) of cenHighMh (orange-red) and cenLowMh (grey-black) samples. The formats are very similar to the figure for μ_* profile (e.g. right figure of Fig.6). On each side, from top to bottom, we show the elliptical profile, and the color profile using $g-r$ and $g-i$ color. Since the individual profile of these properties has very large uncertainty in the outskirt, we block the region at large radii where we think the median profiles are still unreliable using a dark, shaded box. We also compare these results with previous results based on SDSS images. They are: 1) Ellipticity profile of the stacked image of a large sample of red galaxies at $z \sim 0.4$ from [Tal & van Dokkum \(2011\)](#) with PSF correction (solid blue line on top panel); 2) Ellipticity and $g-r$ color profiles from stacking analysis of nearby massive galaxies with high concentration index ($C > 2.6$) in [D'Souza et al. \(2014\)](#), blue dash lines on the top and middle panels; 3) average $g-r$ and $g-i$ color profiles for a large sample of nearby elliptical galaxies in [La Barbera et al. \(2010\)](#), blue, solid lines on the middle and bottom panels).

way to 50 kpc ($2-3 \times R_e$ for their M_*); there might be hints that the cenHighMh ones have higher ellipticity at larger radius, but the isophotal fits with free geometry become very unstable at such low surface brightness region. This confirms that the comparisons of μ_* profiles using average isophotal shape is reasonable. On the other hands, when matched using $M_{*,10\text{kpc}}$, the cenHighMh galaxies show systematically higher ellipticity than the ones at $r > 10$ kpc, despite the ellipticity profiles at inner region are still very similar. Since the average ellipticity value is still quite low, and the slope of the profile is very shallow, the differences in ellipticity profiles will not affect the significant differences in μ_* profiles. And it further hints different assembly histories of the outer envelopes of central galaxies in different environments. These results are in consistent with the ones from 2-D decomposition in ([Huang et al. 2013b](#)): the outer envelopes of massive ETGs have higher ellipticity than the inner, “in-situ” dominated region; and become more elongated with M_* . As for the ellipticity profile, although it contains interesting information regarding the assembly history, it is difficult to estimate them down to very large radius. [Tal & van Dokkum \(2011\)](#) stacked the SDSS images of a large sample of Luminous Red Galaxies (LRGs) at $z \sim 0.4$, and extract the ellipticity profile after correcting the PSF convolution effect. Its slope is much shallower than the average ones using HSC images, despite the two samples are at similar redshift and are quite comparable. The poorer seeing condition of SDSS image plus the system-

atics in the stacking process can easily explain this. [D'Souza et al. \(2015\)](#) performed similar stacking analysis for a large sample of very nearby ETGs. The ellipticity profile is quite consistent with our average ones within 5-10 kpc, but become much shallower at outer region. The lower average M_* of their sample and/or the uncertainties in the stacking analysis may explain this. This highlights the advantages of the high-resolution, deep HSC images again, and it would be very interesting to compare with numerical simulations.

Secondly, we see shallow and negative gradients of average $g-r$ and $g-i$ color profiles for both cenHighMh and cenLowMh galaxies after excluding the unreliable regions. On the left of Fig.8, we see that the cenHighMh and cenLowMh samples share very similar color profiles from 5-50 kpc. This is very good news for using average M_*/L_* in the comparisons of μ_* profiles: although the μ_* profiles may not be perfectly accurate, there should be no bias when comparing the average profiles of cenHighMh and cenLowMh samples. On the right side of Fig.8, the situation is very similar as the slopes of color gradients are basically the same for two samples; although there might be some evidence that, when matched at similar M_* of the “in-situ” component, the cenHighMh galaxies tend to have slightly redder envelopes than the cenLowMh ones. This is worth further investigation, especially via multi-band, 2-D decomposition method. Ignoring the tiny differences between the corresponding HSC and SDSS filters, we see quite consistent $g-r$ color profiles;

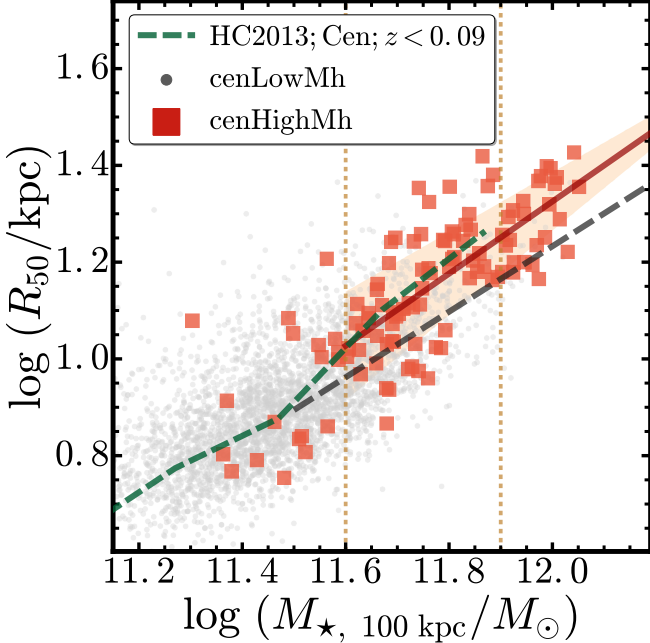


FIG. 9.— The M_* -size relations for cenHighMh (orange-red circles) and cenLowMh (grey dots) galaxies. Here we use the $M_{*,100\text{kpc}}$ as proxy of total M_* , and use the R_{50} derived from the 1-D profile as size estimate. Two vertical lines highlight the $11.6 < \log(M_*/M_\odot) < 11.9$ mass bin. We visualize the best-fit M_* - R_{50} relations of cenHighMh (red, solid line) and cenLowMh (grey, dash line) galaxies at high- M_* end. The shaded regions in lighter colors show the $1-\sigma$ uncertainties from MCMC sampling. We also compare with the M_* - R_{50} relation for nearby central galaxies in massive groups from [Huertas-Company et al. \(2013\)](#) (green, long dashed line). Please refer to the text for more details.

but the $g-i$ profiles become slightly steeper using HSC images. Although the exact cause of this difference is not clear, it is worth noting that the SDSS i -band images suffer from the “red-halo” effect of extended PSF wing (e.g. [Wu et al. 2005](#), [Tal & van Dokkum 2011](#)) which could make the color at larger radius appear redder. Thank to the thickness of the CCD, the HSC i -band images do not have this problem, hence can provide more accurate color estimates.

Although the 1-D analysis is not perfect, these preliminary results already point out the importance and benefits of including multiband, 2-D information into account. Now we know that, for massive central galaxies with similar $M_{*,100\text{kpc}}$, the average μ_* profiles show subtle dependence on halo mass, while the color and ellipticity profiles are very stable. On the other hands, for central galaxies that have the same M_* , ellipticity and color profiles within 10 kpc, their outer envelopes appears to be strongly depend on environments.

5.3. Explore Different Scaling Relations

5.3.1. M_* -size relation

The scaling relation between M_* and effective radius (or half-light radius; R_e or R_{50}) was the focus of previous investigations of the structural evolution (e.g. [Shankar et al. 2013](#); [Leja et al. 2013](#), [van der Wel et al. 2014](#)) and the environmental dependence of structures for massive galaxies (e.g. [Weinmann et al. 2009](#), [Nair et al. 2010](#), [Huertas-Company et al. 2013](#), [Cebrián & Trujillo 2014](#)). So far, the results are quite confusing as no clear evidence of environmental dependence has been found at low redshift using various definitions of “size”. And the observations become controversial at intermediate and high redshift (e.g. [Cooper et al. 2012](#), [Papovich et al. 2012](#), [Kelkar et al. 2015](#)). Through careful comparisons

of μ_* profiles at fixed $M_{*,100\text{kpc}}$ and $M_{*,10\text{kpc}}$, we clearly show that the structure of massive central galaxies at $0.3 < z < 0.5$ depend on the halo mass in a subtle but systematic manner. Therefore, we also expect to see such evidence on the M_* -size relations of cenHighMh and cenLowMh galaxies (see Fig.9).

We choose to use the $M_{*,100\text{kpc}}$ as the proxy of “total” M_* , and use the radius that encloses 50% of luminosity within 100 kpc (R_{50}) as the “size” to evaluate the relation. We use the curve-of-growth of luminosity from the Ellipse run on i -band images to estimate the R_{50} here. This 1-D approach is more sensitive to issues like the smearing effect of PSF and the choice of aperture for maximum luminosity than the 2-D fitting method. But, for the massive galaxies in this work, their apparent sizes are always sufficiently large at $0.3 \geq z \geq 0.5$ so that the R_{50} measurements are not bothered by seeing. At the same time, this 1-D method has the advantages of being less affected by the accuracy of background subtraction, structural details, and model assumptions.

On Fig.9, we see clear M_* -size relations for both samples. At fixed $M_{*,100\text{kpc}}$, the distributions of R_{50} for the cenHighMh and cenLowMh galaxies greatly overlap. Meanwhile, it seems that the cenHighMh galaxies do have a slightly higher R_{50} . For the $M_{*,100\text{kpc}}$ -matched samples used in Fig.6, the median $\log(R_{50}/\text{kpc})$ values for the cenHighMh and cenLowMh are 1.22 ± 0.02 ($\sim 17.4 \pm 0.75$ kpc) and 1.09 ± 0.01 ($\sim 12.3 \pm 0.3$ kpc), which confirm the above observation and is consistent with the differences seen in Fig.6. However, most previous works that we are aware of did not match the M_* and redshift distributions between different samples, and often focused on the shape of the $\log(M_*/M_\odot)$ - $\log R_e$ relation. Here, we try to derive the best-fit parameters for the $\log(M_{*,100\text{kpc}}/M_\odot)$ - $\log(R_{50}/\text{kpc})$ relations of galaxies with $\log(M_{*,100\text{kpc}}/M_\odot) \geq 11.6$ using MCMC-sampling method via the ensemble sampler emcee ([Foreman-Mackey et al. 2013](#)). Using initial guesses based on maximum likelihood estimates, and assuming reasonable flat priors, we derive best-fit relations for the massive cenHighMh galaxies:

$$\log(R_{50}/\text{kpc}) = (0.73 \pm 0.13) \times \log(M_{*,100\text{kpc}}/M_\odot) - (7.49 \pm 1.56) \quad (1)$$

And for the massive cenLowMh galaxies, we have:

$$\log(R_{50}/\text{kpc}) = (0.68 \pm 0.06) \times \log(M_{*,100\text{kpc}}/M_\odot) - (6.88 \pm 0.75) \quad (2)$$

As shown in Fig.9, at the high-mass end, the two relations have consistent slopes within their uncertainties, but different normalizations. Extending the fitting to the full $\log(M_{*,100\text{kpc}}/M_\odot)$ range does not change this result. We also explore mass-size relations for our samples using M_* within different radius (e.g. 120, 150 kpc) and the R_{50} derived within these apertures, and find consistent results.

We qualitatively compare our results with the one for $z \leq 0.09$ central ETGs in $14 \leq \log(M_{\text{Halo}}/M_\odot) < 15$ halos from [Huertas-Company et al. 2013](#) (HC13; green solid line). HSC13 used the group catalog by [Yang et al. \(2007\)](#) to estimate $\log(M_{\text{Halo}}/M_\odot)$. They estimated the 2-D R_e using single-Sérsic model fitting to SDSS images, and derived M_* based on SED fitting using the BC03 ([Bruzual & Charlot 2003](#)) synthetic population model. We empirically convert their M_* from the Kroupa IMF to the Chabrier one used in this

work by applying a constant -0.05 shift to their values (see ?). We also increase the M_* in HC13 by +0.1dex to account for the systematic difference between their BC03 and our FSPS model (see Appendix.C). In HC13, the authors found no difference among the mass-size distributions for central galaxies in halos across $12.5 \leq \log(M_{\text{Halo}}/M_\odot) < 15.0$. Despite all the systematic differences, the mass-size distributions for both cenHighMh and cenLowMh galaxies follow the HC13 relation reasonably well (with slightly shallower slopes) even at $\log(M_{*,100\text{kpc}}/M_\odot) < 11.6$ where our samples start to become incomplete.

In short, we confirm that the massive central galaxies in this work generally follow the M_* -size relation for massive ETGs at low- z . More importantly, we find that the M_* -size relations at high- M_* end depends on M_{halo} , suggesting that the central galaxies in denser environment (higher M_{halo}) have slightly larger R_{50} comparing to the ones from smaller haloes at fixed $M_{*,100\text{kpc}}$.

It would be interesting to revisit this topic using 2-D models based on deep HSC images as the next step. It is worth noting that our results are based on massive galaxies at $z \sim 0.4$, while the sample of HC13 has $z < 0.09$. Although here we can not study the redshift evolution of M_* -size relation here, it will be interesting to see whether the structural evolution of massive galaxies between $z \sim 0.4$ and 0.0 also depends on environment. If the cenHighMh galaxies experienced more mergers than the cenLowMh ones during this time, we should expect that M_* -size relation shows stronger environmental dependence at $z \sim 0.0$ using deeper image than SDSS. On the other hand, if the cenLowMh galaxies could assemble more M_* through minor mergers in the last 3-4 Gyrs, they could potentially “catch-up” with the cenHighMh galaxies on the M_* -size plane, and makes it harder to find the environmental dependence in nearby universe. In principle, we can make uses of the frequency of tidal features and the numbers of satellites around our cenHighMh and cenLowMh galaxies to make some predictions in the near future.

5.3.2. Relations between stellar mass within different physical apertures

We just show that the M_* -size relation of massive central galaxies also depends on the M_{halo} or environment, and now we explore relationships between M_* within different apertures as alternative tools to help us better understand the relationship between M_{halo} and the assembly history of massive galaxies. Here we focus on $M_{*,100\text{kpc}}$, $M_{*,10\text{kpc}}$, and also the logarithmic mass differences between them ($\Delta \log M$, reflecting M_* ratio). Comparing to the M_* -size relation, such relations are not affected by the ambiguous definition of “size”; and comparing to the detailed μ_* profiles, it is much easier to apply these relations to larger samples or to compare with simulations.

We show the results in Fig.10. In panel (a), we plot the $M_{*,100\text{kpc}}$ with $\Delta \log M$ for both the cenHighMh and cenLowMh samples. As expected, these two parameters well trace each other over the entire range of $M_{*,100\text{kpc}}$, indicating that more massive central galaxies have larger fraction of total M_* in their outskirts. Suggested in Fig.7, the structural differences related to M_{halo} seem to be more significant in the higher M_* bin. We therefore highlight the $M_{*,100\text{kpc}}$ -matched cenHighMh and cenLowMh galaxies at $11.7 \leq \log(M_{*,100\text{kpc}}/M_\odot) < 11.9$. Although the $\Delta \log M$ distributions still greatly overlap at high- $M_{*,100\text{kpc}}$ end, their median values (big, outlined symbols with error bars), and

kernel-density distributions clearly reveal systematic difference. Consistent, but slightly smaller, difference also exists for $M_{*,100\text{kpc}}$ -matched samples at $11.6 \leq \log(M_{*,100\text{kpc}}/M_\odot) < 11.9$.

At the same time, the comparisons in Fig.6 and Fig.7 also suggest that the $M_{*,100\text{kpc}}$ -matched cenHighMh galaxies have lower $M_{*,10\text{kpc}}$ than the cenLowMh sample. When we plot $\Delta \log M$ with $M_{*,10\text{kpc}}$ for the $M_{*,100\text{kpc}}$ -matched samples in panel (b), we can easily confirm this result. The correlation between $\Delta \log M$ and $M_{*,10\text{kpc}}$ is quite weak for the cenLowMh galaxies, but still visible. However, we see no apparent correlation between $\Delta \log M$ and $M_{*,10\text{kpc}}$ for the cenHighMh galaxies. We also construct $\Delta \log M$ using logarithmic mass differences between 100 and 30 (or 50) kpc, and the results are very similar. These reflect the structural differences we found in Fig.6: at fixed $M_{*,100\text{kpc}}$, central galaxy in more massive halo tends to have even higher fraction of M_* stored between 10 and 100 kpc than the one from smaller haloes.

In panel (c), we show the relationship between $M_{*,100\text{kpc}}$ and $\Delta \log M$ again, but highlight the $M_{*,10\text{kpc}}$ -matched samples showed in right panel of Fig.6. Their distributions clearly show the impact of the much more prominent outer envelope hosted by cenHighMh galaxies through the differences in $M_{*,100\text{kpc}}$ and $\Delta \log M$ of the $M_{*,10\text{kpc}}$ -matched samples.

Finally, in panel (d), we plot $M_{*,100\text{kpc}}$ against $M_{*,10\text{kpc}}$ directly. It is intriguing to see that the distributions of cenHighMh and cenLowMh galaxies on this 2-D plane seem to be offset with each other. At least at the high mass end, the central galaxies in more and less massive halos seem to follow $M_{*,100\text{kpc}}-M_{*,10\text{kpc}}$ relations with similar slopes, but different normalizations. Instead of “arbitrarily” grouping galaxies into different bins of $M_{*,100\text{kpc}}$ or $M_{*,10\text{kpc}}$, such scaling relation brings us a more generic view of the environmental dependence of structure, and could help us better investigate the relations among halo mass, assembly history, and the structure of massive galaxies. On Fig.10 (d), we illustrate the $M_{*,100\text{kpc}}-M_{*,10\text{kpc}}$ relations at $\log(M_{*,100\text{kpc}}/M_\odot) \geq 11.6$ that are derived using MCMC sampling method. For cenHighMh galaxies, the best-fit relation is:

$$\log(M_{*,10\text{kpc}}/M_\odot) = (0.48 \pm 0.06) \times \log(M_{*,100\text{kpc}}/M_\odot) + (5.72 \pm 0.75). \quad (3)$$

In the same range of $M_{*,100\text{kpc}}$, the best-fit relation for cenLowMh is:

$$\log(M_{*,10\text{kpc}}/M_\odot) = (0.56 \pm 0.03) \times \log(M_{*,100\text{kpc}}/M_\odot) + (4.82 \pm 0.30). \quad (4)$$

Fitting this relation in the full $M_{*,100\text{kpc}}$ range results in even shallower slope for the cenHighMh galaxies. Also, replacing the $M_{*,10\text{kpc}}$ with M_* within 5 or 15 kpc apertures does not change our conclusions. In fact, the relation using $M_{*,5\text{kpc}}$ shows more significant M_{halo} dependence at the high-mass end. Unfortunately, due to the impact of PSF, the $M_{*,5\text{kpc}}$ values are less reliable than $M_{*,10\text{kpc}}$. Samples at lower redshift, images with higher spatial resolution, and 2-D modeling analysis can help us push the investigation further into smaller radius, and help us develop better proxy for the M_* of the “in-situ” component.

Limited by our capability to estimate M_{halo} with better accuracy or individually, we can not further quantify this M_{halo} -

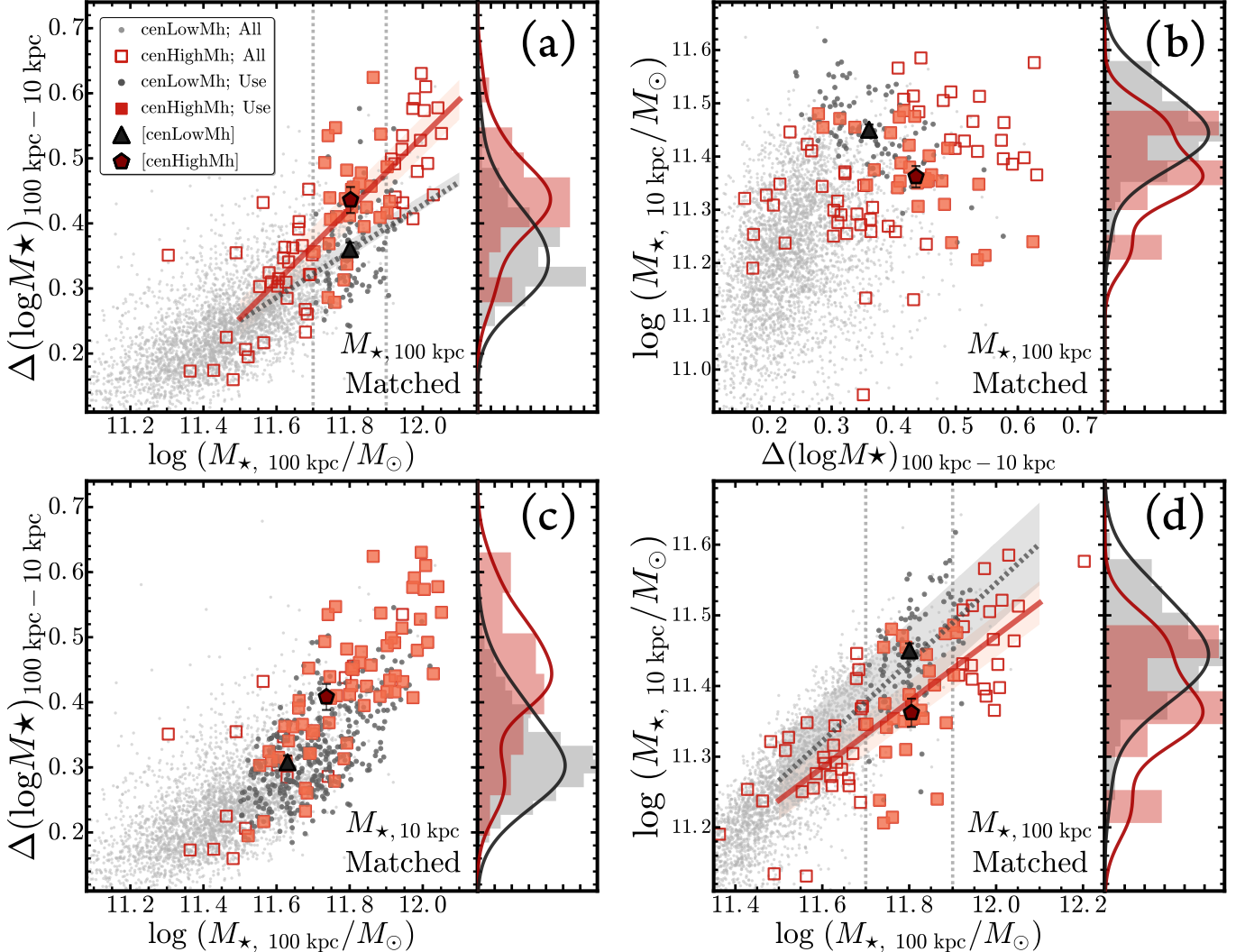


FIG. 10.— (a): Distributions of galaxies on the $M_{\star,100\text{kpc}}-\Delta(\log M_{\star})_{100\text{kpc}-10\text{kpc}}$ plane. All cenHighMh (open red boxes) and cenLowMh (light, grey dots) galaxies are shown in the background. The $M_{\star,100\text{kpc}}$ -matched samples between $11.6 < \log(M_{\star}/M_{\odot}) < 11.9$ (between two vertical lines) are highlighted (cenHighMh: solid red boxes; cenLowMh: bigger grey dots). We also show the median values (solid triangular and hexagon), and the distributions of $\Delta(\log M_{\star})_{100\text{kpc}-10\text{kpc}}$ (both histograms and kernel density distributions on the right). The best scaling relations for cenHighMh (red, solid) and cenLowMh (grey, dashed) galaxies along with their uncertainties are illustrated as well. (b): Distributions of galaxies on the $\Delta(\log M_{\star})_{100\text{kpc}-10\text{kpc}}-M_{\star,10\text{kpc}}$ plane. (c): Distributions of galaxies on the $\Delta(\log M_{\star})_{100\text{kpc}-10\text{kpc}}-M_{\star,100\text{kpc}}$ plane. But, this time, we highlight the cenHighMh and cenLowMh samples that are matched using $M_{\star,10\text{kpc}}$ instead of $M_{\star,100\text{kpc}}$. (d): Relations between $M_{\star,100\text{kpc}}$ and $M_{\star,10\text{kpc}}$. Other formats of figure (b), (c), and (d) are very similar with figure (a).

dependence here. Albeit that the redMaPPer richness (λ) traces M_{halo} reasonably well, we do not find any clear correlation with λ within the cenHighMh galaxies. In the current sample, most of the cenHighMh galaxies are centrals of clusters with $30 \leq \lambda \leq 40$, and only a small fraction comes from more massive clusters. Therefore, the small sample size, the uncertainties of richness from shallow SDSS images, and the intrinsic scatter of the $\lambda-M_{\text{halo}}$ relation may conspire to stop us from extracting more information from this M_{halo} -dependence.

The M_{halo} -dependence of structure in massive central galaxies could be the result of many different physical processes. It would be very interesting to compare with progenitors of these massive galaxies at higher redshift and with the results of numerical simulations (e.g. see Fig.1 of Wellons et al. 2016) via the $M_{\star,100\text{kpc}}-M_{\star,10\text{kpc}}$ or similar relations.

In the past decade, the mass assembly and structural evolution of massive ETGs remains as an active topic. More and more convincing observations of massive galaxies at high redshift reveal that the progenitors of massive elliptical galaxies are quite different in structure comparing with their local decedents (e.g. REF). Collectively, they need to increase their “size” (R_e) by a factor of 2 to 4 (e.g. REF) without changing their inner μ_{\star} profile (e.g. REF) and central stellar velocity dispersion (e.g. REF) much in the last 8-10 Gyrs. Owing mainly to better numerical simulations, the challenge of “size”-evolution seems to be eased by the promising “two-phase” scenario under the framework of hierarchical formation of galaxy (e.g.REF). Under this picture, the inner region of massive galaxies mostly consist of stars formed within the halo of the main progenitor through intense dissipative processes at high redshift. Later, after the active star formation is quenched in these massive systems, their mass assembly history becomes dominated by accretions of satellites. Based on the prediction of merger tree and current understanding

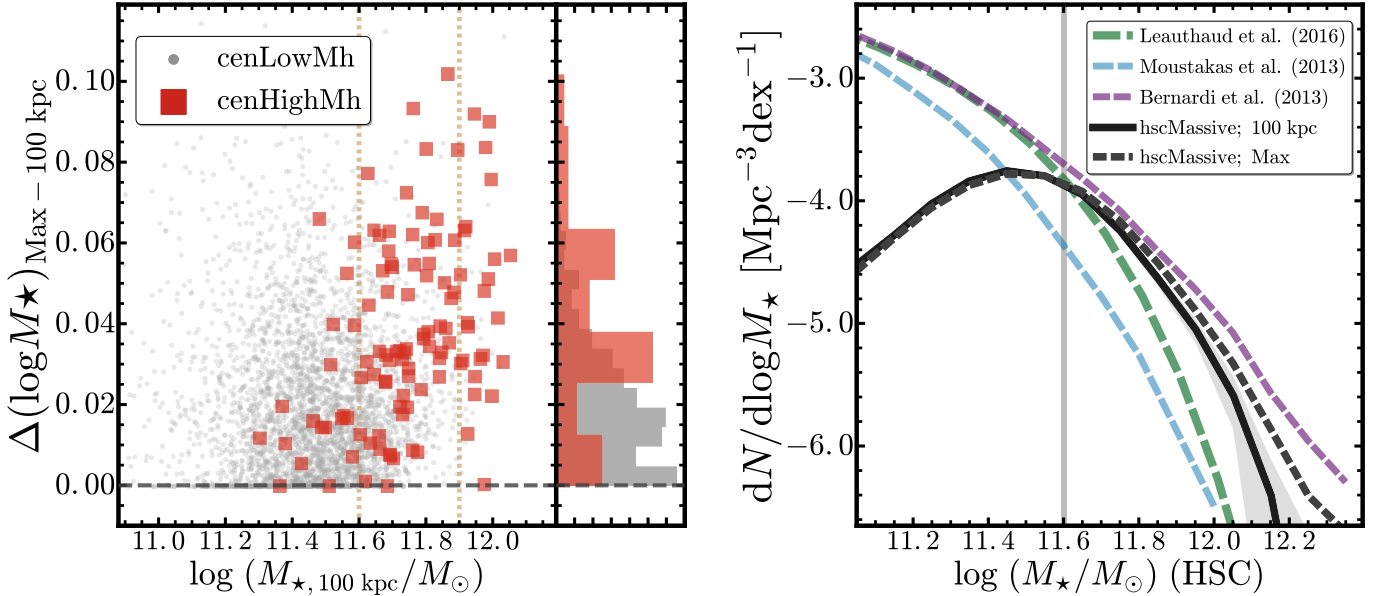


FIG. 11.— **Left:** Relation between $M_{\star,100\text{kpc}}$ and the logarithmic mass difference between $M_{\star,\text{Max}}$ and $M_{\star,100\text{kpc}}$ for both *cenHighMh* (red square) and *cenLowMh* (grey dot) galaxies. The format is very similar to the left figure of Fig.4. **Right:** The stellar mass volume-density distributions of massive galaxies after combining the *cenHighMh* and *cenLowMh* samples together, using both $M_{\star,100\text{kpc}}$ (black solid line) and $M_{\star,\text{Max}}$ (black dash line). The uncertainty for distribution using $M_{\star,100\text{kpc}}$ is shown in grey shaded region. Here, we also compare the distributions with SMF from previous works: (a): SDSS galaxies at $z \sim 0.1$ from Bernardi et al. (2013); the M_\star is based on photometry from 2-D Sérsic +Exponential model fitting; (b): SDSS galaxies at $z \sim 0.1$ from Moustakas et al. (2013) based on improved SDSS cModel photometry; (c): S82–MGC galaxies at $0.15 < z < 0.43$ from Leauthaud et al. (2016) based on PSF-matched SDSS–UKIDSS photometry. Please see text for more details of the comparison.

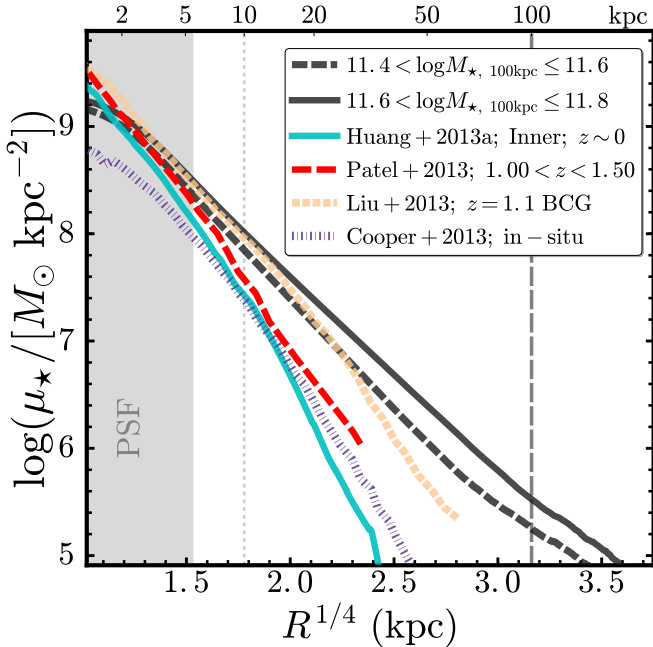


FIG. 12.— Comparison of the average μ_\star profiles of massive galaxies in the two lower $M_{\star,100\text{kpc}}$ bins from Fig.5 with other observations and simulations, focusing on the inner region. The format is similar with the right panel of Fig.5. We include: 1) the average μ_\star profile of inner component from structure decomposition of massive elliptical galaxies at $z \sim 0$ from Huang et al. (2013b, Cyan, solid); 2) the average μ_\star profile of massive galaxies at $1.0 < z < 1.5$ from HST observations in Patel et al. (2013, Red, dashed); 3) the average μ_\star profile of the “in-situ” stellar components in simulated massive halos from Cooper et al. (2013, Purple, dot-dashed); 4) the μ_\star profile of the very massive cD galaxy at $z \sim 1.1$ discovered by Liu et al. (2013, Yellow, dashed) in the Hubble Ultra-Deep Field.

of satellite population around massive galaxies, most these merging events are likely to be minor ones, and without involving much gas dissipation. Since such minor, dry merger

basically redistributes stars onto the outer envelope of the central galaxy, it becomes the most promising solution to the “size-evolution” puzzle. However, it raises additional questions at the same time. The most pressing one would be the expected “environmental”-dependence of structures of massive central galaxies. As minor merger is expected to be more frequent in denser environment, the mass assembly history and M_\star distribution of central galaxies should show dependence on M_{halo} or even other properties of the host halo. For instance, centrals in more and less massive halos could have different slopes and/or scatters in their mass-size relation (e.g. REF). Yet, no clear evidence of such dependence has been found. In this work, taking advantage of the deep photometry from the HSC survey and looking into the detailed μ_\star profiles, we clearly see evidence that the **structure of massive central galaxies, both the inner and outer parts, does show dependence on the halo mass**. Here, we briefly discuss the physical causes of this dependence, potential caveats, and more scientific implications.

Firstly, the comparisons of the μ_\star profiles suggest that M_{halo} **does not play a central role in shaping the structure of massive central galaxies**. It appears that massive central galaxies at $\log(M_\star/M_\odot) \geq 11.5$ were shaped by same physical processes in more and less massive halos. At both fixed $M_{\star,100\text{kpc}}$ and $M_{\star,10\text{kpc}}$, centrals from cluster-level halos do not form a unique population. Instead, their individual μ_\star profiles greatly overlap with the ones in halos of small group. At similar $M_{\star,100\text{kpc}}$, even their median μ_\star profiles only show quite subtle differences. For the *cenHighMh* sample, this is similar to the results of (Zhao et al. 2015) that a considerable fraction of nearby BCGs (34%) does not fall into the “cD” class. From the smooth distributions of μ_\star profiles on Fig.6 and Fig.22, it is even harder to draw a clear difference between “cD” galaxy and “normal elliptical”.

At the same time, **the M_{halo} -dependence we found do fit the expectations of the “two-phase” scenario at first**

glance. For central galaxies with similar stellar mass at the end of the first phase, their subsequent, accretion-dominated mass assembly naturally relates to M_{halo} , which determines the number and mass distributions of satellites. Therefore, centrals of more massive halos should accumulate more extended stellar envelope during the second phase, exactly as we find in the μ_* profile comparison of the $M_{*,10\text{kpc}}$ -matched samples (see Fig.22). Under the “two-phase” formation scenario, the stellar content of massive galaxies can be broadly separated into the “in-situ” and “accreted” components. At fixed $M_{*,100\text{kpc}}$, the differences of median μ_* profiles could reflect different relative fraction of these two components. Recent simulations indicate that (1) the fraction of accreted stars could have a steep correlation with total stellar mass; (2) for $\log(M_*/M_\odot) \geq 11.5$ galaxies, the accreted component starts to dominate within the R_e . Given that (1) the “transition radius” between the two median profiles is around 15-20 kpc (see Fig.6); and (2) the differences become more significant at higher mass end, it is likely the M_{halo} -dependence of structure at fixed total stellar mass is driven by the higher fraction of accreted stars in more massive halos. To confirm this inference, in Fig.11, we compare the median μ_* profiles of the $M_{*,100\text{kpc}}$ -matched cenHighMh and cenLowMh samples at $11.5 \leq \log(M_*/M_\odot) < 11.7$ with the median profiles of (1) massive ETGs at $1.0 < z < 1.5$ that are considered the progenitors of $\sim 10^{11.5} M_\odot$ ETGs at $z = 0$ (Patel et al. 2013). After this redshift range, their mass growth should be dominated by mergers. (2) inner components of $z = 0$ $10^{11.4} M_\odot$ ellipticals from 2-D decomposition (Huang et al. 2013b). (Huang et al. 2013a) showed that these structures are quite similar to the compact progenitors at higher redshift in many aspects. (3) the “in-situ” components of simulated galaxies in massive halo of (Cooper et al. 2013) using particle-tagging technique (the inner few kpc is quite uncertain due to the resolution). Regardless the small difference in median M_* and details in M_*/L_* estimates, the comparison first confirms that $M_{*,10\text{kpc}}$ is indeed not a bad proxy of the in-situ mass; meanwhile, it also highlights that structural difference between cenHighMh and cenLowMh are driven by region that is not dominated by “in-situ” stars. Since most of these samples in comparison are not as extreme as the massive cenHighMh galaxies, we also compare with a uniquely massive BCG at high redshift: a $10^{11.4} M_\odot$ BCGs with distinctive envelope at $z \sim 1.1$ (Liu et al. 2013). It is interesting to see that its μ_* profile follows the median profile of cenHighMh nicely until 20 kpc; then it becomes much steeper in the outskirt. This is quite consistent with the expectation that the inner part of the BCGs should be well developed at $z \sim 1$, but the extended stellar envelope is still assembling.

Also, it is worth noting that the relative flatten inner μ_* profile of cenHighMh at fixed $M_{*,100\text{kpc}}$ could be an interesting feature, although we currently lack of the resolution to investigate region ≤ 3 kpc. It is known that major-merger induced coalesce of super-massive black holes (SMBHs) can create flattened inner profile (e.g. Milosavljević et al. 2002), and recent discoveries of massive BCGs with very large core (a few kpc; e.g. Postman et al. 2012; López-Cruz et al. 2014) further complicate the picture. On Fig.10, there are a few cenHighMh galaxies with quite low $M_{*,10\text{kpc}}$ at high $M_{*,100\text{kpc}}$ end. After examining their images, we conclude the low $M_{*,10\text{kpc}}$ is not caused by problematic photometry or exceptionally bad seeing; they could also be massive BCGs with very flattened inner μ_* profiles. Besides the SMBH-merger

theory, strong adiabatic expansion induced by strong AGN feedback was proposed to modify the inner mass distribution (e.g. Fan et al. 2008). The potential impact of these processes to massive galaxies, and their dependence on halo mass would be an interesting topic to investigate in the future.

[Song: Move a big paragraph to Results]

[Song: Ok, I'll see how to make it happen; this sounds abrupt since I used to have several subsections in the discussion section.] [Alexie: The beginning part of this paragraph sounds to me like the summary section. You could move part of this to summary and put it in bullet point format.]. In the end, we want to emphasize once more the importance of deep image and appropriate method of photometry in studying the structure and assembly history of galaxies. With the help of deep HSC images, we reliably reveal the extended stellar structures around large sample of massive central galaxies out to more than 100 kpc. And, using model-independent method, we found that (1) previous de Vaucouleur or single-Sérsic modeling method on shallower SDSS images underestimates the total mass of massive galaxies; (2) even using deep HSC images, photometric method like cModel also tends to underestimate the mass. For these massive central galaxies, their extended mass distributions are simply beyond the capability of the simply modeling method. In addition, since the slope and mass contribution of the outer envelope depend on not only the total stellar mass, but also likely the halo mass. Applying the same oversimplified model to galaxies across a large range of mass and environment could result in both underestimated and biased mass estimates that can stop us getting accurate stellar mass function at the high-mass end and studying potential environmental dependence of structures. Moreover, these results also raise crucial questions like: What is the definition of “total” stellar mass of galaxy? And, what is the most informative definition of stellar mass in the studies of galaxy evolution?. [Alexie: I think we can expand the discussion around this topic. We'd like to say something about the impact of total luminosity on the SMF. How about moving the left hand of Figure 3 here? What is the current volume of your data set compared to the volume of SDSS? I think we should emphasize the impact of stellar mass estimate on the SMF, especially the large impact it has for BCGs]. [Song: As mentioned earlier, I can expand the discussion easily with the help from another figure, comparing with SMF from other people's work??]

[Alexie: Yes, the only thing that I just realized and pointed out in the earlier SMF figure is that to compare the SMF, we need to include everything, not just centrals. There are two options: 1) just show the impact on the SMF for centrals (the figure you have already) or 2) include all the galaxies and compared with previous work. I think that 2) is a paper itself and is beyond the scope of the papers (it becomes "Mission Creep").]

[Alexie: I thought of another interesting aspect to add to the discussion. This I think is perhaps a nice angle to discuss. The total luminosity of a galaxy has an impact on abundance matching. Do you have the “luminosity” that you would get for each galaxy if you assumed a single Sérsic fit for example? If so, we could do the following. Assume a one-to-one mapping between halo mass and your M100. Then plot Mhalo versus the stellar mass inferred from either cmodel or the single Sérsic fit. Then we can quote the scatter in $\log(M_*)$ at fixed Mhalo that this introduces. This figure will be very relevant for the Santa

Barabara workshop!? [Song: We do not have results from single Sersic models; at least not reliable enough to be used here, mostly because single Sersic works terribly for these galaxies. We do have $M_{*,\text{cModel}}$, but sorry that I failed to follows the logic here, basically this is the difference between $M_{*,100\text{kpc}}$ and $M_{*,\text{cModel}}$ expressed in a different way, and I am not sure the scatter is due to the scatter of the mhalo-mstar relation, as the cModel ones are underestimated due to technical reasons; We can bin the cenHighMh galaxies into a narrow λ bin thoug, e.g. $30 < \lambda < 40$, and see the scatter of $M_{*,\text{cModel}}$, $M_{*,10\text{kpc}}$, and $M_{*,100\text{kpc}}$. We can certainly shows that the scatter is larger for mass using larger radius. I think this point is important for the discussion of the intrinsic scatter of the mhalo-mstar relation, and at very similar mhalo, the outer structure may trace other properties of the halo. Let me know what do you think.]

[Alexie: THe same idea holds if we use our M100 mass and cmodel. The points is just to evaluate how much extra scatter you introduce because of many people simple use naive luminosities when they do abundance matching. Your previous figures show that the luminosities of massive galaxies may be severaly underestiamted. How much impact does this have on abundance matching? How much extra scatter does it introduce?]

[Alexie: Finally, another quick discussion paragraph could be related to finding BCGs. It would be interesting to have a plot of the magnitude gap between Pcen1 and Pcen 2 (the most likely and the second most likely central) with cmodel versus your estimates. It would be nice to show that having a better luminosity estimate will enable you to identify the BCG better (is this true?).] [Song: This is interesting, and I don't know if it is true. It requires more works as I do not have the profiles for all PCEN2 galaxies, I only do it when they are more massive than the threshold. Can we save this for later, I mean, after we send around the draft. Although I do compare the structures of really massive satellites in these clusters with the cenLowMh galaxies, and the results show little difference, basically shows that the structure difference could be unique for central galaxies. I originally show a figure for this, and will send you along the e-mail.]

[Alexie: If it is too much, work, skip this idea! We dont want mission creep.]

In this work, we choose mass enclosed by different, but fixed physical apertures, and find promising scientific applications for massive galaxies. But, we recognize that they may not be the best choice. For instance, central galaxies of massive halos like BCGs are known to be surrounded by diffuse stellar component that does not follow the potential of the central galaxy (the intra-cluster light, or ICL; e.g. REF). In theory, it can contribute a large amount of stellar mass out to very large radius (e.g. REF). Using the definition of $M_{*,100\text{kpc}}$, we can not separate the potential contribution of ICL in our cenHighMh galaxies; and this could make complicate the discussion of environmental dependence. [Alexie: I am not sure I agree here. What is the "ICL"? How can is physically be defined? Can one robustly distinguish an "ICL" component from the galaxy component and how? Is the ICL similar to the "cD" enveloppe in the sense that we use these words all the time, but in practice, these are just one extrema of a continous galaxy population?] Since most of the cenHighMh galaxies in our sample belong to low-mass

cluster like the Virgo or Fornax, we do not expect the ICL component can makes a smooth and significant contribution to the μ_* profiles (e.g. REF). Even removing all cenHighMh galaxies in $\lambda > 40$ clusters will not change our findings. However, it is still important to ask whether should we include the ICL when estimating the mass of central galaxies in massive halos. [Alexie: But what is the ICL?] [Song: The observational definiton is very vague; and the theoretical one is very hard to achieve through observation, basically the stars that follows the potential of the cluter.] [Alexie: Exactly. Which is why I think we dont want to go into a big discussion on this.] And, if the answer is no, which is the best way to separate the ICL component? In literature, most works studied ICL by subtracting the model for inner part of the central galaxy (e.g. REF). As we show in this work, when extended stellar envelopes are revealed around massive galaxies in large range of stellar and halo mass, we may have to reconsider this approach [Alexie: I agree with this phrase, this is good to point out.]. [Song: I think I understand your point here. The thing with ICL is that any conclusion so far is quite uncertain, so I can reorganize this paragraph, point out the interesting question first, discuss it a little bit, but also shows a caveat that say ICL could play a role here, and if it does, how could they change our results.]

[Alexie: I'm saying more than that. I'm saying that I don't beleive that there is necessarily a firm distinction between the galaxy and the "ICL". Might be easier to chat about this on Skype.]

7. SUMMARY AND FUTURE PLANS

In this work, we study the how environment (halo mass) affects the structures and assembly history of massive central galaxies using deep images from the Subaru HSC survey. With the help of these high-quality data, we map the stellar mass distributions of large numbers of massive central galaxies at $0.3 < z < 0.5$ out to > 100 kpc, and discussing their environmental dependence after grouping them into centrals of halos more and less massive than $M_{\text{halo}} \sim 10^{14} M_\odot$. The main results here are:

1. We find that the “total” M_* of these massive galaxies could be significantly underestimated when shallow image (e.g. the SDSS ones) and/or imperfect model assumption (e.g. the cModel) are used. In different with previous works, this result does not depend on stacking analysis or any parametric model. Moreover, the level of such underestimation could also depend on the stellar mass. This should be carefully taken into account when discussing important topics like the stellar mass function and its evolution.
2. At fixed M_* within 100 kpc, we find that the massive central galaxies in more and less massive halos have subtle, but systematic differences in their μ_* profiles when their ellipticity and optical color profiles are very similar. On average, the ones from denser environments have slightly shallower inner μ_* profiles while showing more prominent outer envelope.
3. Meanwhile, when matched at the same M_* within inner 10 kpc—a proxy of the M_* formed in the the “in-situ” channel, we find that the ones in more massive halos possess much more extended stellar envelope in the outskirts than the ones in smaller halos when the μ_* ,

- ellipticity, and optical color profiles inside 10 kpc show no dependence on environment.
- The M_* -size relation also reflects the subtle environmental dependence as the central galaxies from more massive halos have slightly higher R_{50} at fixed $M_{*,100\text{kpc}}$. We further suggest that the relation between $M_{*,100\text{kpc}}$ and $M_{*,10\text{kpc}}$ ¹¹ can be useful tool in diagnosing the assembly history of these massive galaxies and its relation to their dark matter halos.

These results are broadly consistent with the prediction of the “two-phase” scenario: the massive central galaxies in more massive halos should experience more minor, dry mergers that accumulate more stars in the outskirts. These results also highlight the advantages of HSC survey in studying the evolution of massive galaxies. Upon finishing this work, the HSC survey has already doubled its sky coverage to ~ 200 deg², and provides a much larger sample of massive central galaxies. At the same time, we will work on better data reduction of HSC images by improving the deblending in crowded regions and the accuracy of background subtraction. This can help provide more reliable SED fitting results, and push the photometric limit to even lower surface brightness.

Right now, we still rely on the redMaPPer catalog from SDSS and spectroscopic redshift from SDSS and BOSS. Running redMaPPer algorithm or similar group/cluster finder on HSC catalogs can greatly help us extend the discussion to lower M_{halo} and higher redshift. Better selection of satellites in massive halos will also open up the possibility to study “environment” within the halo. It is interesting to see whether there is any structural difference between central and satellite galaxy at similar M_* .

We will work on careful 2-D photometric modeling to these massive galaxies. Under the same principle outlined by Huang et al. 2013b, we will explore different models, and gradually build up the complexity to fit these galaxies better. With the 2-D modeling approach, we can deal with the seeing and background subtraction easier, and provide better maps the stellar mass distributions. We are also working on characterizing the color distributions of these galaxies better via multi-band modeling with reasonable constraints (e.g. Huang et al. 2016).

Primarily designed as a cosmological endeavor, the HSC survey has excellent images to greatly improve the the weak lensing analysis of massive galaxies. The next major step will be to investigate the connections between massive galaxies and their halos with the help of the weak lensing signals for different groups of massive galaxies (e.g. binned by $M_{*,100\text{kpc}}$, $M_{*,10\text{kpc}}$, size et al.). Joining the stellar mass distributions and the weak lensing signals together, we can trace the impacts from a series of physical processes (strength and type of AGN feedback, merger rate, typical mass ratio of mergers et al.). To help us have better physical insights, we will directly compare our results with predictions from cosmological hydro-simulations such as Illustris (Vogelsberger et al. 2014, Genel et al. 2014), EAGLE (Schaye et al. 2015, Crain et al. 2015), or Horizon-AGN (Dubois et al. 2014).

The Hyper Suprime-Cam (HSC) collaboration includes the astronomical communities of Japan and Taiwan, and

¹¹ or any better proxy of total M_* and the mass formed in the “in-situ” phase.

Princeton University. The HSC instrumentation and software were developed by the National Astronomical Observatory of Japan (NAOJ), the Kavli Institute for the Physics and Mathematics of the Universe (Kavli IPMU), the University of Tokyo, the High Energy Accelerator Research Organization (KEK), the Academia Sinica Institute for Astronomy and Astrophysics in Taiwan (ASIAA), and Princeton University. Funding was contributed by the FIRST program from Japanese Cabinet Office, the Ministry of Education, Culture, Sports, Science and Technology (MEXT), the Japan Society for the Promotion of Science (JSPS), Japan Science and Technology Agency (JST), the Toray Science Foundation, NAOJ, Kavli IPMU, KEK, ASIAA, and Princeton University.

Funding for SDSS-III has been provided by the Alfred P. Sloan Foundation, the Participating Institutions, the National Science Foundation, and the U.S. Department of Energy. The SDSS-III web site is <http://www.sdss3.org>. SDSS-III is managed by the Astrophysical Research Consortium for the Participating Institutions of the SDSS-III Collaboration including the University of Arizona, the Brazilian Participation Group, Brookhaven National Laboratory, University of Cambridge, University of Florida, the French Participation Group, the German Participation Group, the Instituto de Astrofísica de Canarias, the Michigan State/Notre Dame/JINA Participation Group, Johns Hopkins University, Lawrence Berkeley National Laboratory, Max Planck Institute for Astrophysics, New Mexico State University, New York University, Ohio State University, Pennsylvania State University, University of Portsmouth, Princeton University, the Spanish Participation Group, University of Tokyo, University of Utah, Vanderbilt University, University of Virginia, University of Washington, and Yale University.

The Pan-STARRS1 Surveys (PS1) have been made possible through contributions of the Institute for Astronomy, the University of Hawaii, the Pan-STARRS Project Office, the Max-Planck Society and its participating institutes, the Max Planck Institute for Astronomy, Heidelberg and the Max Planck Institute for Extraterrestrial Physics, Garching, The Johns Hopkins University, Durham University, the University of Edinburgh, Queen’s University Belfast, the Harvard-Smithsonian Center for Astrophysics, the Las Cumbres Observatory Global Telescope Network Incorporated, the National Central University of Taiwan, the Space Telescope Science Institute, the National Aeronautics and Space Administration under Grant No. NNX08AR22G issued through the Planetary Science Division of the NASA Science Mission Directorate, the National Science Foundation under Grant No. AST-1238877, the University of Maryland, and Eotvos Lorand University (ELTE).

This paper makes use of software developed for the Large Synoptic Survey Telescope. We thank the LSST Project for making their code available as free software at <http://dm.lsstcorp.org>.

This research made use of: `STSCI PYTHON`, a general astronomical data analysis infrastructure in Python. `STSCI PYTHON` is a product of the Space Telescope Science Institute, which is operated by AURA for NASA; `SciPy`, an open source scientific tools for Python (Jones et al. 2001); `NumPy`, a fundamental package for scientific computing with Python (Walt et al. 2011); `Matplotlib`, a 2-D plotting library for Python (Hunter 2007); `Astropy`, a community-developed core Python package for Astronomy (`Astropy Collaboration` et al. 2013); `scikit-learn`, a machine-learning library in Python (Pedregosa et al. 2011); `astroml`, a machine learning library for astrophysics (Van-

derplas et al. 2012); IPython, an interactive computing system for Python (Pérez & Granger 2007); sep Source Extraction and Photometry in Python (Barbary et al. 2015);

palettable, color palettes for Python; emcee, Seriously Kick-Ass MCMC in Python; Colossus, COsmology, haLO and large-Scale StrUcture toolS (Diemer 2015).

REFERENCES

- Aihara, H., Allende Prieto, C., An, D., et al. 2011, ApJS, 193, 29
 Alam, S., Albareti, F. D., Allende Prieto, C., et al. 2015, ApJS, 219, 12
 Annis, J., Soares-Santos, M., Strauss, M. A., et al. 2014, ApJ, 794, 120
 Astropy Collaboration, Robitaille, T. P., Tollerud, E. J., et al. 2013, A&A, 558, A33
 Axelrod, T., Kantor, J., Lupton, R. H., & Pierfederici, F. 2010, in Proc. SPIE, Vol. 7740, Software and Cyberinfrastructure for Astronomy, 774015
 Bai, L., Yee, H. K. C., Yan, R., et al. 2014, ApJ, 789, 134
 Barbary, Boone, & Deil. 2015, sep: v0.3.0
 Behroozi, P. S., Wechsler, R. H., & Conroy, C. 2013, ApJ, 770, 57
 Bellstedt, S., Lidman, C., Muzzin, A., et al. 2016, MNRAS, 460, 2862
 Bernardi, M., Meert, A., Sheth, R. K., et al. 2016a, ArXiv e-prints
 —. 2016b, MNRAS, 455, 4122
 —. 2013, MNRAS, 436, 697
 Blanton, M. R., Kazin, E., Muna, D., Weaver, B. A., & Price-Whelan, A. 2011, AJ, 142, 31
 Bosch, J. in prep., In preparation
 Bruzual, G., & Charlot, S. 2003, MNRAS, 344, 1000
 Bundy, K., Leauthaud, A., Saito, S., et al. 2015, ApJS, 221, 15
 Calzetti, D., Armus, L., Bohlin, R. C., et al. 2000, ApJ, 533, 682
 Cappellari, M., McDermid, R. M., Alatalo, K., et al. 2012, Nature, 484, 485
 —. 2013, MNRAS, 432, 1862
 Cebrán, M., & Trujillo, I. 2014, MNRAS, 444, 682
 Chabrier, G. 2003, PASP, 115, 763
 Conroy, C., & Gunn, J. E. 2010a, FSPS: Flexible Stellar Population Synthesis, Astrophysics Source Code Library
 —. 2010b, ApJ, 712, 833
 Conroy, C., & van Dokkum, P. G. 2012, ApJ, 760, 71
 Cooper, A. P., D’Souza, R., Kauffmann, G., et al. 2013, MNRAS, 434, 3348
 Cooper, A. P., Cole, S., Frenk, C. S., et al. 2010, MNRAS, 406, 744
 Cooper, M. C., Griffith, R. L., Newman, J. A., et al. 2012, MNRAS, 419, 3018
 Crain, R. A., Schaye, J., Bower, R. G., et al. 2015, MNRAS, 450, 1937
 Diemer, B. 2015, Colossus: COsmology, haLO, and large-Scale StrUcture tools, Astrophysics Source Code Library
 Diemer, B., & Kravtsov, A. V. 2015, ApJ, 799, 108
 Driver, S. P., Hill, D. T., Kelvin, L. S., et al. 2011, MNRAS, 413, 971
 D’Souza, R., Kauffmann, G., Wang, J., & Vegetti, S. 2014, MNRAS, 443, 1433
 D’Souza, R., Vegetti, S., & Kauffmann, G. 2015, MNRAS, 454, 4027
 Dubois, Y., Pichon, C., Welker, C., et al. 2014, MNRAS, 444, 1453
 Eisenstein, D. J., Weinberg, D. H., Agol, E., et al. 2011, AJ, 142, 72
 Falcón-Barroso, J., Sánchez-Blázquez, P., Vazdekis, A., et al. 2011, A&A, 532, A95
 Fan, L., Lapi, A., De Zotti, G., & Danese, L. 2008, ApJ, 689, L101
 Farahi, A., Evrard, A. E., Rozo, E., Rykoff, E. S., & Wechsler, R. H. 2016, MNRAS, 460, 3900
 Foreman-Mackey, D., Hogg, D. W., Lang, D., & Goodman, J. 2013, PASP, 125, 306
 Genel, S., Vogelsberger, M., Springel, V., et al. 2014, MNRAS, 445, 175
 Hilz, M., Naab, T., & Ostriker, J. P. 2013, MNRAS, 429, 2924
 Ho, L. C., Li, Z.-Y., Barth, A. J., Seigar, M. S., & Peng, C. Y. 2011, ApJS, 197, 21
 Hopkins, P. F., Hernquist, L., Cox, T. J., Dutta, S. N., & Rothberg, B. 2008, ApJ, 679, 156
 Huang, S., Ho, L. C., Peng, C. Y., Li, Z.-Y., & Barth, A. J. 2013a, ApJ, 768, L28
 —. 2013b, ApJ, 766, 47
 —. 2016, ApJ, 821, 114
 Huertas-Company, M., Shankar, F., Mei, S., et al. 2013, ApJ, 779, 29
 Hunter, J. D. 2007, Computing In Science & Engineering, 9, 90
 Inagaki, T., Lin, Y.-T., Huang, H.-J., Hsieh, B.-C., & Sugiyama, N. 2015, MNRAS, 446, 1107
 Jones, E., Oliphant, T., Peterson, P., et al. 2001, SciPy: Open source scientific tools for Python, [Online; accessed 2016-09-30]
 Jurić, M., Kantor, J., Lim, K., et al. 2015, ArXiv e-prints
 Kauffmann, G., Heckman, T. M., White, S. D. M., et al. 2003, MNRAS, 341, 54
 Kelkar, K., Aragón-Salamanca, A., Gray, M. E., et al. 2015, MNRAS, 450, 1246
 Kelvin, L. S., Driver, S. P., Robotham, A. S. G., et al. 2012, MNRAS, 421, 1007
 Kormendy, J., Fisher, D. B., Cornell, M. E., & Bender, R. 2009, ApJS, 182, 216
 Kravtsov, A., Vikhlinin, A., & Meshcheryakov, A. 2014, ArXiv e-prints
 La Barbera, F., De Carvalho, R. R., De La Rosa, I. G., et al. 2010, AJ, 140, 1528
 La Barbera, F., Ferreras, I., de Carvalho, R. R., et al. 2012, MNRAS, 426, 2300
 Lauer, T. R., Gebhardt, K., Faber, S. M., et al. 2007, ApJ, 664, 226
 Lawrence, A., Warren, S. J., Almaini, O., et al. 2007, MNRAS, 379, 1599
 Leauthaud, A., Tinker, J., Bundy, K., et al. 2012, ApJ, 744, 159
 Leauthaud, A., Bundy, K., Saito, S., et al. 2016, MNRAS, 457, 4021
 Leja, J., van Dokkum, P., & Franx, M. 2013, ApJ, 766, 33
 Li, Z.-Y., Ho, L. C., Barth, A. J., & Peng, C. Y. 2011, ApJS, 197, 22
 Liske, J., Baldry, I. K., Driver, S. P., et al. 2015, MNRAS, 452, 2087
 Liu, F. S., Guo, Y., Koo, D. C., et al. 2013, ApJ, 769, 147
 López-Cruz, O., Afonso, C., Birkkinshaw, M., et al. 2014, ApJ, 795, L31
 Lupton, R., Blanton, M. R., Fekete, G., et al. 2004, PASP, 116, 133
 Magnier, E. A., Schlafly, E., Finkbeiner, D., et al. 2013, ApJS, 205, 20
 Meert, A., Vikram, V., & Bernardi, M. 2015, MNRAS, 446, 3943
 Milosavljević, M., Merritt, D., Rest, A., & van den Bosch, F. C. 2002, MNRAS, 331, L51
 Miyazaki, S., Komiyama, Y., Nakaya, H., et al. 2012, in Proc. SPIE, Vol. 8446, Ground-based and Airborne Instrumentation for Astronomy IV, 84460Z
 Moustakas, J., Coil, A. L., Aird, J., et al. 2013, ApJ, 767, 50
 Nair, P. B., van den Bergh, S., & Abraham, R. G. 2010, ApJ, 715, 606
 Oke, J. B., & Gunn, J. E. 1983, ApJ, 266, 713
 Oogi, T., & Habe, A. 2013, MNRAS, 428, 641
 Papovich, C., Bassett, R., Lotz, J. M., et al. 2012, ApJ, 750, 93
 Park, C., Choi, Y.-Y., Vogeley, M. S., et al. 2007, ApJ, 658, 898
 Patel, S. G., van Dokkum, P. G., Franx, M., et al. 2013, ApJ, 766, 15
 Pedregosa, F., Varoquaux, G., Gramfort, A., et al. 2011, Journal of Machine Learning Research, 12, 2825
 Pérez, F., & Granger, B. E. 2007, Computing in Science and Engineering, 9, 21
 Pillepich, A., Vogelsberger, M., Deason, A., et al. 2014, MNRAS, 444, 237
 Postman, M., Lauer, T. R., Donahue, M., et al. 2012, ApJ, 756, 159
 Ricciardelli, E., Vazdekis, A., Cenarro, A. J., & Falcón-Barroso, J. 2012, MNRAS, 424, 172
 Rodriguez-Gomez, V., Pillepich, A., Sales, L. V., et al. 2016, MNRAS, 458, 2371
 Rozo, E., & Rykoff, E. S. 2014, ApJ, 783, 80
 Rozo, E., Rykoff, E. S., Bartlett, J. G., & Melin, J.-B. 2015a, MNRAS, 450, 592
 Rozo, E., Rykoff, E. S., Becker, M., Reddick, R. M., & Wechsler, R. H. 2015b, MNRAS, 453, 38
 Rykoff, E. S., Rozo, E., Busha, M. T., et al. 2014, ApJ, 785, 104
 Salpeter, E. E. 1955, ApJ, 121, 161
 Sánchez-Blázquez, P., Peletier, R. F., Jiménez-Vicente, J., et al. 2006, MNRAS, 371, 703
 Saro, A., Bocquet, S., Rozo, E., et al. 2015, MNRAS, 454, 2305
 Savorgnan, G., Graham, A. W., Marconi, A., et al. 2013, MNRAS, 434, 387
 Schaye, J., Crain, R. A., Bower, R. G., et al. 2015, MNRAS, 446, 521
 Schlafly, E. F., & Finkbeiner, D. P. 2011, ApJ, 737, 103
 Schlafly, E. F., Finkbeiner, D. P., Jurić, M., et al. 2012, ApJ, 756, 158
 Shankar, F., Marulli, F., Bernardi, M., et al. 2013, MNRAS, 428, 109
 Simet, M., McClintock, T., Mandelbaum, R., et al. 2016, ArXiv e-prints
 Tal, T., & van Dokkum, P. G. 2011, ApJ, 731, 89
 Taylor, E. N., Hopkins, A. M., Baldry, I. K., et al. 2011, MNRAS, 418, 1587
 Tonry, J. L., Stubbs, C. W., Lykke, K. R., et al. 2012, ApJ, 750, 99
 van der Wel, A., Franx, M., van Dokkum, P. G., et al. 2014, ApJ, 788, 28
 van Dokkum, P. G., Whitaker, K. E., Brammer, G., et al. 2010, ApJ, 709, 1018
 van Uitert, E., Cacciato, M., Hoekstra, H., et al. 2016, MNRAS, 459, 3251
 Vanderplas, J., Connolly, A., Ivezić, Ž., & Gray, A. 2012, in Conference on Intelligent Data Understanding (CIDU), 47–54
 Vogelsberger, M., Genel, S., Springel, V., et al. 2014, MNRAS, 444, 1518
 Walcher, J., Groves, B., Budavári, T., & Dale, D. 2011, Ap&SS, 331, 1

- Walt, S. v. d., Colbert, S. C., & Varoquaux, G. 2011, Computing in Science and Engg., 13, 22
- Weinmann, S. M., Kauffmann, G., van den Bosch, F. C., et al. 2009, MNRAS, 394, 1213
- Wellons, S., Torrey, P., Ma, C.-P., et al. 2016, MNRAS, 456, 1030
- Wu, H., Shao, Z., Mo, H. J., Xia, X., & Deng, Z. 2005, ApJ, 622, 244
- Yang, X., Mo, H. J., van den Bosch, F. C., et al. 2007, ApJ, 671, 153
- Zhao, D., Aragón-Salamanca, A., & Conselice, C. J. 2015, MNRAS, 448, 2530

APPENDIX

A. BASIC STATISTICAL PROPERTIES OF THE SAMPLE

In the top-left figure of Fig.13, we show the $M_{*,100\text{kpc}}$ -color relations using the k -corrected $g - r$ color for the cenHighMh and cenLowMh samples. Both samples follow the same tight “red-sequence” with very little contamination from star-forming galaxy in the “blue cloud”. And, at fixed $M_{*,100\text{kpc}}$, we see little offset in color distributions of the two samples suggesting that both samples consist of old quiescent galaxies with similar average stellar population properties. This is consistent with previous result that suggests the average stellar population of massive central galaxy does not depend on M_{halo} (e.g. Park et al. 2007). To look into the potential environmental dependence of structure, we will focus on the mass range of $11.6 \leq \log(M_{*,100\text{kpc}}/M_{\odot}) \leq 11.9$, where both samples have acceptable completeness, and their $M_{*,100\text{kpc}}$ distributions greatly overlap (see the normalized distributions of $M_{*,100\text{kpc}}$ in the bottom-left panel of Fig.13). The similar situation applies to the $M_{*,10\text{kpc}}$ distributions as well, where the two samples overlap the most within $11.2 \leq \log(M_{*,100\text{kpc}}/M_{\odot}) \leq 11.6$, but have quite different relative distributions.

Due to the different sources of redshift for the cenHighMh and cenLowMh samples, the two samples have somewhat different redshift distributions (right figure of Fig.13), even within the $11.6 \leq \log(M_{*,100\text{kpc}}/M_{\odot}) \leq 11.9$ mass bin. Apparently, the redshift distribution of the cenLowMh sample skews toward higher- z end, primarily due to the contribution of BOSS spec- z . This could bias the comparison of μ_* profiles and other properties (please see Appendix E for more details). We will address this via matching the two samples in both mass and redshift distributions carefully before any comparison (see Appendix F).

B. EXTRACTION OF 1-D SURFACE BRIGHTNESS PROFILE

C. ESTIMATE AVERAGE M_*/L_* USING ISEDFIT

We adopt flat distribution between 0.5 to 14.0 Gyrs as prior for the look-back time when the star formation turned on. The exponential delayed time-scale (τ) is allowed to change between 0.1 to 3.0 with equal probability. The chance of random star burst is set at 0.2 for every 2 Gyrs. The duration of the star burst is draw from a logarithmic distribution between 0.03 to 0.3 Gyr; and the mass fraction formed in the burst is from a logarithmic distribution between 0.01 and 1.0.

In principle, these choices of priors could leave systematic effects in the estimate of stellar mass (e.g. Bernardi et al. 2016a). For low- z massive ETGs like the ones in our sample, the details form of SFH, importance of random star burst, and the dust extinction should not be major concern. However, the choices of stellar population models and IMF can still change the results systematically. More discussions on this can be found in Appendix A. In short:

1. Both FSPS+MILES and BC03 (Bruzual & Charlot 2003) models still have difficulties recovering the optical color involving filters at the red end (e.g $i - Y$), which could relate to the challenge for modern stellar population models to reproduce the optical color-color relation of red-sequence galaxies (e.g. Ricciardelli et al. 2012), or the shallower photometry of HSC-Y band data.
2. The BC03 provides slightly better overall χ^2 and systematically smaller M_* than the FSPS+MILES models. However, it is possible that the BC03 model tends to underestimate the M_*/L_* for a fraction of them as the estimate stellar age is unrealistically young for red, massive galaxies. Therefore, we still use the FSPS+MILES model as the fiducial one. But, switching to the BC03 model will not change any key result in this work.
3. The usage of Salpeter (1955) IMF results in systematically higher M_* (on average +0.25 dex of $\log(M_*/M_{\odot})$). Although there are multiple lines of evidence that favor Salpeter or even more “bottom-heavy” IMF in the most massive ETGs (e.g. Conroy & van Dokkum 2012; Cappellari et al. 2012), we still present the main results using Chabrier IMF to accommodate galaxies with lower M_* in the sample, and to be as consistent as possible with a few other works. Also, the choice of IMF does not impact our results qualitatively.

Besides the priors for stellar population properties, different treatments of the light profile and accuracy of sky background subtraction are also important for the estimate of M_* as they strongly impact the estimate of total luminosity (e.g. Bernardi et al. 2013 and D’Souza et al. 2015). At the depth of SDSS, the default cModel photometry is already shown to be not very accurate at high- M_* end (e.g. Meert et al. 2015; Bernardi et al. 2016b) as it does not capture the extended envelope of these galaxies. As for HSC, it is much more challenging for cModel to recover the total luminosity of massive ETGs since the stellar envelope becomes even more extended for neither de Vaucouleur or exponential model to reproduce. However, the HSC cModel under the force-photometry mode can measure **average** color of the galaxy with great accuracy (e.g. Huang et al. in prep.), and provide us a reliable SED to estimate the **average** M_*/L_* . Considering this, we separate the process of estimating the total M_* of massive ETGs in our sample into two steps:

1. Firstly, using the redshift and cModel magnitude in five bands, we derive an initial estimate of the M_* of the galaxy. More importantly, we derive the **average** M_*/L_* in i -band of the galaxy, and use the best-fit SED to provide k -correction to the photometry.

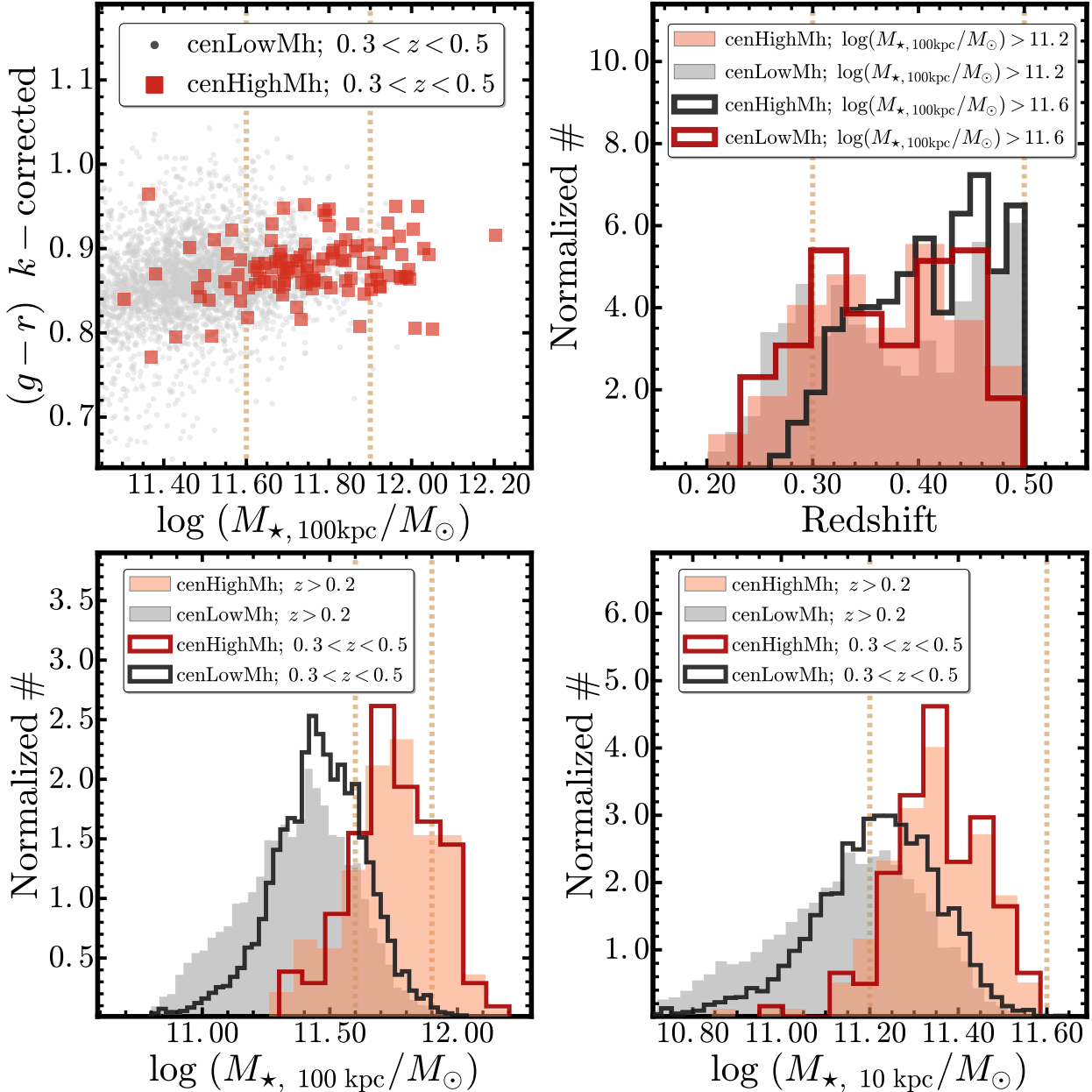


FIG. 13.— **Top-left:** The $\log(M_*/M_\odot)$ - $g-r$ color relation of the `cenHighMh` (red circle; datafield format is the same with the right panel of Fig.4) and `cenLowMh` (grey dots) samples. We apply the k -corrections from `iSEDFit` fitting to the colors. **Top-right:** the histograms of the redshift for the `cenHighMh` and `cenLowMh` galaxies in both $\log(M_*, 100\text{ kpc}/M_\odot) > 11.2$ and $11.6 < \log(M_*, 100\text{ kpc}/M_\odot) < 11.9$ mass bins. The vertical lines highlights the $0.3 \leq z \leq 0.5$ redshift range. **Bottom-left:** the histograms of $M_*, 100\text{ kpc}$ for the `cenHighMh` (orange-red) and `cenLowMh` (grey-black) samples at both $z > 0.2$ (step-filled histogram) and $0.3 \leq z \leq 0.5$ (stepped histogram). The vertical lines in both top-left and bottom-left figures highlight the $11.6 < \log(M_*, 100\text{ kpc}/M_\odot) < 11.9$ mass range that will be used in the comparison of the $M_*, 100\text{ kpc}$ -matched samples. **Bottom-right:** the histograms of $M_*, 10\text{ kpc}$ in similar format. Here the vertical lines highlight the $11.2 < \log(M_*, 10\text{ kpc}/M_\odot) < 11.6$ mass range that is used for comparison.

2. In the next section, we will derive better estimate of total M_* using the more accurate total luminosity in i -band from integration of carefully measured 1-D surface brightness profile, and the average M_*/L_* from the SED fitting.

The basic results from `iSEDFit` are summarized in Figure 2, where we compare the relations between initial estimates of M_* and (both luminosity and star formation weighted) stellar age, metallicity, and dust extinction. As expected, most galaxies in our samples are $\log(M_{*, \text{ini}}/M_\odot) \geq 11.2$ massive galaxies that have old age, high metallicity ($1.5 \times Z_\odot$ is the highest metallicity allowed), and low dust extinction. Given that we only have photometry from five optical bands, degeneracies among age, metallicity, and dust extinction are naturally expected. We will not use them for any scientific reason in this work, but to show that they behave reasonably.

D. COMPARISON OF μ_* PROFILES USING M_* FROM THE GAMA SURVEY

As the sky coverage of this release greatly overlaps with the GAMA survey, we start the detailed comparison with an external check using the stellar mass estimated by (Taylor et al. 2011). The purpose is still to investigate the impact of deeper photometry

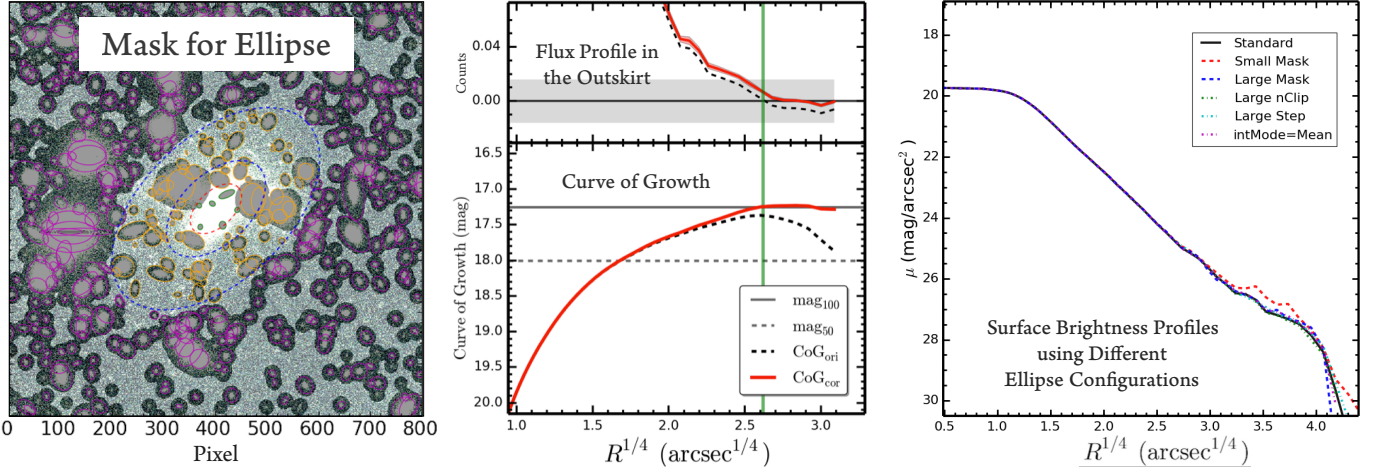


FIG. 14.— **Left:** Example of the object-mask built for the `Ellipse` run for a typical massive galaxy in the sample. All the shaded regions are masked out. The three dash lines (red, inner one and two blue ones) around the target at the center outlines the three radius we defined using the flux radius of the target. We increase the mask size for objects detected in different regions separated by these apertures (which are outlined by solid, elliptical apertures with different colors) using slightly different criteria. **Middle:** The flux profile that is zoomed into the near-zero flux range (top panel), and the curve-of-growth of the magnitude for the example massive galaxy. To highlight the importance of correcting sky background, we show the profiles using both images with (red, solid line) and without (black, dash line) ad-hoc background correction. On the top panel, besides the horizontal line that highlights the zero flux level, we also show the uncertainty of the sky background estimate via grey-shaded region. On the bottom panel, two horizontal lines indicate the magnitudes corresponding to total (solid) and half flux (dash) using the background-corrected profile. **Right:** compare the 1-D surface brightness profiles for the same example galaxy extracted using different mask (smaller masking region: red, dash line; larger masks: blue, dash line), or different `Ellipse` settings (more aggressive pixel-clipping: cyan, dash line; larger step in radius: green, dash line; using mean flux along the isophote instead of median: purple, dash line) with the one using the default configuration (black, solid line).

[Song: Figure will be updated]

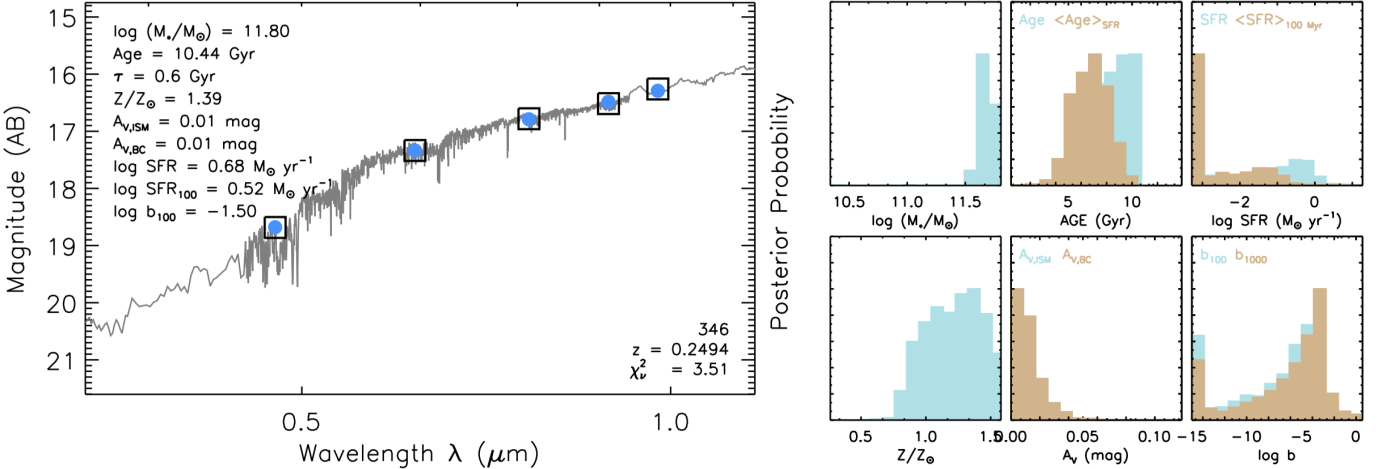


FIG. 15.— Left: example output figure from `iSEDFit` that shows the SED fitting results. The open-boxes show the observed fluxes in 5-band, and the solid, blue-dots show the best-fitted results, along with the high-resolution spectrum for this model reconstructed using the synthetic spectra from `FSPS`. Top-left corner shows the best-fit stellar population parameters, and bottom-right corner shows the ID, redshift of this object, and reduced χ^2 of the best-fit model. Right: the Posterior distributions of a few key parameters. From top-left to bottom right are: 1) stellar mass ($\log(M_*/M_\odot)$); 2) age of the population (mass and star-formation rate weighted) in Gyr; 3) star formation rate ($\log SFR (M_\odot/\text{yr})$; instant one and the one averaged over the previous 100 Myr); 4) stellar metallicity (Z/Z_\odot); 5) dust extinction (A_V in mag); 6) birthrate parameter ($\log b$; averaged over previous 100 and 1000 Myr).

on the analysis of structure of massive galaxies. The stellar masses of GAMA galaxies are initially derived through careful optical-SED fitting (BC03 model; Chabrier IMF) using the PSF-matched aperture photometry. Then they were corrected for the total luminosity estimated using single-Sérsic 2-D model to multi-band images (Kelvin et al. 2012). We separate the `cenHighMh` and `cenLowMh` galaxies that also have `spec-z` and stellar mass in GAMA DR2 (Liske et al. 2015). Most of galaxies in these subsamples have $z < 0.40$.

In Fig. 10, we show the results of matches for subsamples using $M_{*,\text{GAMA}}$. To increase the number of available `cenHighMh` to match, we loosen its selection criteria to $\lambda \geq 20$ and $P_{\text{CEN}} \geq 0.6$. Based on the distributions of the two samples at the $M_{*,\text{GAMA}}-z$ plane, and their overlapped region, we match them in two bins of $M_{*,\text{GAMA}}$ that have slightly different redshift ranges. For the samples in two $M_{*,\text{GAMA}}$, the matches appear to be very good.

In Fig. 18, we show the individual profiles, median profiles along with their uncertainties derived using 5000 times bootstrap resampling, and the relative difference between the profile of the `cenHighMh` and `cenLowMh` subsamples. It is very clear that, for both mass bins, the `cenHighMh` has a much more extended outer envelope, while its profile inside ~ 10 kpc is very close to

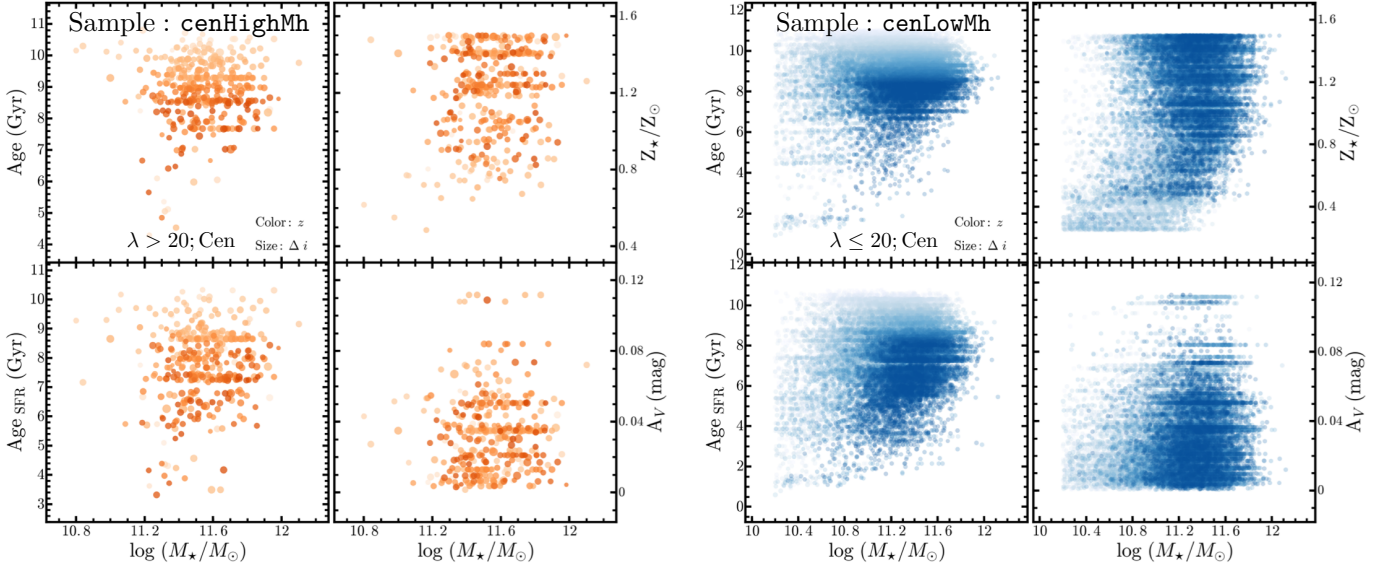


FIG. 16.— Relationships between M_* and certain stellar population parameter using `iSEDfit`. The left figures are for the `cenHighMh` sample, while the right ones are for the `cenLowMh` sample. They are both color-coded using the mass-weighted stellar age. The four stellar population properties shown here are: 1) mass-weighted stellar age in Gyr (top-left); 2) SFR-weighted stellar age in Gyr (bottom-left); 3) mass-weighted stellar metallicity in unit of solar value (top-right); 4) dust extinction value in magnitude (bottom-right).

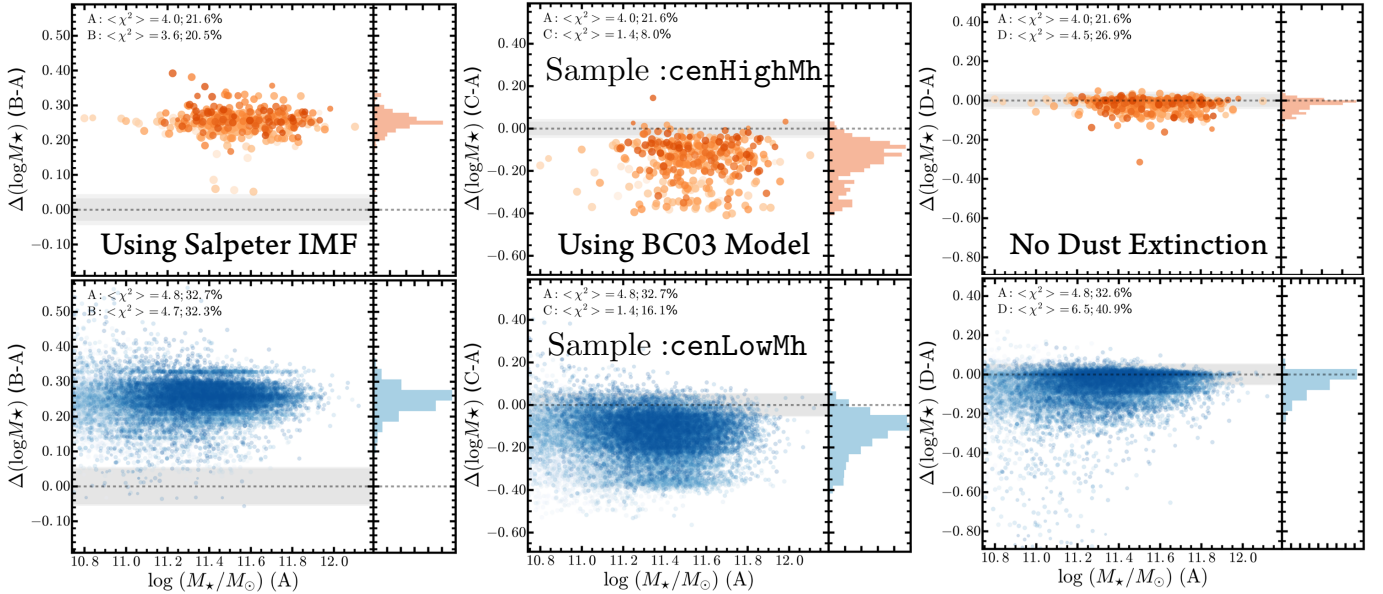


FIG. 17.— Comparisons of M_* estimated by `iSEDfit` using different assumptions. In each figure, we plot the default M_* values against their differences with the results using other models. The top (bottom) row shows comparisons for the `cenHighMh` (`cenLowMh`) sample. The results involved here are labeled: (A): default one; (B): using the Salpeter IMF instead of the Chabrier one (Left column); (C): using the BC03 synthetic population model instead of the FSPS one (Middle column); (D): assume that there is no dust extinction (Right column). On each figure, a horizontal line shows the zero difference level, along with the grey shaded region that highlights the typical uncertainty of the M_* -differences. We also show the histogram of the M_* -differences on the right.

the `cenLowMh` one. This is inconsistent with the matched distributions of their “total” stellar mass, and reveals potential issue with the stellar mass estimated by GAMA. We can reproduce very similar results using the luminosity density profiles (with or without k -correction) of these matched samples, which suggests that the main problem does not lie in the estimate of M_*/L_* , but in the measurement of total luminosity using single-Sérsic model. This highlights the importance of deep optical images in studying the structure of massive galaxies.

In cases of these $M_{*,\text{GAMA}}$ -matched samples, the differences of median profiles are very robust.

E. COMPARISONS OF μ_* PROFILES IN DIFFERENT REDSHIFT BINS

As the massive galaxies in our samples span quite a bit in both redshift and $M_{*,100\text{kpc}}$, it is important to evaluate the impact from PSF on the μ_* profiles at different redshift. In Fig.19, we group the `cenHighMh` and `cenLowMh` galaxies at

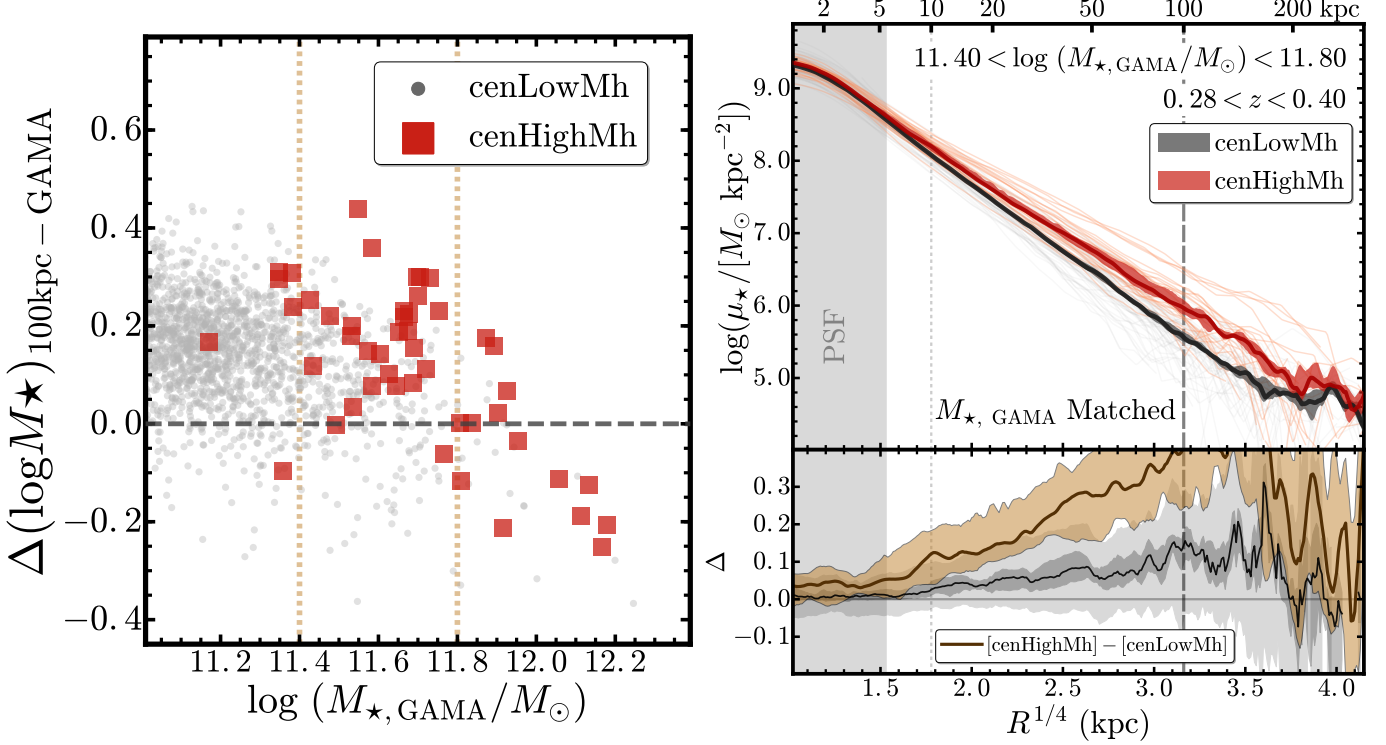


FIG. 18.— **Left:** comparison of M_{\star} estimated by the GAMA survey and the $M_{\star,100\text{kpc}}$ using HSC images in this work. We plot the $\log(M_{\star,\text{GAMA}}/M_{\odot})$ against the difference between $\log(M_{\star,100\text{kpc}}/M_{\odot})$ and $\log(M_{\star,\text{GAMA}}/M_{\odot})$. The format is very similar to the left panel of Fig.4. The two vertical lines highlight the mass range $11.4 \leq \log(M_{\star,\text{GAMA}}/M_{\odot}) < 11.8$ that is used for the comparison. **Right:** we compare the μ_{\star} profiles of cenHighMh (orange-red) and cenLowMh (grey-black) galaxies using the samples matched on the $M_{\star,\text{GAMA}}-z$ plane at $11.4 \leq \log(M_{\star,\text{GAMA}}/M_{\odot}) < 11.9$ and $0.28 \leq z < 0.4$. The format is very similar to the ones in Fig.6.

$11.6 \leq \log(M_{\star,100\text{kpc}}/M_{\odot}) < 11.9$ into two z bins ($0.3 \leq z < 0.4$ and $0.4 \leq z < 0.5$). We did not match the $M_{\star,100\text{kpc}}$ distributions in two z bins, so slight difference in average $M_{\star,100\text{kpc}}$ can be expected. With the same seeing condition, the μ_{\star} profile of galaxy at higher redshift is more vulnerable to the PSF smearing effect in the center, while suffers more in the outskirt due to cosmological dimming and background noise. Fig.19 clearly shows that, although the median profiles of the same sample in two redshift bins follow each other well outside 10 kpc, they start to differ in the central 2-3 kpc as the one from higher redshift bin has more flattened profile due to PSF smearing effect. Meanwhile, we notice that the median profiles of cenHighMh and cenLowMh in the same z bin are very similar to each other in the region affected by seeing. This comparison confirms the radius range that is sensitive to seeing and redshift distribution is well constrained within the grey-shaded area. It also suggests that it is important to match the redshift distributions between samples before we can compare their μ_{\star} profiles or other properties at inner region, as we did in this work. In the outskirt, within 100-150 kpc, we see no difference in the median μ_{\star} profiles caused by redshift distributions. We therefore conclude that it is safe to study the μ_{\star} profile within this radius range for massive galaxies at $z < 0.5$ using HSC images.

F. MATCH THE CENHIGHMH AND CENLOWMH SAMPLES IN M_{\star} AND REDSHIFT DISTRIBUTIONS

[Song: Still need some adjustments]

As stellar mass is considered the most important parameter in determining the structure and other properties of massive galaxies, it is crucial to make sure the comparison is conducted at “fixed stellar mass”. And, since we directly compare the stellar mass distributions across very large range in radius, it is also important to make sure that differences in physical size of PSF (for more discussion on this issue, please see Appendix.D) and imaging depth do not affect the result. In practice, we achieve these by matching the cenHighMh and cenLowMh samples in the distributions of M_{\star} and redshift in the mass range where both samples have decent completeness. Since the cenHighMh sample is much smaller in size, we match the cenLowMh sample to it by searching for the N nearest neighbours on the M_{\star} -redshift plane using the KDTree algorithm provided by scikit-learn Python library (Pedregosa et al. 2011). The quality of the matched sample is evaluated by not just the median values of stellar mass and redshift, but also the kernel density distributions (KDE) of these two properties. For M_{\star} , we use a Gaussian kernel with width equals to the typical uncertainty of the mass estimate (0.06-0.10); and for redshift, we choose 0.025 as the width of the Gaussian kernel. As we only keep unique cenLowMh galaxies in the matched sample, we manually adjust the value of N to achieve the most similar distribution. In case that the distribution of stellar mass or redshift for cenHighMh is bi-modal, we also try to split the sample into two, and match them separately. Normally N is between 3 to 8.

M_{\star} within different radius traces different physical processes and different epochs in the assembly history. In this section, we match the two samples using our proxy of “total” stellar mass, which is the M_{\star} within 100 kpc radius. This choice reflects the stellar mass distributions we can safely measure using model-independent approach given the current depth of the image and the

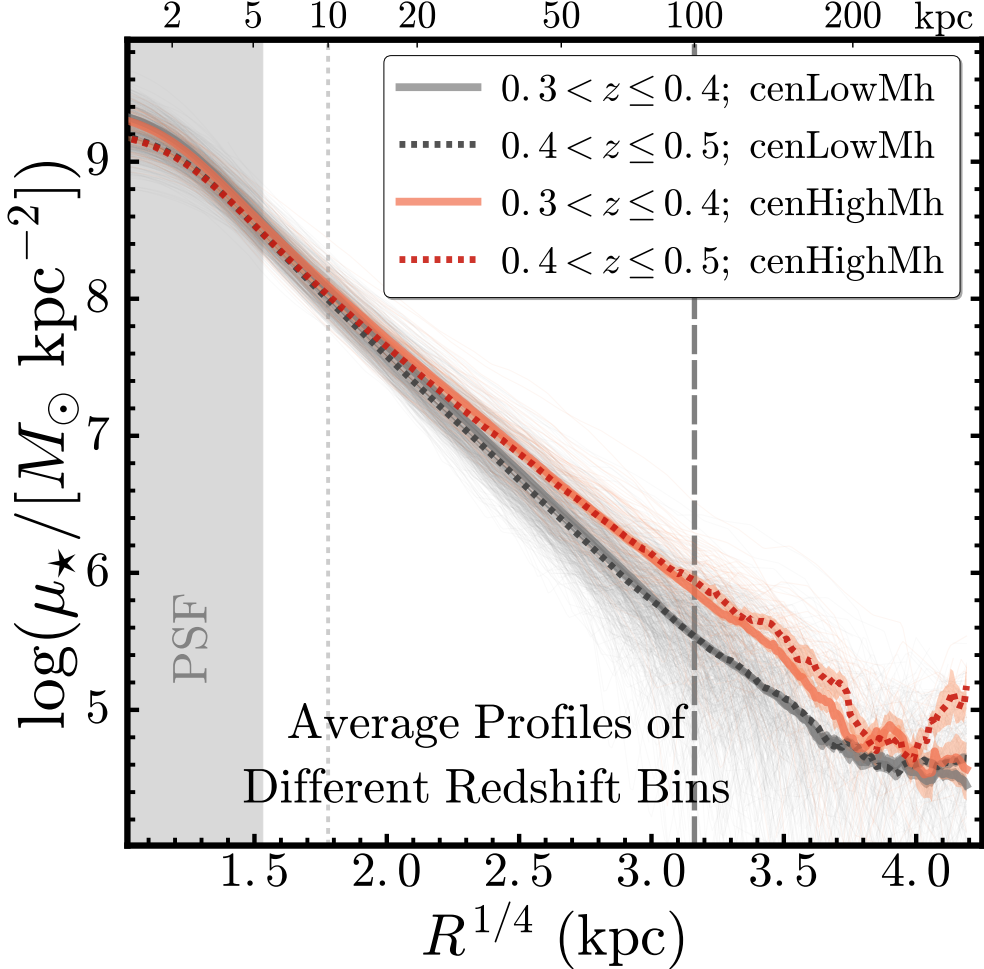


FIG. 19.— Comparison of μ_* profiles of cenHighMh (orange-red) and cenLowMh (grey-black) at $11.6 \leq \log(M_{*,100\text{kpc}}/M_\odot) < 11.9$ in redshift bins of $0.3 \leq z < 0.4$ (solid lines) and $0.4 \leq z < 0.5$ (dash lines). We show the individual profile in the background using much thinner line, and highlight the median profiles using thicker line and darker color. Other formats are exactly the same with the left figure of Fig. 5.

accuracy of sky background subtraction. For galaxies at $11.6 \leq \log(M_*/M_\odot) < 11.9$, 100 kpc equals to 5-8 times of their effective radius, hence should enclose most their stellar mass. Also, for a fraction of massive cenHighMh galaxies, the intra-group/cluster light (IGL/ICL) could dominate their mass profiles outside 100 kpc (REF), and complicate the comparison with the cenLowMh galaxies. We will discuss these issues later in Section 6, but in conclusion, the proxy of total M_* and the potential ICL component should not affect the results.

G. ROBUSTNESS OF THE μ_* DIFFERENCES

[Song: Need some text!]

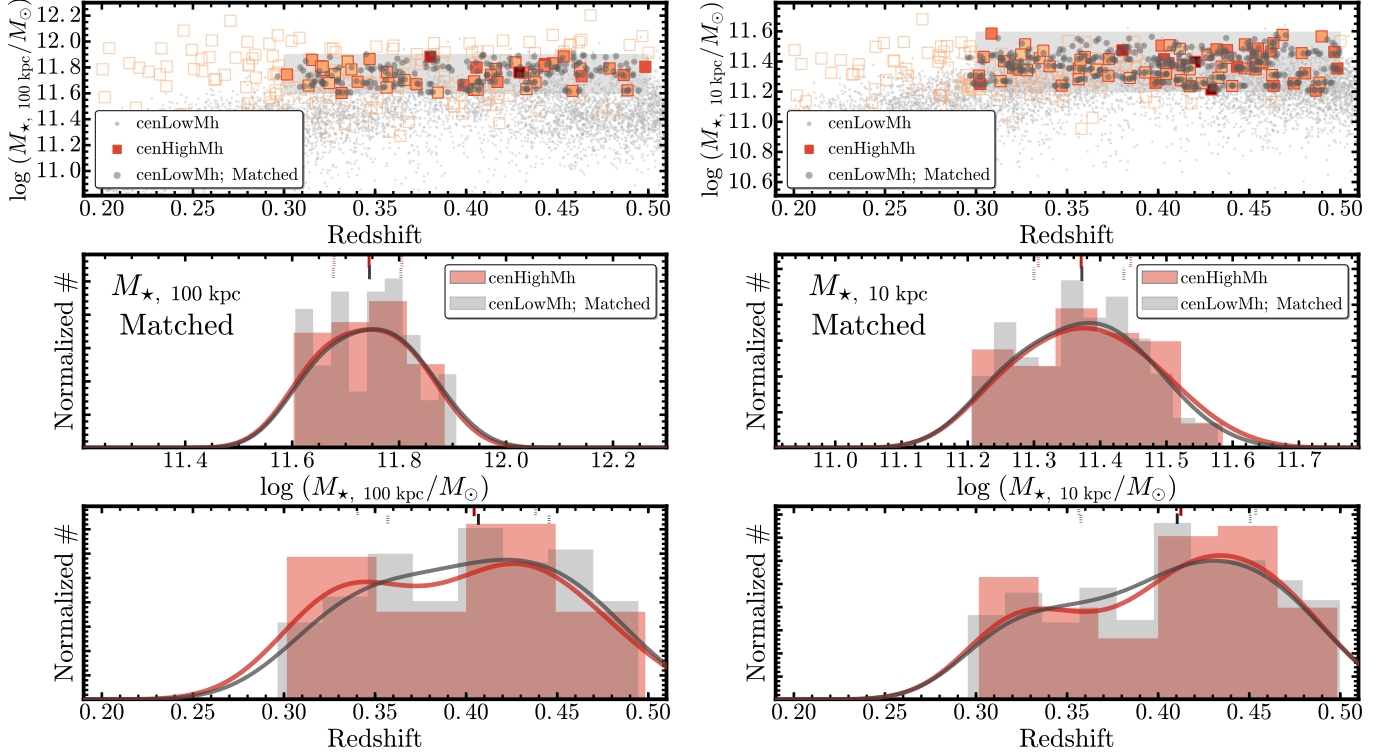


FIG. 20.— **Left figure** shows the details of the $M_{\star,100\text{kpc}}$ -matching process, corresponding to the results shown in the left figure of On the top panel, we show the overall distributions of cenHighMh (light orange boxes) and cenLowMh (light grey dots) galaxies on the $M_{\star,100\text{kpc}}-z$ plane. And, we match the two sample in the $M_{\star,100\text{kpc}}-z$ space outlined by the shaded region. We highlight the cenHighMh galaxies in this region using bigger boxes in red frames, whose size reflects the P_{Cen} value. We also color-code them using the richness (λ) of the host cluster. The matched cenLowMh galaxies are highlighted using darker color and bigger dots. To further evaluate the matching results, we show the distributions of $M_{\star,100\text{kpc}}$ (middle panel) and redshift (bottom panel) separately. On both panesl, we show the histograms along with their kernel density distributions. And, on the top of each panel, two sets of short vertical lines highlight the median value (solid) and the inter-quartile (dash) of each distribution. **Right figure** shows the similar matching results for the $M_{\star,10\text{kpc}}$ -matched samples used for the right figure of Fig.6. The format is exactly the same as the left one, except the $M_{\star,10\text{kpc}}$ replaces the $M_{\star,100\text{kpc}}$ in the top and middle panels.

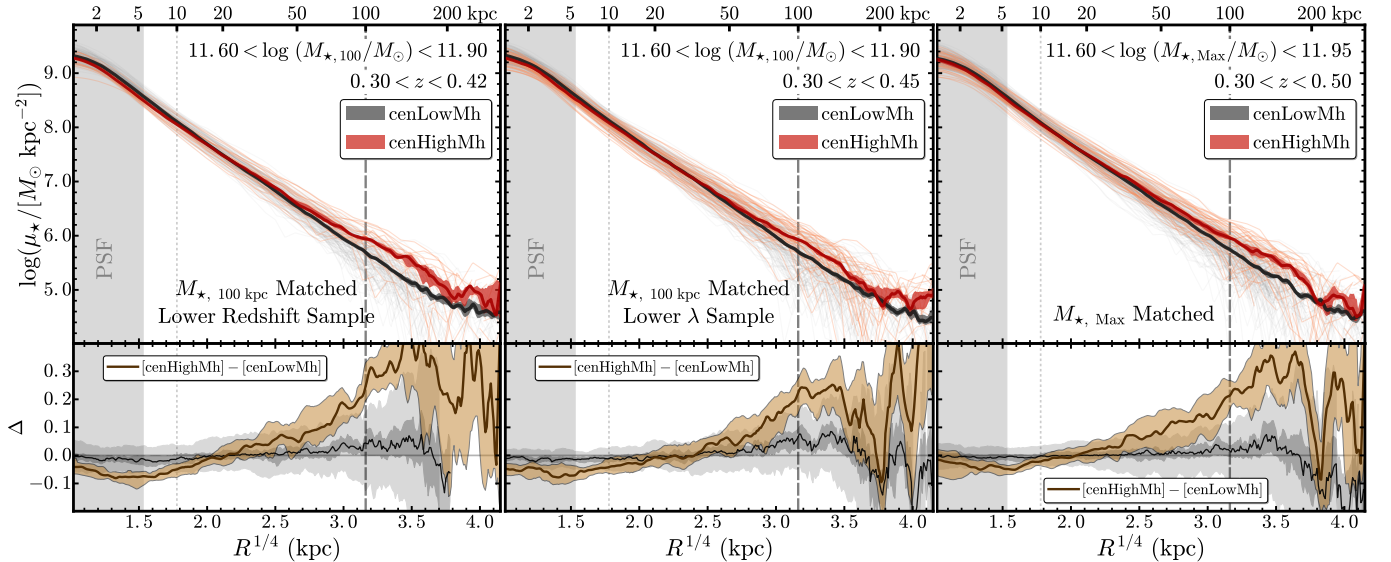


FIG. 21.— Comparisons of the μ_{\star} profiles for cenHighMh (orange-red) and cenLowMh (grey-black) galaxies that are matched using proxies of total M_{\star} . The formats are in consistent with the right figure of Fig.6. The differences are, here, the samples are matched in slightly differnt ways. From left to right: a) using samples at lower redshift ($0.3 < z < 0.4$); b) using cenHighMh sample with $\lambda > 20$ instead of 30; c) using M_{\star} within 150 kpc instead of 100 kpc. The results are broadly consistent with the one in Fig.6.

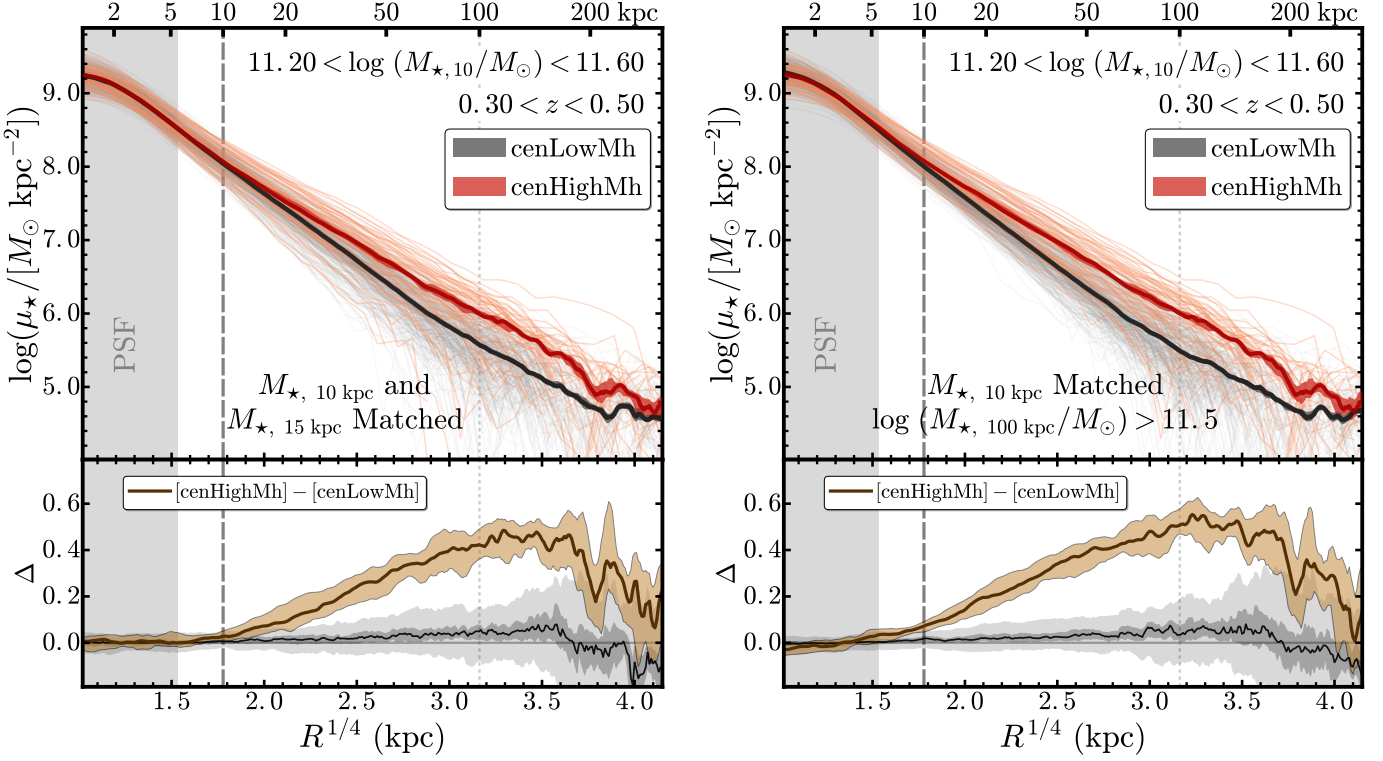


FIG. 22.— Comparisons of the μ_* profiles for cenHighMh (orange-red) and cenLowMh (grey-black) galaxies that are matched using the M_* enclosed in the inner region. Left panel shows the results after matching the $M_{*,10\text{kpc}}$ and $M_{*,15\text{kpc}}$ together, and the right panel shows the results when only the $\log(M_{*,100\text{kpc}}/M_\odot) \geq 11.5$ cenHighMh and cenLowMh galaxies are included. Other formats are in consistent with the right figure of Fig.6.

TABLE 1
AVERAGE μ_* PROFILES OF MASSIVE GALAXIES IN DIFFERENT STELLAR MASS BINS

Radius kpc	[μ_*]; Combined samples			[μ_*]; $M_{*,100\text{ kpc}}$ -matched		[μ_*]; $M_{*,10\text{ kpc}}$ -matched	
	$\log(M_\odot/\text{kpc}^2)$			$\log(M_\odot/\text{kpc}^2)$		$\log(M_\odot/\text{kpc}^2)$	
	$\log \frac{M_{*,100\text{kpc}}}{M_\odot} \in [11.4, 11.6]$	$[11.6, 11.8]$	$[11.8, 12.0]$	cenHighMh	cenLowMh	cenHighMh	cenLowMh
(1)	(2)	(3)	(4)	(5)	(6)	(7)	(8)
0.0	9.23 \pm 0.00	9.31 \pm 0.00	9.32 \pm 0.01	9.31 \pm 0.02	9.34 \pm 0.01	9.31 \pm 0.02	9.34 \pm 0.02
0.6	9.20 \pm 0.00	9.28 \pm 0.00	9.29 \pm 0.01	9.27 \pm 0.02	9.31 \pm 0.01	9.28 \pm 0.02	9.31 \pm 0.02
1.0	9.16 \pm 0.00	9.24 \pm 0.00	9.26 \pm 0.01	9.24 \pm 0.02	9.27 \pm 0.01	9.25 \pm 0.02	9.27 \pm 0.02
1.4	9.12 \pm 0.00	9.20 \pm 0.00	9.23 \pm 0.01	9.20 \pm 0.02	9.23 \pm 0.01	9.21 \pm 0.02	9.23 \pm 0.01
1.7	9.06 \pm 0.00	9.15 \pm 0.00	9.19 \pm 0.01	9.15 \pm 0.02	9.19 \pm 0.01	9.16 \pm 0.01	9.18 \pm 0.01
2.0	9.00 \pm 0.00	9.10 \pm 0.00	9.15 \pm 0.01	9.09 \pm 0.01	9.13 \pm 0.01	9.11 \pm 0.01	9.12 \pm 0.01
2.4	8.93 \pm 0.00	9.03 \pm 0.00	9.09 \pm 0.01	9.03 \pm 0.02	9.07 \pm 0.01	9.05 \pm 0.01	9.05 \pm 0.01
2.7	8.87 \pm 0.00	8.97 \pm 0.00	9.04 \pm 0.01	8.97 \pm 0.01	9.01 \pm 0.01	9.00 \pm 0.01	8.99 \pm 0.01
3.0	8.80 \pm 0.00	8.90 \pm 0.00	8.98 \pm 0.01	8.90 \pm 0.01	8.95 \pm 0.01	8.93 \pm 0.01	8.92 \pm 0.01
3.4	8.72 \pm 0.00	8.83 \pm 0.00	8.92 \pm 0.01	8.83 \pm 0.01	8.88 \pm 0.01	8.86 \pm 0.01	8.85 \pm 0.01
3.7	8.66 \pm 0.00	8.78 \pm 0.00	8.87 \pm 0.01	8.78 \pm 0.01	8.83 \pm 0.01	8.81 \pm 0.01	8.79 \pm 0.01
4.1	8.60 \pm 0.00	8.72 \pm 0.00	8.82 \pm 0.01	8.72 \pm 0.01	8.77 \pm 0.01	8.76 \pm 0.01	8.73 \pm 0.01
4.4	8.54 \pm 0.00	8.66 \pm 0.00	8.77 \pm 0.01	8.66 \pm 0.01	8.72 \pm 0.01	8.70 \pm 0.01	8.67 \pm 0.01
4.8	8.48 \pm 0.00	8.60 \pm 0.00	8.71 \pm 0.01	8.60 \pm 0.01	8.66 \pm 0.01	8.65 \pm 0.01	8.61 \pm 0.01
6.2	8.26 \pm 0.00	8.40 \pm 0.00	8.53 \pm 0.01	8.41 \pm 0.01	8.46 \pm 0.01	8.46 \pm 0.02	8.40 \pm 0.02
7.6	8.09 \pm 0.00	8.24 \pm 0.00	8.39 \pm 0.01	8.27 \pm 0.01	8.31 \pm 0.01	8.31 \pm 0.02	8.23 \pm 0.02
9.0	7.95 \pm 0.00	8.10 \pm 0.00	8.27 \pm 0.01	8.14 \pm 0.02	8.18 \pm 0.01	8.19 \pm 0.02	8.09 \pm 0.02
10.3	7.82 \pm 0.00	7.99 \pm 0.00	8.16 \pm 0.01	8.03 \pm 0.02	8.06 \pm 0.01	8.09 \pm 0.02	7.97 \pm 0.02
11.7	7.70 \pm 0.00	7.88 \pm 0.00	8.06 \pm 0.01	7.93 \pm 0.02	7.96 \pm 0.01	7.99 \pm 0.02	7.85 \pm 0.02
13.0	7.60 \pm 0.00	7.78 \pm 0.00	7.98 \pm 0.01	7.85 \pm 0.02	7.87 \pm 0.01	7.90 \pm 0.02	7.75 \pm 0.02
14.5	7.50 \pm 0.00	7.69 \pm 0.00	7.90 \pm 0.01	7.76 \pm 0.02	7.78 \pm 0.01	7.82 \pm 0.02	7.65 \pm 0.02
16.0	7.39 \pm 0.00	7.60 \pm 0.00	7.82 \pm 0.01	7.68 \pm 0.02	7.69 \pm 0.01	7.74 \pm 0.02	7.56 \pm 0.03
17.3	7.31 \pm 0.00	7.52 \pm 0.00	7.76 \pm 0.01	7.61 \pm 0.02	7.62 \pm 0.01	7.67 \pm 0.03	7.48 \pm 0.03
18.7	7.23 \pm 0.00	7.45 \pm 0.00	7.69 \pm 0.01	7.55 \pm 0.02	7.55 \pm 0.01	7.61 \pm 0.03	7.40 \pm 0.03
22.6	7.02 \pm 0.00	7.27 \pm 0.00	7.54 \pm 0.01	7.38 \pm 0.02	7.37 \pm 0.01	7.45 \pm 0.03	7.21 \pm 0.03
26.1	6.86 \pm 0.00	7.12 \pm 0.00	7.41 \pm 0.01	7.25 \pm 0.02	7.24 \pm 0.01	7.32 \pm 0.03	7.05 \pm 0.03
30.0	6.70 \pm 0.00	6.98 \pm 0.00	7.29 \pm 0.01	7.13 \pm 0.03	7.10 \pm 0.01	7.20 \pm 0.03	6.90 \pm 0.03
33.7	6.55 \pm 0.00	6.85 \pm 0.00	7.18 \pm 0.01	7.01 \pm 0.03	6.98 \pm 0.01	7.09 \pm 0.03	6.76 \pm 0.03
37.8	6.41 \pm 0.00	6.72 \pm 0.01	7.07 \pm 0.01	6.90 \pm 0.03	6.85 \pm 0.01	6.98 \pm 0.04	6.63 \pm 0.04
41.6	6.29 \pm 0.01	6.61 \pm 0.01	6.98 \pm 0.01	6.81 \pm 0.03	6.75 \pm 0.01	6.89 \pm 0.04	6.51 \pm 0.04
45.7	6.17 \pm 0.01	6.50 \pm 0.01	6.88 \pm 0.01	6.71 \pm 0.03	6.64 \pm 0.01	6.79 \pm 0.04	6.39 \pm 0.04
49.3	6.07 \pm 0.01	6.41 \pm 0.01	6.80 \pm 0.01	6.62 \pm 0.03	6.56 \pm 0.01	6.70 \pm 0.04	6.30 \pm 0.04
53.1	5.98 \pm 0.01	6.33 \pm 0.01	6.71 \pm 0.02	6.55 \pm 0.03	6.46 \pm 0.01	6.64 \pm 0.04	6.21 \pm 0.04
57.2	5.88 \pm 0.01	6.24 \pm 0.01	6.63 \pm 0.02	6.47 \pm 0.04	6.37 \pm 0.01	6.56 \pm 0.04	6.11 \pm 0.04
61.5	5.79 \pm 0.01	6.15 \pm 0.01	6.55 \pm 0.02	6.39 \pm 0.04	6.29 \pm 0.01	6.49 \pm 0.04	6.03 \pm 0.04
66.0	5.70 \pm 0.01	6.05 \pm 0.01	6.47 \pm 0.02	6.32 \pm 0.04	6.20 \pm 0.01	6.37 \pm 0.05	5.94 \pm 0.05
69.8	5.64 \pm 0.01	5.98 \pm 0.01	6.40 \pm 0.02	6.25 \pm 0.04	6.12 \pm 0.02	6.35 \pm 0.04	5.87 \pm 0.04
74.7	5.56 \pm 0.01	5.89 \pm 0.01	6.32 \pm 0.02	6.18 \pm 0.04	6.04 \pm 0.02	6.28 \pm 0.05	5.79 \pm 0.05
79.9	5.49 \pm 0.01	5.81 \pm 0.01	6.24 \pm 0.02	6.12 \pm 0.04	5.96 \pm 0.02	6.20 \pm 0.05	5.72 \pm 0.06
84.3	5.43 \pm 0.01	5.74 \pm 0.01	6.18 \pm 0.02	6.05 \pm 0.04	5.89 \pm 0.02	6.16 \pm 0.05	5.65 \pm 0.05
88.8	5.38 \pm 0.01	5.67 \pm 0.01	6.11 \pm 0.02	5.99 \pm 0.05	5.81 \pm 0.02	6.08 \pm 0.05	5.58 \pm 0.06
97.2	5.29 \pm 0.01	5.56 \pm 0.01	5.98 \pm 0.02	5.92 \pm 0.04	5.69 \pm 0.02	5.99 \pm 0.05	5.47 \pm 0.05
103.6	5.21 \pm 0.01	5.49 \pm 0.01	5.89 \pm 0.03	5.84 \pm 0.05	5.62 \pm 0.02	5.94 \pm 0.05	5.39 \pm 0.05
111.6	5.14 \pm 0.01	5.40 \pm 0.01	5.79 \pm 0.03	5.78 \pm 0.05	5.54 \pm 0.02	5.87 \pm 0.05	5.32 \pm 0.05
117.2	5.10 \pm 0.01	5.36 \pm 0.01	5.72 \pm 0.03	5.72 \pm 0.05	5.47 \pm 0.02	5.82 \pm 0.05	5.29 \pm 0.05
129.0	5.00 \pm 0.01	5.25 \pm 0.02	5.61 \pm 0.03	5.64 \pm 0.05	5.36 \pm 0.02	5.74 \pm 0.05	5.21 \pm 0.05
141.7	4.89 \pm 0.02	5.13 \pm 0.02	5.49 \pm 0.03	5.58 \pm 0.05	5.23 \pm 0.03	5.66 \pm 0.05	5.09 \pm 0.05
146.7	4.85 \pm 0.02	5.10 \pm 0.02	5.46 \pm 0.03	5.51 \pm 0.06	5.19 \pm 0.03	5.61 \pm 0.05	5.03 \pm 0.05

NOTE. — Average μ_* profiles of massive cenHighMh and cenLowMh galaxies in different samples:

Col. (1) Radius along the major axis in kpc.

Col. (2) Average μ_* profile for galaxies with $11.4 \leq \log(M_{*,100\text{kpc}}/M_\odot) < 11.6$ in the combined samples of cenHighMh and cenLowMh galaxies.

Col. (3) Average μ_* profile of combined samples in the mass bin of $11.6 \leq \log(M_{*,100\text{kpc}}/M_\odot) < 11.8$.

Col. (4) Average μ_* profile of combined samples in the mass bin of $11.8 \leq \log(M_{*,100\text{kpc}}/M_\odot) < 12.0$.

Col. (5) and Col. (6) are the average μ_* profiles of cenHighMh and cenLowMh galaxies in the $M_{*,100\text{kpc}}$ -matched samples within $11.6 \leq \log(M_{*,100\text{kpc}}/M_\odot) < 11.9$.

Col. (7) and Col. (8) are the average μ_* profiles of cenHighMh and cenLowMh galaxies in the $M_{*,10\text{kpc}}$ -matched samples within $11.2 \leq \log(M_{*,100\text{kpc}}/M_\odot) < 11.6$. The upper and lower uncertainties of these average profiles via bootstrap-resampling method are also displayed.